DEVELOPMENT OF NONDESTRUCTIVE EVALUATION METHODS FOR STRUCTURAL CERAMICS

W. A. Ellingson, R. D. Koehl, H. P. Engel,*
J. B. Stuckey, J. G. Sun, and R. G. Smith+
Argonne National Laboratory
*Heaviside Science, Inc.
+3M Corporation

ABSTRACT

Development of nondestructive evaluation (NDE) methods for application to fossil energy systems continues in three areas: (a) mapping axial and radial density gradients in hot-gas filters, (b) characterization of the quality of continuous-fiber ceramic matrix composite (CFCC) joints and (c) characterization and detection of defects in thermal-barrier coatings. In our work, X-ray computed tomographic imaging was further developed and used to map variations in the axial and radial density of two full-length (2.3-m) hot-gas filters. The two filters differed in through-wall density because of the thickness of the coating on the continuous fibers. Differences in axial and through-wall density were clearly detected.

Through-transmission infrared imaging with a highly sensitivity focal-plane array camera was used to assess joint quality in two sets of SiC/SiC CFCC joints. High-frame-rate data-capture suggests that our infrared imaging method holds potential for the characterization of CFCC joints.

Work to develop NDE methods that can be used to evaluate electron-beam physical-vapor-deposited coatings with platinum-aluminide (Pt-Al) bonds was undertaken. Coatings of Zirconia with thicknesses of 125 μm (0.005 in.), 190 μm (0.0075 in.), and 254 μm (0.010 in.) with a Pt-Al bond coat on René N5 Ni-based superalloy were studied by infrared imaging. Currently, it appears that thickness variation, as well as thermal properties, can be assessed by infrared technology.

INTRODUCTION

Nondestructive evaluation (NDE) technology is being developed to advance the reliable application of ceramic materials to fossil energy systems for improved efficiency and better environmental control. Advanced materials systems under development for fossil energy applications include continuous-fiber ceramic matrix composites (CFCCs) for hot-gas filters and heat exchangers, and thermal-barrier coatings (TBCs) for high gas-firing-temperature turbines.

Detection and measurement of variations in the axial and radial density of hot-gas filters are important, because change in density can be used as a process control parameter during fabrication and because density measurements can be used to study the efficiency of back-purging during cleaning.

Ceramic-to-ceramic joining is usually necessary both for shop fabrication of parts with complex shapes and for field repair. Many processes are under development to join CFCC materials. Researchers at the Idaho National Engineeering Laboratory (INEL)joined one set of specimens with a lapjoint. A second set, also joined with a lap joint, was produced by Dow-Corning.

While focusing on monolithic SiC and CFCC's with SiC/SiC, Rabin[1] and Rabin and Moore[2] of INEL clamp tape cast sheets of SiC + C precursor between parts that are to be bonded, and then infiltrate molten Si to form a reaction-bonded silicon carbide (RBSC) joint interlayer. Regardless of the method used for joining, NDE methods must be developed to establish the completeness and quality of the joint.

Thermal-barrier coatings are key material elements that allow higher gas-firing temperatures in gas turbines with low emissions. The integrity and properties (thermal and physical) of these TBC's depends on a reliable bond coat and careful process control.

For fossil energy applications, e.g., coal-gas-fired turbines, where the turbine duty cycle is much different from a typical aircraft engine, long-term, high-temperature exposure and high-cycle fatigue can be an issue, and the likelihood of spallation is increased. Answers to questions such as; What is the status of the coating? If damaged, should the blade be repaired? replaced? become matters of concern.

Work on the NDE of TBCs is initially concentrating on two methods: a) noncontact, noninvasive time-resolved-infrared-radiometry (TRIR)[3,4] for thermal characterization and b) elastic optical scatter[5] for crack detection and disbonds. In the TRIR method a thermal excitation source and a highly sensitive, high-frame rate (up to 1900 frames/sec) infrared camera are placed on one side of the TBC. The thermal excitation source can be a high- energy flash lamp or a laser. Thermal images are acquired in time sequence and analyzed.

METHODS AND RESULTS

Hot-Gas Filters

The use of high-spatial-resolution X-ray computed tomographic (XCT) methods for the study of hot-gas filters and heat exchangers has been explored previously.[3,6-8] In the work described here, two 2.3-meter-long, 3.8-mm-O.D. Nextel 611 fiber/SiC matrix hot-gas filters, supplied by 3M Corporation, were examined by XCT imaging densitometry. One of the filters was heavly coated, whereas the other was lightly coated. Figure 1, a schematic diagram of a typical filter, shows the location of the coating.

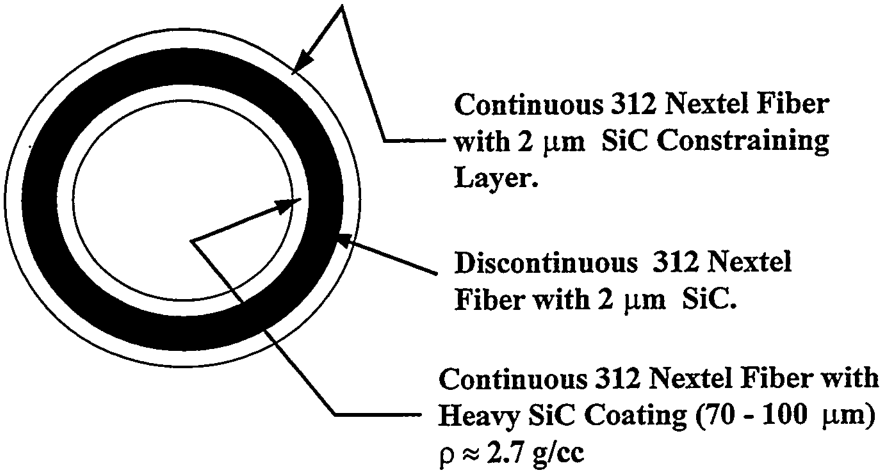

Fig. 1. Schematic diagram of cross section of 3M hot-gas filter

The XCT images were acquired every 50 mm along the length of the filters, as shown in Fig. 2, which is a projection X-ray digital radiograph (XDR). (Note that a holder is shown at the bottom of the XDR. This holder incorporates the flanges for mounting the hot-gas filters.)

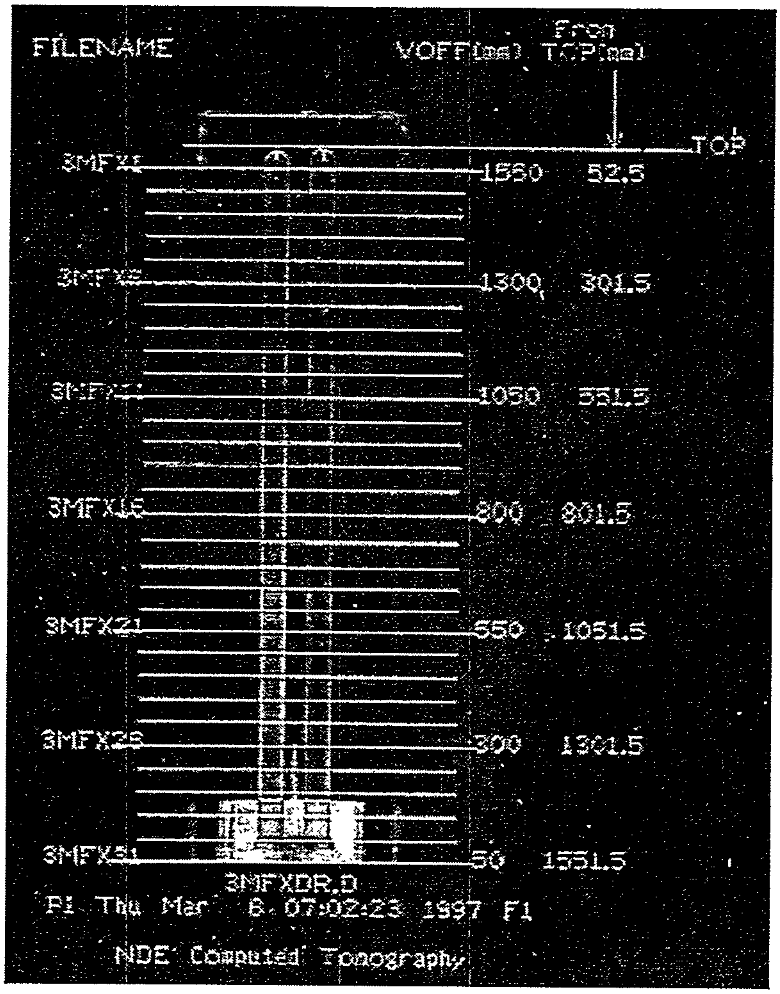

Fig. 2. X-Ray projection digital radiograph showing axial locations of X-ray tomographic images used for densitometry

The acquired XCT data clearly delineate differences between heavy and light coatings, as indicated in Fig. 3, which shows typical XCT images of the two hot-gas filters. By using digital image processing and determining the average density of each XCT image, one can plot relative density as a function of axial position. The variations in relative axial density that were obtained in this manner are shown in Fig. 4.

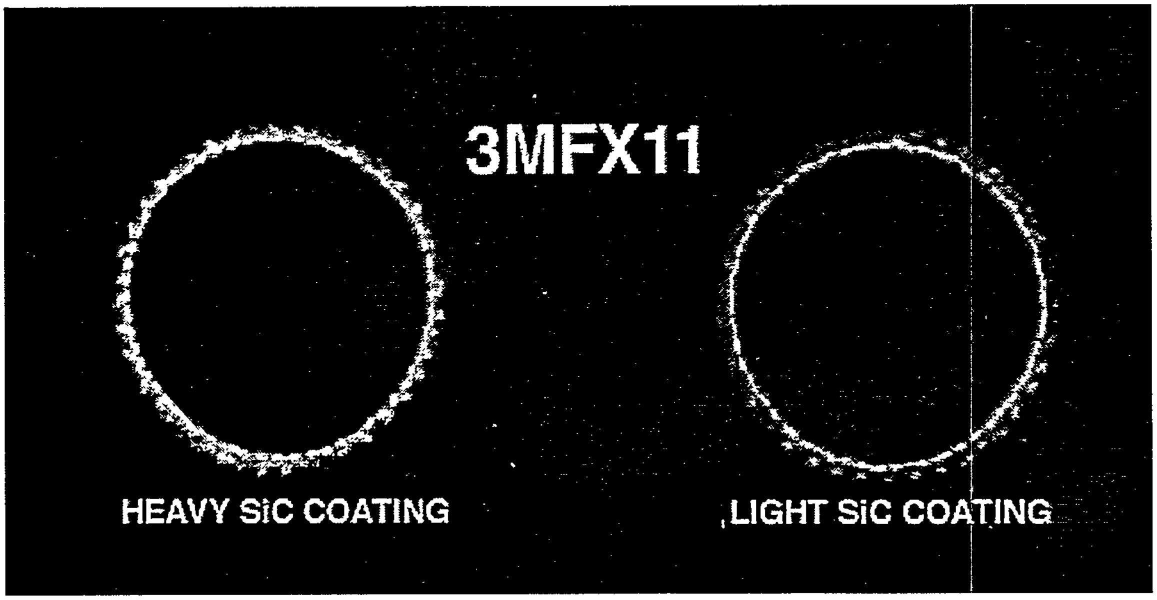

Fig. 3. Typical X-ray computed tomographic images of the 3M hot-gas filters; (a) heavy SiC coating, and (b) light SiC coating

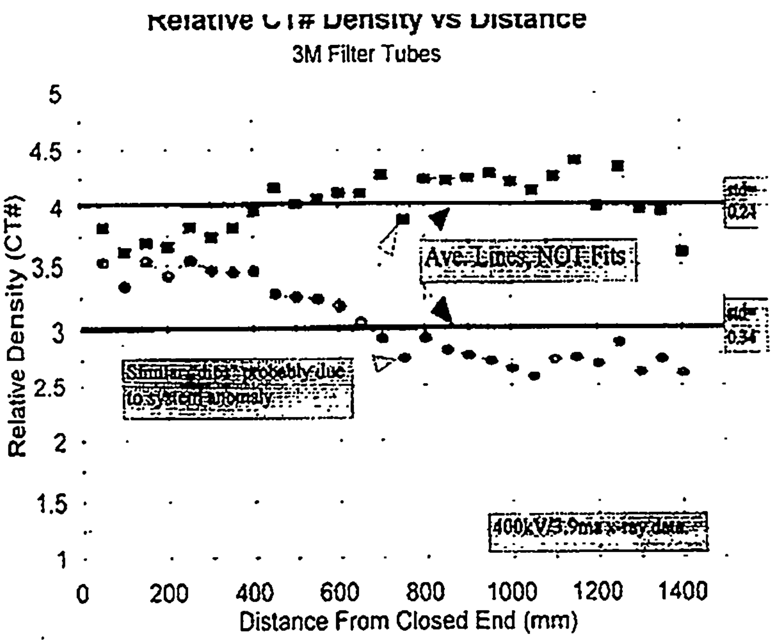

Fig. 4. Variations in relative axial density of two 3M hot-gas filters

Joints

To study the NDE of ceramic-to-ceramic joints, we used a butt-joint monolithic 15-cm-diameter SiC tube that was joined for use in a corrosion test facility at Oak Ridge National Laboratory. The tube (Fig.5) was studied by two NDE methods: XCT and impact acoustic resonance (IAR).[9] The XCT method was used to determine if large voids existed at the joint and IAR was used to the joint establish if the joint was solid, which perhaps could be considered a function of the elastic properties.

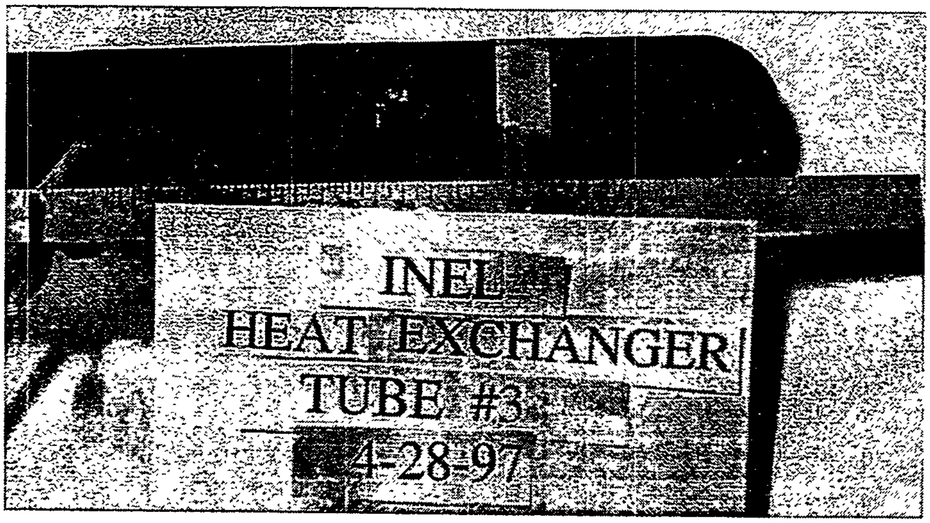

Fig. 5. Photograph of 15-cm-diameter SiC/SiC butt-joined tube

A 450 KVp XCT system was used to obtain a set of XCT images through the joint region. The XCT "slices", which were 500 μm thick, were taken sequentially, with 300-μm off-sets. Three XCT images of the joint are shown in Fig. 6, which reveals several features,

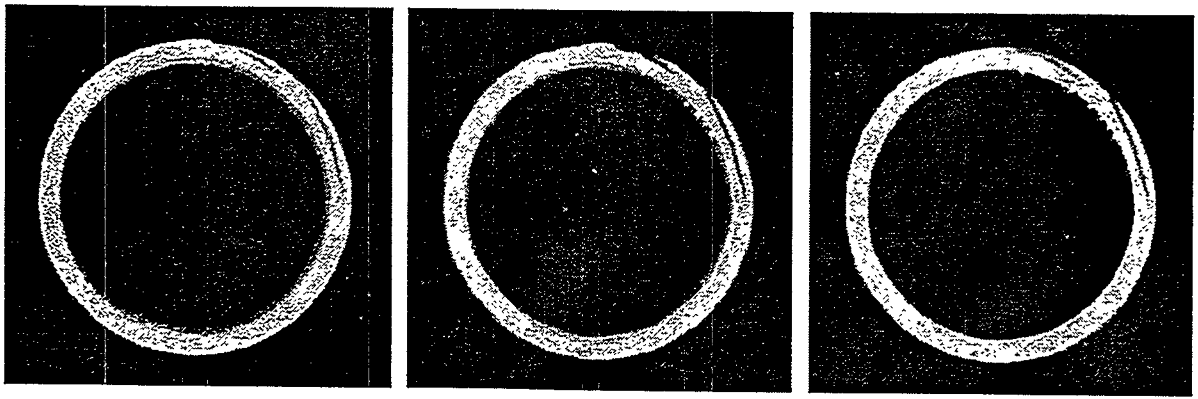

Fig. 6. X-ray CT images through butt joint of 15cm SiC/SiC tube;

(a) open unjoined areas, (b) less dense regions, and (c) so-called drop-through or regions where the "weld" material dropped to the inside. This suggests that XCT can be used to detect regions that lack penetration and, perhaps, density variations in the joint.

In the IAR method, the specimen is struck with an instrumented hammer and the resultant acoustic signal is detected by a microphone. Both the signal and the instrumented hammer are digitized in a 100-Mhz dual-channel digitizer. Impact excitations are used at uniform distances around the tube on both sides of the buttjoint. The collected data are then analyzed for changes. Results to date correlate with the voids detected by XCT, in that poorly joined regions show significantly differing frequency peaks.

Thermal-Barrier Coatings

For the work on TBCs, nine 20-mm-diameter specimens were coated with René N5 substrate, PtAl bond coat, and ZrO_2 by electron-beam physical vapor deposition. Coatings of three thicknesses, 125 µm, 190 µm, and 254 µm , were applied. In addition, two full-scale aeroderivative turbine blades that had been coated were also studied.

An area of technical interest is uniformity of coating thickness. One-sided flash thermal imaging was used to study the three coating thicknesses and the turbine blades. Sensitivity to thickness can be attaineb by obtaining time-dependent images and using digital image processing. Figure 7 shows data for each specimen and both turbine blades. These data suggest that the blades are covered with have 125-µm TBCs.

While not verified destructively, it has been suggested by the suppliers that, indeed, the typical coating thickness would be expected to be in the range of 125 µm. Thus, there is reason to believe that the thermal-flash method a reasonably be used for full field thickness measurement.

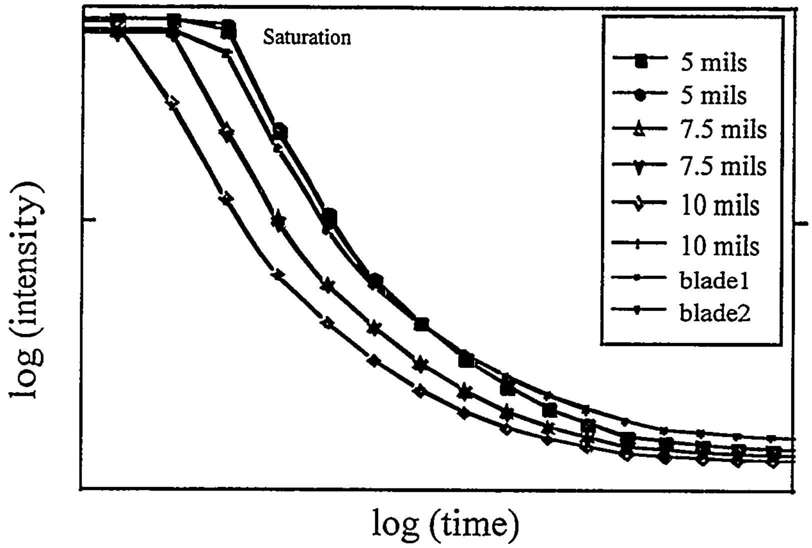

Fig. 7. Sensitivity of flash infrared imaging to EB-PVD thickness of coating applied by (Substrate is René N5 and bond coat is Pt A1)

ACKNOWLEDGMENTS

This research was sponsored by the Office of Fossil energy, Advanced Research and Technology Development materials Program [DOE/FE AA 15 10 10 0, Work Breakdoen Structure Element ANL-1], U.S. Department of Energy, under Contract W-31-109-Eng-38. B. Rabin of INEL provided joined SiC/SiC specimens, R. Bruce of GE Aircraft Engines, R. Orenstein of GE Power Generation, and B. Seth of Westinghouse Power Systems provided thermal barrier coating specimens

REFERENCES

1. B. H. Rabin, *Joining of SiC Ceramics and SiC/SiC Composites*, in Proc. of the 9th Annual Conf. on Fossil Energy Materials, Oak Ridge National Laboratory Report, ORNL/FMP-95/1, 1995, pp. 41-44.

2. B. H. Rabin and G. A. Moore, *Joining of SiC Ceramics and SiC/SiC Composites*, in Proc. of the 7th Annual Conf. on Fossil Energy Materials, Oak Ridge National Laboratory Report ORNL/FMP-93/1, 1993, pp. 33-42.

3. W. A. Ellingson, E. R. Koehl, H. P. Engel, J. A. Wilson, and J. B. Stuckey, *Development of Nondestructive Evaluation Methods for Structural Ceramics*, in Proc. of the 10th Annual Conference on Fossil Energy Materials, Oak Ridge National Laboratory Report, ORNL/FMP/-96-1, Conf. 9605167, August 1996, pp. 27-37.

4. J. B. Stuckey, Development of Non-Contact Thermal Imaging Methods for Characterizing Advanced Ceramics, Masters Thesis submitted to Northwestern University (May 1997).

5. J. G. Sun, W. A. Ellingson, J. S. Steckenrider, and S. Ahuja, *Application of Optical Scattering Methods to Detect Damage in Ceramics,* Chapter 5 in Machining of Ceramics and Composites, Part IV, (to be published 1997)

. Private communication, B. F. Goodrich-Supertemp, January 1996.

6. W. A. Ellingson, M. W. Vannier, and D. P. Stinton, *Application of X-ray Computed Tomography to Ceramic/Ceramic Composites*, in Characterization of Advanced Materials, E. Henneke, ed., Plenum Press, N.Y., 1991, pp. 9-25.

7. E. A. Sivers, P. A. Holloway, and W. A. Ellingson, *Obtaining High-Resolution Images of Ceramics from 3D X-ray Microtomography by Region-of-Interest Reconstruction*, in Ceramic Engineering and Science Proceedings, Vol. 14, No. 17-18, 1993, pp. 463-472.

8. E. A. Sivers, *Use of Multiple CT Scans to Accommodate Large Objects and Stretch Dynamic Range of Detectability*, in Nuclear Instruments and Methods, Phy. Res. B., Vol. 99, 1995, pp. 761-764.

9. P. R. Raju, J. R. Patel, and U. K. Vaidya, *Characterization of Defects in Graphite-Fiber Based Composite Structures Using the Acoustic Impact Technique (AIT),* J. Test Vib., Vol. 21, No. 5, 1993, pp. 377-395.

SOLID STATE ELECTROLYTE SYSTEMS

L. R. Pederson, B. L. Armstrong, T. R. Armstrong, J. L. Bates, G. W. Coffey,
G. H. Hsieh, J. Li, T. O. Mason*, A. S. Rupaal**, J. W. Stevenson, and W. J. Weber

Pacific Northwest National Laboratory
P.O. Box 999
Richland, WA 99352

*Northwestern University
Evanston, IL 60208

** Western Washington University
Bellingham, WA 98225

ABSTRACT

Lanthanum gallates are a new family of solid electrolytes that exhibit high ionic conductivity and are stable to high temperatures. Compositions have been developed that are as much as a factor of two more conductive than yttria-stabilized zirconia at a given temperature, through partial replacement of lanthanum by calcium, strontium, and/or barium and through partial replacement of gallium by magnesium. Oxide powders were prepared using combustion synthesis techniques developed in this laboratory; these were sintered to >95% of theoretical density and consisted of a single crystalline phase. Electrical conductivities, electron and ion transference numbers, thermal expansion, and phase behavior were evaluated as a function of temperature and oxygen partial pressure. A key advantage of the use of lanthanum gallate electrolytes in solid oxide fuel cells is that the temperature of operation may be lowered to perhaps 800°C, yet provide approximately the same power density as zirconia-based cells operating at 1000°C.

Ceramic electrolytes that conduct both oxygen ions and electrons are potentially useful to passively separate pure oxygen from an air source at low cost. In such materials, an oxygen ion flux in one direction is charge-compensated by an opposing electron flux. We have examined a wide range of mixed ion and electron conducting perovskite ceramics in the system $La_{1-x}M_xCo_{1-y-z}Fe_yN_zO_{3-\delta}$, where M=Sr,Ca, and Ba, and N=Pr, Mn, Ni, Cu, Ti, and Al, as well as mixed conducting brownmillerite ceramics, and have characterized oxygen permeation behavior, defect chemistry, structural and phase stability, and performance as cathodes.

INTRODUCTION

Two principal glasses of oxygen ion conductors are being developed: (1) ceramics that predominantly conduct oxygen ions, and (2) ceramics that conduct both electrons and oxygen ions. The first type find application as the electrolyte in solid oxide fuel cells, as oxygen sensors, and as oxygen separation membranes. The second type are useful as passive oxygen separation membranes, as the membrane in a catalytic reactor to partially oxidize hydrocarbons or to produce synthesis gas, and as the electrode in a fuel cell.

Lanthanum gallate ceramics comprise a new class of solid electrolytes of the first type, with high electrical conductivities and excellent stabilities at high temperatures.[1-5] Some compositions give electrical conductivities a factor of two to three greater than found for yttria-stabilized zirconia, the most widely utilized solid electrolyte.[3-5] Lanthanum gallates exhibit an ABO_3-type perovskite structure, one that is quite amenable to cation substitution. By substituting strontium, calcium, and/or barium for lanthanum and by substituting magnesium for gallium in this structure, oxygen vacancy populations can be adjusted and electrical conductivities altered.

Compositions in the $(La,M)(Co, Fe)O_{3-x}$ system, where M = Sr, Ca, Ba, and Pr, also are ABO_3-type perovskites whose properties can be tailored through compositional variations. These ceramics exhibit mixed oxygen ion and electron conductivity.[6-8] Although the oxygen ion current is usually less than one percent of the overall current, the oxygen ion conductivity often exceeds that of yttria-stabilized zirconia by a significant margin. Partial substitution of divalent cations for lanthanum on the A-site and substitution of cobalt for iron enhances oxygen ion conductivity, generally at the expense of structural stability. Similar in structure to perovskites, certain brownmillerites are mixed conducting ceramics showing good stability under conditions necessary for the production of synthesis gas.[9,10]

LANTHANUM GALLATE ELECTROLYTES

Lanthanum gallate powders were prepared using the glycine-metal nitrate combustion synthesis method, which is particularly well-suited to make homogeneous, multicomponent metal oxide products.[11] Samples were calcined in air at 650°C to remove any residual carbon, isostatically dry pressed at ≈140 MPa, and then sintered at temperatures up to 1500°C. Phase purity was determined by x-ray diffraction, thermal expansion behavior evaluated using vertical dilatometry, electrical conductivity determined using 4-probe pulsed dc methods, and transference numbers determined as a function of oxygen partial pressure using the voltage step method.

Using stoichiometric mixes of the metal nitrates and glycine in the precursor solution, approximately 90 percent by weight of lanthanum strontium gallium magnesium oxide compositions were converted to the desired perovskite phase following calcination for a half hour at 650°C. That amount increased to 94, 97, and 99 weight percent, respectively, after calcination to 1000, 1200, and 1400°C. High A-site substitution resulted in larger fractions of non-perovskite phases being present in the powders. Appropriately calcined powders sintered densities of greater than 97 percent of the theoretical value when heated from 1400 to 1500°C. When heated at temperatures greater than 1550°C, sintered densities actually were diminished. This was shown to be due to the formation of a suboxide of gallium, Ga_2O, which forms pressurized gas pockets within the sample.

Thermal expansion behavior was evaluated in the temperature range of 20 to 1200°C. In general, thermal expansion coefficients (TEC) were similar to that obtained for yttria-stabilized zirconia ($\approx 10.4 \times 10^{-6}$ cm/cm-°C). Values ranged from 11.3×10^{-6} cm/cm-°C for $La_{0.9}Ca_{0.1}Ga_{0.8}Mg_{0.2}O_{3-\delta}$ to 12.1×10^{-6} cm/cm-°C for $La_{0.8}Sr_{0.2}Ga_{0.8}Mg_{0.2}O_{3-\delta}$. Thermal expansion coefficients increased with increased acceptor content, expected since the dopants strontium and magnesium have larger ionic radii than the ions they replace in the structure.

The electrical conductivity of strontium-substituted lanthanum gallate electrolytes were typically two or more times higher than yttria-stabilized zirconia, particularly at lower temperatures. Electrical conductivities of several substituted lanthanum gallate compositions are given in Figure 1. The designation "1020" refers to 10% Sr substitution for La and 20% Mg substitution for Ga. A comparison of electrical conductivities for various lanthanum gallates are also given in Table 1. Within the composition range studied, electrical conductivity increased with increased acceptor

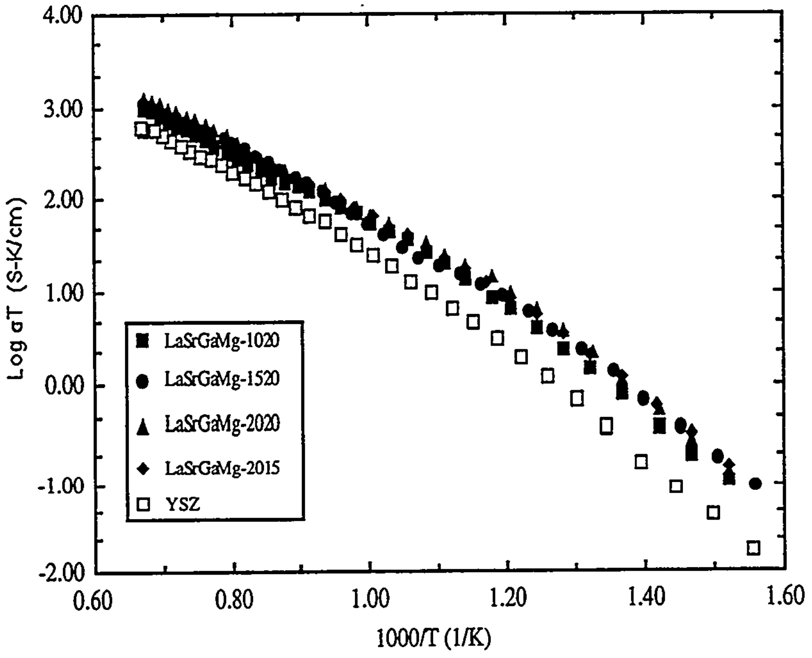

Figure 1. Electrical conductivity of lanthanum gallate compositions versus reciprocal temperature.

content (Sr and Mg substitution), the result of a concomitant increase in the concentration of oxygen vacancies. Calcium and barium-substituted lanthanum gallates were also studied. Barium-substituted compositions behaved similarly to the strontium-substituted analogs; calcium-substituted analogs were less conductive.

Table 1. Comparison of electrical conductivity of lanthanum gallate with yttria-stabilized zirconia at 600 and 1000°C

Composition	σ, 600°C	σ/σ_{YSZ}, 600°C	σ, 1000°C	σ/σ_{YSZ}, 1000°C
10% Sr, 20% Mg	$1.5x10^{-2}$	2..5	$1.5x10^{-2}$	1.4
15% Sr, 20% Mg	$1.5x10^{-2}$	2.5	$1.5x10^{-2}$	2.0
20% Sr, 15% Mg	$1.8x10^{-2}$	3.0	$1.5x10^{-2}$	1.7
20% Sr, 20% Mg	$2.0x10^{-2}$	3.3	$1.5x10^{-2}$	2.2
10% Ca, 20% Mg	$0.1x10^{-2}$	0.17	$1.5x10^{-2}$	0.33
20% Ca, 20% Mg	$0.4x10^{-2}$	0.67	$1.5x10^{-2}$	0.67
10% Ba, 20% Mg	$1.8x10^{-2}$	3.0	$1.5x10^{-2}$	1.7
yttria-zirconia	$0.6x10^{-2}$	1	$1.5x10^{-2}$	1

The lanthanum gallates are predominantly oxygen ion conductors, but not exclusively so. Transference numbers were determined for lanthanum gallate electrolytes using the voltage step method as a function of temperature and oxygen partial pressure. Platinum or gold blocking electrodes were applied to prevent the passage of a steady-state oxygen ion current. Electronic transference number results for $(La_{0.9}Sr_{0.1})_{0.95}Ga_{0.8}Mg_{0.2}O_{3-\delta}$, an A-site deficient composition, are given in Figure 2. These electrolytes are unusual in that the electronic contribution to overall conductivity first rose and then fell with decreased oxygen partial pressure.

Partial reduction of gallium from a formal +3 state to a +2 state is believed responsible for trends shown in Figure 2. Ga(III) has a $4s^0$ electron configuration, while Ga(II) has a $4s^1$ configuration. The highest possible electronic conductivity via small polaron hopping will occur when there are equal populations of Ga(II) and Ga(III), since Ga(II) provides electrons for conduction while Ga(III) provides holes. Conduction from one Ga(II) site to another Ga(II) site is less favored, since spin pairing of electrons would be required.

In summary, lanthanum gallate electrolytes hold promise for use as the electrolyte in a

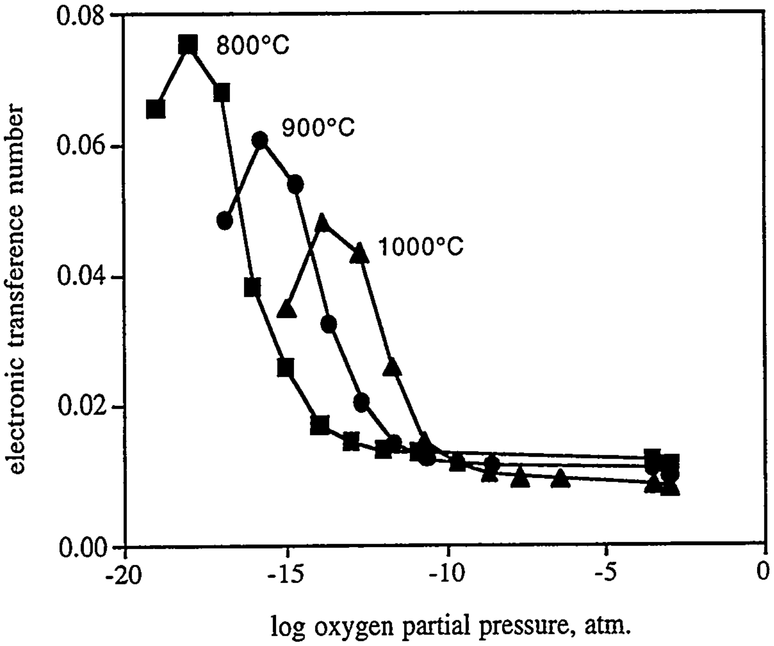

solid oxide fuel cell operating at low temperatures, among other applications. Some compositions are more conductive than yttria stabilized zirconia, particularly at low temperatures. They show predominantly ionic conduction and are relatively stable to very low oxygen partial pressures.

Figure 2. Electronic transference numbers for a non-stoichiometric lanthanum gallate composition, $(La_{0.9}Sr_{0.1})_{0.95}Ga_{0.8}Mg_{0.2}O_{3-\delta}$, as a function of oxygen partial pressure.

MIXED CONDUCTING COBALT IRON OXIDE CERAMICS

A wide range of perovskite compositions in the system $La_{1-x}M_xCo_{1-y-z}Fe_yN_zO_{3-\delta}$, where M=Sr,Ca, and Ba, and N=Pr, Mn, Ni, Cu, Ti, and Al, and a brownmillerite ceramic, $SrFeCo_{0.5}O_{2.5-\delta}$, have been prepared and have been characterized with respect to oxygen permeation behavior, defect chemistry, structural and phase stability, and performance as cathodes. Ceramic powders were synthesized using glycine-nitrate combustion methods. Compacts were uniaxially and then isostatically pressed to 140 MPa, followed by sintering at 1150 to 1250°C. Sintered densities were >95% of theoretical.

In the $La_{1-x}M_xCo_{1-y-z}Fe_yN_zO_{3-\delta}$ perovskite system, electronic conductivities at a given temperature were much higher than the corresponding ionic conductivities, as shown in Table 2. Despite oxygen ions being a minority carrier in these ceramics, the oxygen ion conductivity exceeded that of yttria-stabilized zirconia for many compositions. Compositions most highly substituted with strontium gave oxygen ion conductivities nearly a factor of ten higher than zirconia at the same temperature.

Table 2. Ionic and electronic conductivities for mixed conducting ceramics at 900°C.

Composition	Ionic Conductivity (S/cm)	Electronic Conductivity (S/cm)	Oxygen Ion Transference Number
LaSrCoFe-6428	0.23	252	9×10^{-4}
LaSrCoFe-4628	0.40	219	2×10^{-3}
LaSrCoFe-2828	0.62	120	5×10^{-3}
LaSrCoFe-2882	0.87	310	3×10^{-3}
LaCaCoFe-4628	0.03	52	6×10^{-4}
LaCaCoFe-4682	0.01	296	3×10^{-5}
LaBaCoFe-6428	0.01	123	8×10^{-5}
LaBaCoFe-4628	0.33	57	6×10^{-3}
LaBaCoFe-2828	0.37	19	2×10^{-2}

From the temperature dependence of oxygen permeation, oxygen partial pressure gradient, and sample dimensions, activation energies for ionic conduction were calculated. These are given in Table 3 for a number of different perovskite compositions. Unlike yttria stabilized zirconia or lanthanum gallate electrolytes, the derived activation energy for ionic conduction in the mixed conducting perovskites contains a contribution due to oxygen vacancy formation as temperature is increased. The ionic conductivity in any solid electrolyte is the product of three terms: carrier concentration, carrier charge, and carrier mobility. Carrier concentrations were deduced independently from a combination of thermogravimetric analyses (oxygen weight loss) as a function of temperature and iodometric titration. This enabled carrier mobilities to be deduced and activation energies associated with oxygen vacancy mobility to be calculated. Expressions for vacancy mobility and the diffusion coefficient are also included in Table 3. All but a barium-substituted composition gave activation energies associated with ion mobility in the range of 0.55 to 0.80 eV, which appear in the exponential terms given for mobility and diffusion coefficients in Table 3. Clearly, a significant portion of the apparent activation energy for oxygen permeation derives from the formation of additional oxygen vacancies.

A brownmillerite ceramic, $SrFeCo_{0.5}O_{3.25-\delta}$, has been studied for possible use as the membrane in a reactor to prepare synthesis gas (carbon monoxide and hydrogen) from the reaction of natural gas with oxygen.[10] This particular composition shows relatively good

Table 3. Conduction parameters for mixed ion and electron-conducting electrolytes

Composition	Activation Energy for Ion Conduction (eV)	Mobility (cm^2/V-s)	Diffusion Coefficient (cm^2/s)
LaSrCoFe-6428	1.30	(209/T) exp (-0.55/kT)	0.009 exp (-0.55/kT)
LaSrCoFe-4628	0.95	(269/T) exp (-0.63/kT)	0.012 exp (-0.63/kT)
LaSrCoFe-2828	0.85	(436/T) exp (-0.69/kT)	0.020 exp (-0.69/kT)
LaSrCoFe-2882	0.66	(129/T) exp (-0.56/kT)	0.005 exp (-0.56/kT)
LaBaCoFe-6428	1.64	(10700/T) exp (-1.36/kT)	0.462 exp (-1.36/kT)
LaBaCoFe-4628	0.90	(551/T) exp (-0.77/kT)	0.024 exp (-0.77/kT)
LaBaCoFe-2828	0.65	(78/T) exp (-0.59/kT)	0.003 exp (-0.59/kT)

stability at high temperatures even in the reducing conditions that exist on the natural gas side of the membrane. Transport properties for this ceramic have not been well established previously, particularly in reducing environments; such information is needed to model membrane performance. For that reason, transference numbers for as a function of oxygen partial pressure and temperature were evaluated using the voltage step polarization method. Gas buffer mixtures of hydrogen and carbon dioxide were used to control the oxygen partial pressure to as low as 10^{-20} atmospheres.

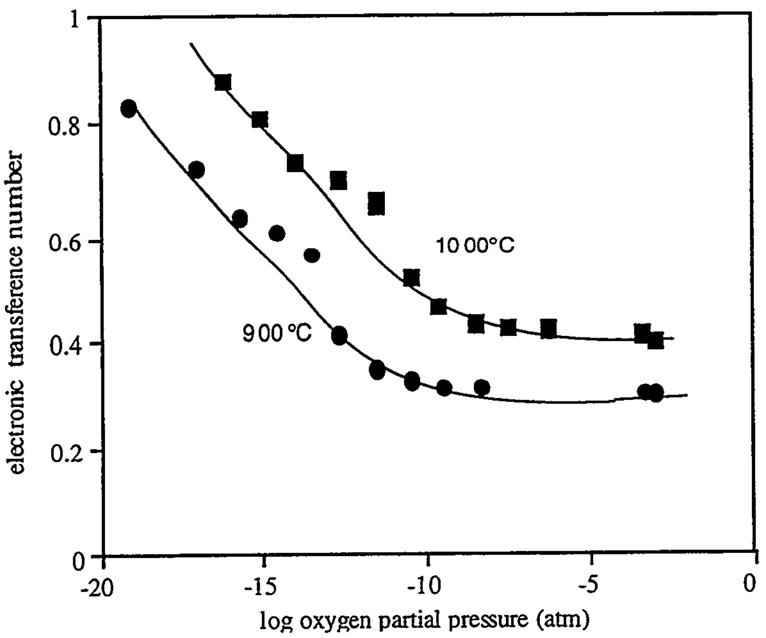

Figure 3. Electronic contribution to the overall conductivity for the ceramic $SrFeCo_{0.5}O_{3.25-\delta}$ versus oxygen partial pressure.

Ionic and electronic contributions to the overall electrical conductivity of the composition $SrFeCo_{0.5}O_{3.25-\delta}$ were similar for oxygen partial pressures greater than 10^{-10} atm, as is shown in Figure 3. The electronic contribution increased substantially for oxygen partial pressures smaller than 10^{-10} atm, typical of an n-type semiconductor. Enhanced electronic conductivity in an environment of low oxygen partial pressure is due to the partial reduction of iron and cobalt from trivalent to divalent states.

Because electronic conduction could well be the limiting factor in determining passive oxygen flux for the brownmillerite ceramic $SrFeCo_{0.5}O_{3.25-\delta}$, this ceramic would be less effective than the mixed conducting perovskite compositions discussed above for the separation of oxygen from air. In configurations needed to prepare synthesis gas from methane, electronic conduction will not limit oxygen fluxes through the brownmillerite membrane, however, as is clear from Figure 3. In the preparation of synthesis gas, stability under reducing environments becomes an important factor, not just oxygen ion conductivity.

REFERENCES

1. T. Ishihara, H. Matsuda, Y. Mizuhara, and Y. Takita, Solid State Ionics, 70/71, 234 (1994).

2. T. Ishihara, H. Matsuda, and Y. Takita, Solid State Ionics, 79, 147 (1995).

3. M. Feng and J. B. Goodenough, Eur. J. Solid State Inorg. Chem. 31, 663 (1994).

4. P. Huang and A. Petrick, J. Electrochem. Soc. 143, 1644 (1996).

5. J. W. Stevenson, T. R. Armstrong, L. R. Pederson, and W. J. Weber, J. Electrochem. Soc. (1997, submitted).

6. Y. Taraoka, T. Nobunaga, K. Okamoto, N. Miura, and N. Yamazoe, Solid State Ionics 48, 207 (1991).

7. H. Bouwmeester, H. Kruidhof, and A. Burggraff, Solid State Ionics 72, 185 (1994).

8. J. W. Stevenson, T. R. Armstrong, R. D. Carneim, L. R. Pederson, and W. J. Weber, J. Electrochem. Soc. 143, 2722 (1996).

9. U. Balachandran, J. T. Dusek, S. Sweeney, R. Poeppel, R. L. Mieville, P. Maiya, M. Kleefisch, S. Pei, T. Kobylinski, C. A. Udovich, and A. Bose, Am. Ceram. Soc. Bull. 74, 71 (1995).

10. C. A. Udovich, M.S. Kleefisch, A. Bhattacharrya, S. Pei, U. Balachandran, J. T. Dusek, and R. L. Mieville, Proc. 1997 Spring Nat. AIChE Meeting, Houston, TX (1997).

11. L. A. Chick, L. R. Pederson, G. D. Maupin, J. L. Bates, L. E. Thomas, and G. J. Exarhos, Materials Lett. 10, 6 (1990).

ACTIVATION AND MICROPORE STRUCTURE OF CARBON-FIBER COMPOSITES

M. Jagtoyen, F. Derbyshire and G. Kimber
University of Kentucky Center for Applied Energy Research,
3572 Iron Works Pike, Lexington KY 40511-8433, USA.

INTRODUCTION

Rigid, high surface area activated carbon fiber composites have been produced with high permeabilities for environmental applications in gas and water purification. The project involves a collaboration between the Oak Ridge National Laboratory (ORNL) and the Center for Applied Energy Research (CAER), University of Kentucky[1,2]. The main focus of recent work has been to find a satisfactory means to uniformly activate large samples of carbon fiber composites to produce controlled pore structures. Processes have been developed using activation in steam and CO_2, and a less conventional method involving oxygen chemisorption and subsequent heat treatment. Another objective has been to explore applications for the activated composites in environmental applications related to fossil energy production.

Activation

Activation in steam and CO_2 has been conducted under different conditions to produce small samples that are activated relatively uniformly throughout the structure of the artefact. However, with large composites there are constraints on the use of a reactive gas in attaining a uniform partial pressure and temperature through the body of the composite. To surmount this problem, different reactor configurations were investigated. In the more successful arrangement, steam or CO_2 is introduced at several points along the length of the composite to provide a uniform flow of activating agent.

A less conventional method of oxygen chemisorption/heat treatment was selected as an alternative activation technique. This method was first described by Nandi et al[3] and more recently has been the subject of a patent by Quinn et al[4]. The procedure involves the chemisorption of oxygen at low temperatures (e.g<250°C) followed by heat treatment in nitrogen or other inert gas at temperatures up to about 900°C. It appears that slow oxygen chemisorption can produce a uniform distribution of surface oxygen groups that are then thermally decomposed to remove carbon as CO and CO_2. Because of the limited oxygen uptake at low temperatures it is necessary to complete several cycles before there is appreciable surface area development. The results will show that very uniform BET surface areas are developed throughout the composite.

Applications

The application of the activated composites to water treatment was studied last year[5]. More recent work has focused on their possible application in evaporative loss control devices. The Amendments to the Clean Air Act of 1998 have enforced the use of more efficient carbon canisters in US automobiles to recover evaporated gasoline. The standard evaluation method for this application is the butane working capacity test which is a carbon's ability to adsorb and desorb gasoline light ends. The two most important criteria for high butane working capacity carbons are high density and a large proportion of pores in the small mesopore range (from 20-50 A). Several other practical applications of activated carbons also require wide pores, such as cyclic adsorption and desorption of volatile organic compounds (VOCs). Pitch-based carbon fibers tend to have narrow micropores and are therefore not normally useful for such applications. Hence, attempts have been made to examine the possibility of producing fibers with wider pores through varying activation conditions and fiber precursors.

EXPERIMENTAL

Composite Preparation

Carbon fiber composites are prepared at ORNL [1] by vacuum molding from water slurries containing powdered phenolic resin and chopped isotropic petroleum pitch fibers, (P-200, ~ 17.5 μm diameter, average length 380μm, supplied by courtesy of Ashland Carbon Fibers Division, Ashland Inc.). The slurry is vacuum molded into tubular, plate or rod configuration, followed by drying, curing, and carbonization to about 650°C. The carbon fiber composites are supplied to the CAER in the form of plates (28x12x1.5cm), rectangular or cylindrical shapes[5].

Activation

In attempting to uniformly activate relatively large composite samples (4.5" diameter, 6" long) in steam or CO_2, different reactor configurations and conditions have been investigated. Originally a Lindberg Blue M laboratory box furnace was used, in which the specimen was contained in a sealed stainless steel cylindrical chamber of diameter 6", and height 6". Water was pumped into the reaction chamber and vaporized at the bottom when steam flowed upwards through a perforated stainless steel plate, and was distributed around the composite.

In a more successful arrangement, steam is introduced at several points along the length of the composite. A 4900 W Lindberg furnace was acquired with an inconel chamber of dimensions 6"x 4" x 12". The activating agent, steam or CO_2 was supplied through 4 connected stainless steel distributor tubes that run along the four long corners of the furnace, Figure 1. The distributors are drilled with holes 2 mm in diameter and spaced about 1" apart along their length. The end result is to create a uniform flow of the activating agent in the chamber and around the sample. The design was developed from previous experience, where uniform activation was achieved with small samples by introducing the steam at different points around the sample. By this configuration concentration gradients in the activating gas are minimized.

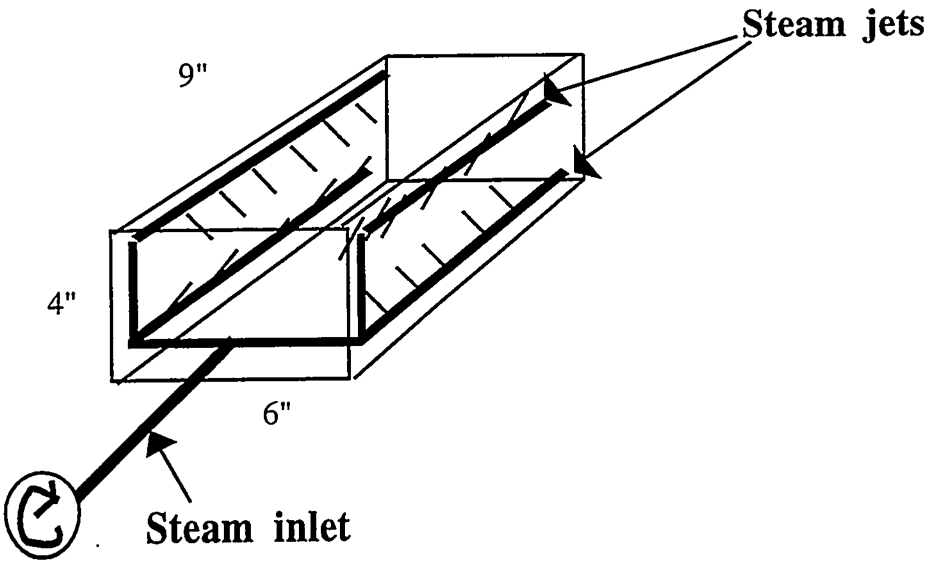

Figure 1: Configuration of steam supply in activation furnace.

Steam activation was carried out at temperatures from 800-900°C for reaction times of 0.5-3 hrs. The flow rate of water was 50-140cc/hr and of nitrogen, 2-3 lpm. Activation in CO_2 was carried out at temperatures from 850-950°C, for reaction times of 1-3 hours. The flow rate of pure CO_2 was varied from 2-3 l/min with the same multiple point gas introduction configuration.

A third method of activation involved a combination of oxygen chemisorption and carbonization. The samples were exposed to an atmosphere of 50% O_2 in N_2 at temperatures ranging from 170-240°C for periods of 1-6 hours. They were subsequently heat treated in nitrogen to 850-925°C, for 1-3 hours. The removal of carbon as carbon oxides should lead to a uniform surface area development. It is known that CO_2 is released at temperatures from 300-800°C with a maximum at about 350°C while CO is released at temperatures from 500-900°C with a maximum at 700°C.

Characterization

Porosity Surface area and pore size distributions were measured on a 10 port automated surface area analyzer, OMNISORB 610. The high efficiency of the instrument allows the measurement of surface areas, as well as the characterization of pore sizes down to 4 A, using nitrogen at 77K as the adsorbate. Surface areas were determined from the isotherms by the BET method, and pore volumes by the D-R method (micropores) and the BJH method (mesopores)[6].

Butane Working Capacity Test The butane working capacity (BWC) was developed as a measure of the effectiveness of activated carbons that are used to trap hydrocarbons released by evaporative losses from vehicle fuel systems (used in evaporative loss control devices, or ELCDs). It is also a useful indication of the properties of activated carbons with respect to other applications. Essentially, the BWC is the difference between the saturation adsorptive capacity of butane, and the amount retained upon the carbon after purging under specified conditions. The retained butane is too strongly adsorbed to allow facile desorption. The tests were performed according to ASTM method D5228-92.

DISCUSSION OF CURRENT ACTIVITIES

Uniform Activation by Steam

Sample SM12, a cylinder of carbon fiber composite produced at ORNL of diameter 11.4 cm and length 21 cm was divided into three sections each 6.9-7.8 cm long with 11.4 cm diameter. The sections weighed 140-180 grams depending on their length. In order to try to achieve uniform activation it was decided to progressively lower the normal steam activation temperature of 875°C by steps of 25°C down to 800 °C. The samples were all activated to a burnoff of 24-28% under the conditions given in Table 1. The surface area distributions through the three samples are given in Figures 2a-c.

The activation is most uniform under conditions of low temperature(800°C) and long reaction times (14 hrs), which is attributed to the low reaction rate that allows the steam to diffuse to the center of the sample before reacting. Hence, the center of the sample is activated to nearly the same extent as the periphery. The mean rate of activation (burnoff/g sample/ minute) is shown in Table 1. The reaction rate increases 27% upon increasing the temperature from 800 to 825°C and by another 50 % upon increasing temperature from 825 to 850°C. The samples do not exhibit stress cracks when activated at 800°C while at 850°C, stress cracks occur. The activation energy for steam activation was determined to be 126kJ/mol by plotting the rate of carbon burnoff in an Arrhenius plot. This is consistent with data in the literature. The activation energy is slightly higher than for the activation of coal and wood based carbons but lower than the activation energy for the activation of carbon fibers[7]. The activation energy for steam activation will be compared to that of CO_2 activation in future work. Further studies will concentrate on reducing activation time and achieving lower standard deviations in surface area distribution by further changing furnace configurations and conditions, and by the application of other techniques that are not discussed here.

Table 1: Conditions and results of steam activation at different HTT.

ID	HTT (°C)	time (hr)	start wt (g)	burnoff(B.O.) (%)	rate of B.O. (g/g.hr)	St dev BET(%)
OR267	800	14	172	26.7	0.019	17
OR 272	825	10	189	24.2	0.024	20
OR 267	850	8	133	28.7	0.036	23

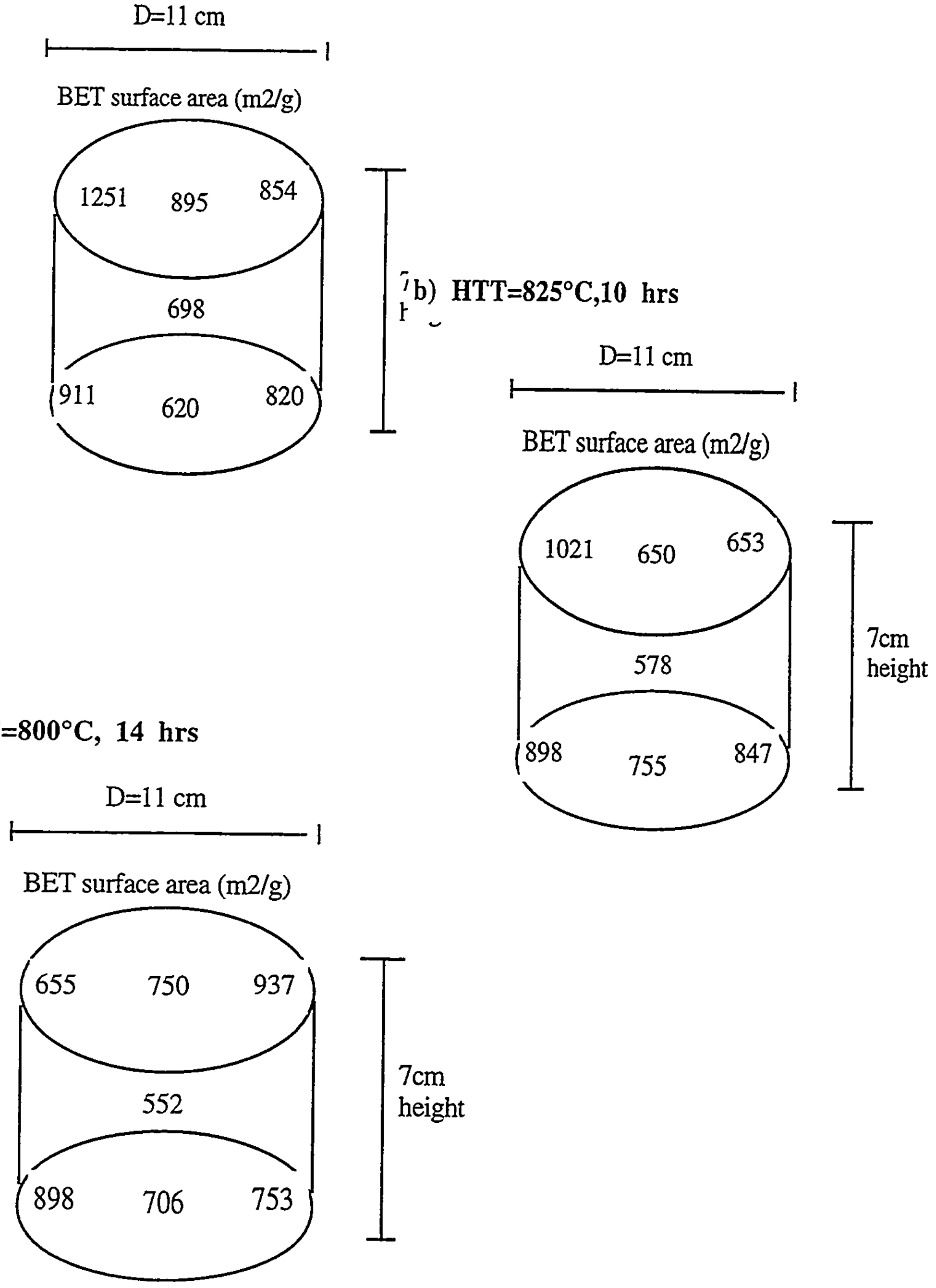
a) HTT=850°C, 8 hrs

b) HTT=825°C,10 hrs

c) HTT=800°C, 14 hrs

Figure 2 a-c: Distribution of BET surface area in samples activated at three different temperatures.

Uniform Activation by Chemisorption

The chemisorption of oxygen coupled with carbonization has been investigated as an activation technique for achieving uniform activation and a narrow pore size distribution. Since chemisorption is performed at temperatures where there is no carbon burn-off, the amount of oxygen uptake will reach a limiting value. As long as sufficient time is allowed for the oxygen to diffuse to all of the available surface, the extent of chemisorption should be uniform throughout the sample. Similarly, upon heat treatment, the removal of carbon as CO_x should also be uniform.

The chemisorption temperature was varied from 160-250°C. Increasing the chemisorption temperature from 225 to 250°C gave sufficient uptake of oxygen to triple the BET surface area upon heat treatment to 900°C, Table 2. The carbonization temperature was varied from 850-925°C. Heat treatment to 850°C is not sufficient to achieve significant microporosity, and heat treatment to 925°C also gives low surface area. The optimum upper temperature for maximizing the production of narrow micropores appears to be around 900°C. The surface area development in the composites was very uniform with deviation in surface area within the samples of only 3-6% for a chemisorption temperature of 250 and carbonization temperature of 900 or 925°C, Table 2.

In order to increase the surface area further, the cycles of oxygen adsorption and heat treatment were repeated several times. The surface area increased slightly with each step, to a maximum of about 440 m^2/g after a total burnoff of 9%, Figure 3. For each cycle of activation, new narrow micropores are opened. It is also found that the average pore width is reduced as the burnoff is increased, contrary to the case with steam activation. The standard deviation in surface area distribution is very small and close to the experimental reproducibility. A disadvantage when compared to steam activation is the extended processing time required

Table 2: Uniformity of activation of CFCMS by oxygen chemisorption/carbonization.

Sample#	**Oxidation**		**Carboniz.**		**Burnoff**	**Surface area**	**stdev**	**pore volume (cc/g)**	
	T(°C)	**t(hr)**	**T(°C)**	**t(hr)**	**(wt%)**	**(m^2/g)**	**(%)**	**micro**	**meso**
221	225	3	900	2	4	134	32	0.07	0.03
216	250	3	850	2	5	315	19	0.15	0.07
218	250	3	900	2	6	387	6	0.20	0.0
219	250	3	925	2	6	230	3	0.13	0.03

to achieve a certain burnoff. Activation times to achieve a 9 % burnoff are shown in Figure 4 for steam activation at different temperatures and oxygen chemisorption/carbonization. As can be seen from the Figure, a far longer processing time is needed to achieve the same burnoff for the chemisorption technique.

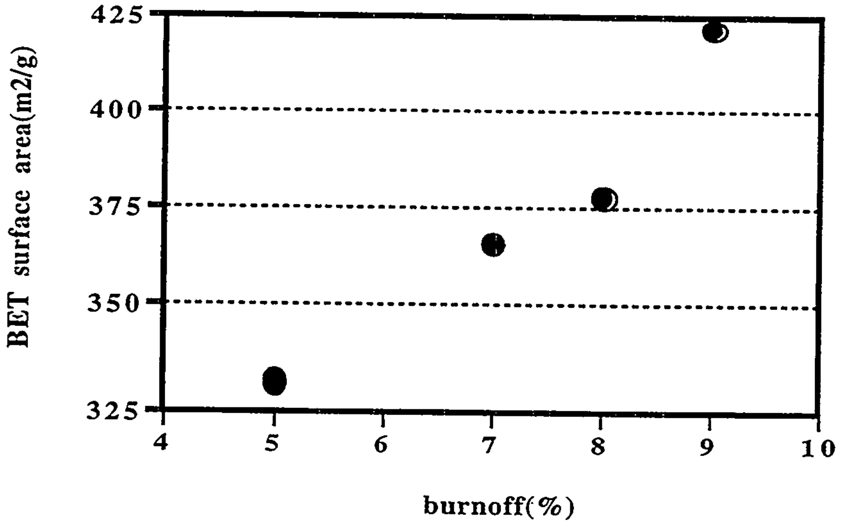

Figure 3: Increase in surface area for each cycle of oxygen chemisorption/carbonization. (Each data point shows a new cycle).

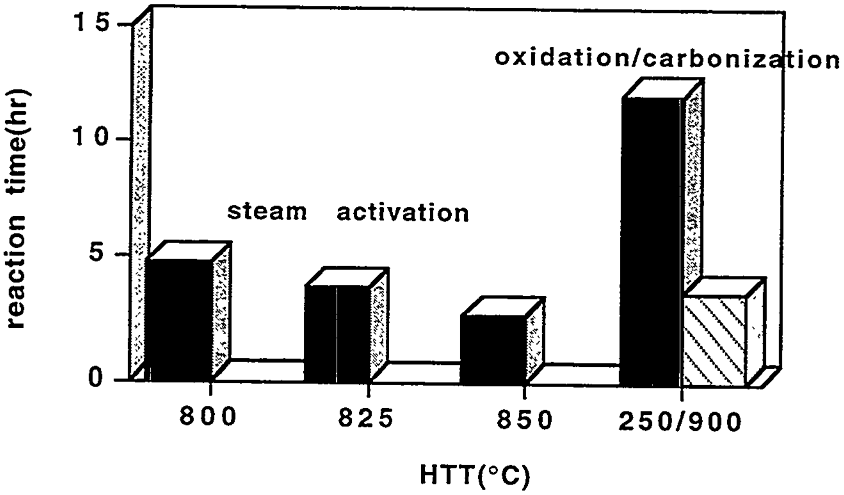

Figure 4: Reaction times for activation to 9% burnoff by steam activation at different HTT and oxygen chemisorption/carbonization.

Butane Working Capacity

Carbons for automobile evaporative control devices are required to have high BWC, as mentioned earlier. Pitch-based carbon fibers have narrow micropores and are therefore not normally useful for such applications. Because of this, carbon fiber composites were activated to high burnoffs in order to attempt to create wide porosity, Table 3. The surface area is high, up to 1800 m^2/g, but the composites still have a low proportion of mesopores. Another problem associated with activation to burnoffs higher than ~40% is that cracking and delamination of the composites occurs. A second obstacle to producing the performance expected of evaporative loss control device is the low density of the composites. The density of the standard composites as received from Oak Ridge is about 0.23 g/cc. In order to compete with the BWC of commercial carbons the density must be increased to around 0.35 - 0.4 g/cc. In the research reported here, samples SA 222 and SA 256 were ground and packed like a powdered bed to a density of 0.39 and 0.36 cc/g respectively. The results of the BWC tests are shown in Table 3. Both samples have butane adsorption capacities within the commercial range of evaporative loss control devices for automobiles, 9.7 and 8.6 g/100 ml. However, these composites also retain ~1.9 g butane per 100 ml of carbon, while wood based carbons show practically no retention.

In an attempt to improve the performance of the composites, an electrical current was applied to two of the composites during the air desorption stage to increase the sample temperature and aid desorption. A current of 4 A was applied for 25 seconds to give a temperature increase of about 50 °C. As can be seen in Table 3, the butane retentivity for sample OR 260 decreased from 1.8 g/100 ml to 0.8 g/100 ml when the current was applied. However, the BWC is still only 4.1 g/100 ml and highest BWC obtained on an activated composite was 5.5 g/100 ml which is still very low.

Even with the application of an electric current during the desorption stage, it does not seem feasible to produce a pitch-based carbon fiber composite with high performance for butane adsorption. The focus of future work will be to identify different precursor fibers that will give composites with higher butane working capacities.

Table 3: Butane Working Capacity (BWC) of activated carbon fiber composites

ID	SA222	SA 222B*	SA256*	OR 263**	OR 260	O 260**	Wood^^
BET surface area (m^2/g)	1380	1380	1057	1728	1126	1126	1798
density (g/cc)	0.25	0.39	0.36	0.25	0.21	0.21	0.28
BWC [W/V] (g/100 ml)	**5.5**	**9.7**	**8.6**	**4.6**	**3.1**	**4.1**	**14.5**
butane activity [W/V] (g/100ml)	10.0	11.6	10.2	6.9	4.9	4.9	14.5
butane retentivity[W/V](g/100 ml)	4.5	1.9	1.6	2.3	1.8	0.8	0

* composite ground and packed to high density; ** current applied to composite to desorb butane, 4 A for 25 seconds, temperature increase ~ 50°C; ^^Wood-wood based commercial carbon

REFERENCES

1) T. D. BURCHELL, F. DERBYSHIRE, Y.Q. FEI AND M. JAGTOYEN, C. E. WEAVER, Proceedings of Eighth Cimtec World Ceramics Conference, 6/28, Florence, Italy (1994) 120.
2) M. JAGTOYEN, F. DERBYSHIRE, N, CUSTER, T. BURCHELL, 1994 Spring Meeting, Materials Research Society, San Francisco, April 4-8, 1994,Symposium Proceedings, 344, (1994) 77.
3) S. P NANDI and P. L. WALKER Jr. , FUEL, 1975, **54**, 169.
4) D. F. QUINN, J. A. HOLLAND, US Patent 5,071,820, 1991.
5) M. JAGTOYEN, F. DERBYSHIRE, G. KIMBER, Y. Q. FEI, Proceedings of the Tenth Annual Conference on Fossil Energy Materials, Fossil Energy AR&TD Materials Program, for USDOE,Oak Ridge National Laboratory, May 14-16(1996) 291.
6) GREGG, S.J., SING, K.S.W, in *"Adsorption, Surface Area and Porosity"*, 2nd ed., Academic, London , 1982, 94-100.
7) Y.Q. Fei and F. DERBYSHIRE, Proceedings, 22nd Bien. Conf. on Carbon,16-22 July,1995, 512.

ACKNOWLEDGEMENTS

The authors wish to acknowledge D. Turner and C. Lafferty of the CAER, the Commonwealth of KY and Rod Judkins of the ORNL for financial support of this work. This work is sponsored by the Fossil Energy AR&TD Materials Program, US Department of Energy, under contract no.SC19X-SN719C.

CARBON FIBER COMPOSITE MOLECULAR SIEVES

T. D. Burchell and M. R. Rogers

INTRODUCTION

Monolithic adsorbents based on isotropic pitch fibers have been developed jointly by ORNL and the University of Kentucky, Center for Applied Energy Research. Our monoliths are attractive for gas separation and storage applications because of their unique combination of physical properties and microporous structure. At ORNL we currently produce the monoliths in billets that are 10 cm in diameter and 25 cm in length. The monolithic adsorbent material is being considered for guard bed applications on a natural gas (NG) powered device. In order for the material to be successful in this application, we must attain a uniform activation to modest micropore volumes throughout the large monoliths currently being produced. Here we report the results of a study directed toward attaining uniform activation in these billets.

EXPERIMENTAL

The manufacturing process for our carbon fiber composite molecular sieve (CFCMS) materials has been reported elsewhere [1,2]. Activation was performed in a three-zone Lindburgh furnace fitted with an 20-cm diameter Inconel retort. The CFCMS samples were dried in vacuum at 300°C, heated to 850°C under He for one hour, cooled to 200°C for a chemisorption treatment in flowing O_2, and then heated again to 850°C in He. The chemisorption and activation steps were repeated until the desired total burn-off (weight loss) was attained. Micropore structure characterization was performed using a Quantichrome Autosorb-1 apparatus.

RESULTS AND DISCUSSION

A total of five billets were subjected to two cycles each of O_2 chemisorption/activation. The burn-off attained ranged from 8.5 to 13.4%, with an average burn-off of 10.4%. A typical (Type I) N_2 isotherm (77K) for sample SMW-8A is shown in Fig. 1. The Dubinin-Redushkevich (DR) micropore volume; Brunauer, Emmett, and Teller (BET) surface area; and Dubinin-Astakhov

(DA) micropore width for four SMW billets are reported in Table 1. The designations A and B indicate samples taken from opposite ends of the 25-cm long billets.

Table 1. Micropore volume, micropore size, and surface area data for CFCMS billets

Billet Number	BET Surface Area (m^2/g)	DR Micropore Volume (cm^3/g)	DA Micropore Diameter [mode] (nm)
SMW1-A	567	0.27	1.54
SMW1-B	425	0.16	1.64
SMW3-A	607	0.23	1.44
SMW3-B	448	0.17	1.48
SMW4-A	940	0.34	1.56
SMW4-B	488	0.19	1.54
SMW8-A	707	0.27	1.48
SMW8-B	441	0.16	1.54

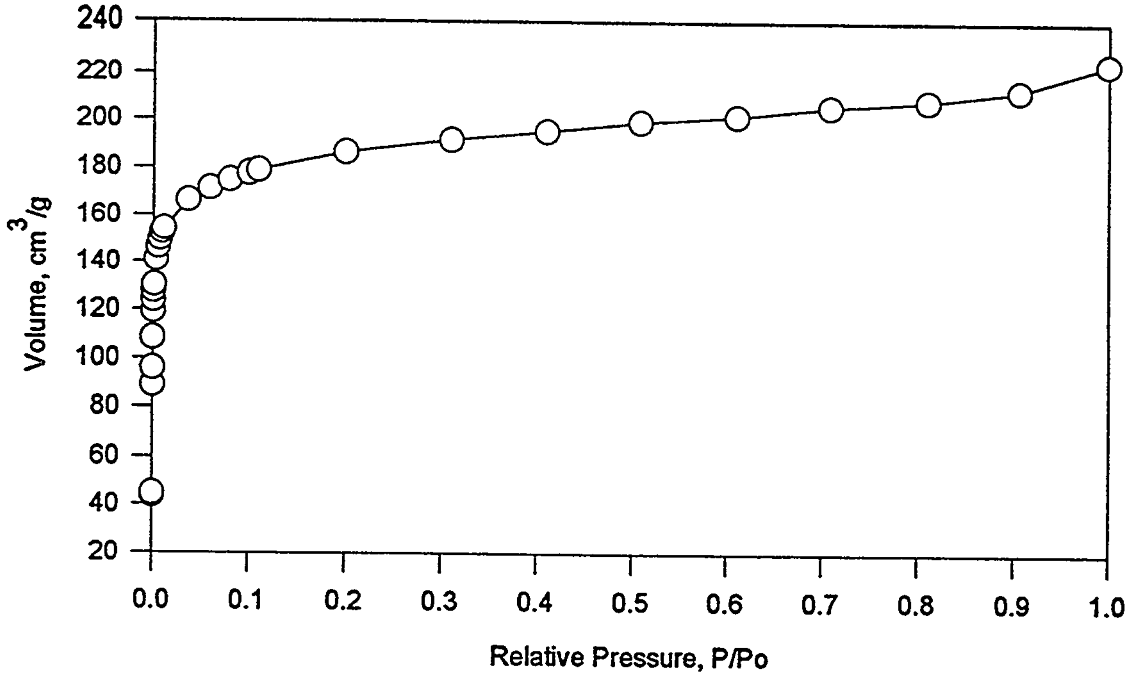

Figure 1. Typical 77K N_2 isotherm for sample SMW8A

The micropore volumes varied from 0.16 to 0.34 cm^3/g and the BET surface areas range from 425 to 940 m^2/g. Billet SM-15 was subjected to a more detailed examination to determine the uniformity of activation throughout the billet. Samples were taken at several radial locations across slices cut periodically along the billet length (Fig. 2). The BET surface area, DR micropore volume, and DA micropore size distribution were determined from the N_2 adsorption isotherm measured for each sample, and are shown in the 3D plots in Figs. 3-5. The BET surface area varied from 944 to 312 m^2/g and the DA pore diameter varied from 14 to 19.2 nm. Figure 6 shows the variation of DR micropore volume throughout billet SM-15, plotted as a function of diametral position for the five axial sampling positions. The DR volume varied from 0.12 to 0.35 cm^3/g, but there was no systematic radial or axial variation.

Figure 7 shows a breakthrough plot for an $Ar/H_2S/H_2$ mixture flowing through a sample of our CFCMS material. The H_2S was adsorbed, and breakthrough occurs some 18 minutes into the experiment. The H_2 and Ar were not adsorbed. Upon total breakthrough, the feed gas mixture flow was terminated and the desorption of the adsorbed H_2S was achieved by applying an electric current (4.5A @ 1V). Desorption occurred rapidly, as indicated by the increased concentration of H_2S in the exhaust gas stream. Regeneration of the CFCMS was thus achieved by direct electrical heating of the CFCMS. The ability of the material to readily adsorb H_2S suggests the removal of natural gas (NG) odorant additives might be achieved with a guard bed containing a billet of activated CFCMS. Consequently, a three-bed guard system was constructed and is depicted schematically in Fig. 8. The device contains three monolithic adsorbent pieces with approximate dimensions of 4.25-inches (10.8-cm) diameter and 10.0-inches (254-cm) length. Pressure drop data for He flow through an activated billet are shown in Fig.9. The measured pressure drop is slightly greater than for a packed bed of granular carbon. CFCMS is currently being evaluated as a guard-bed material for a NG fueled device.

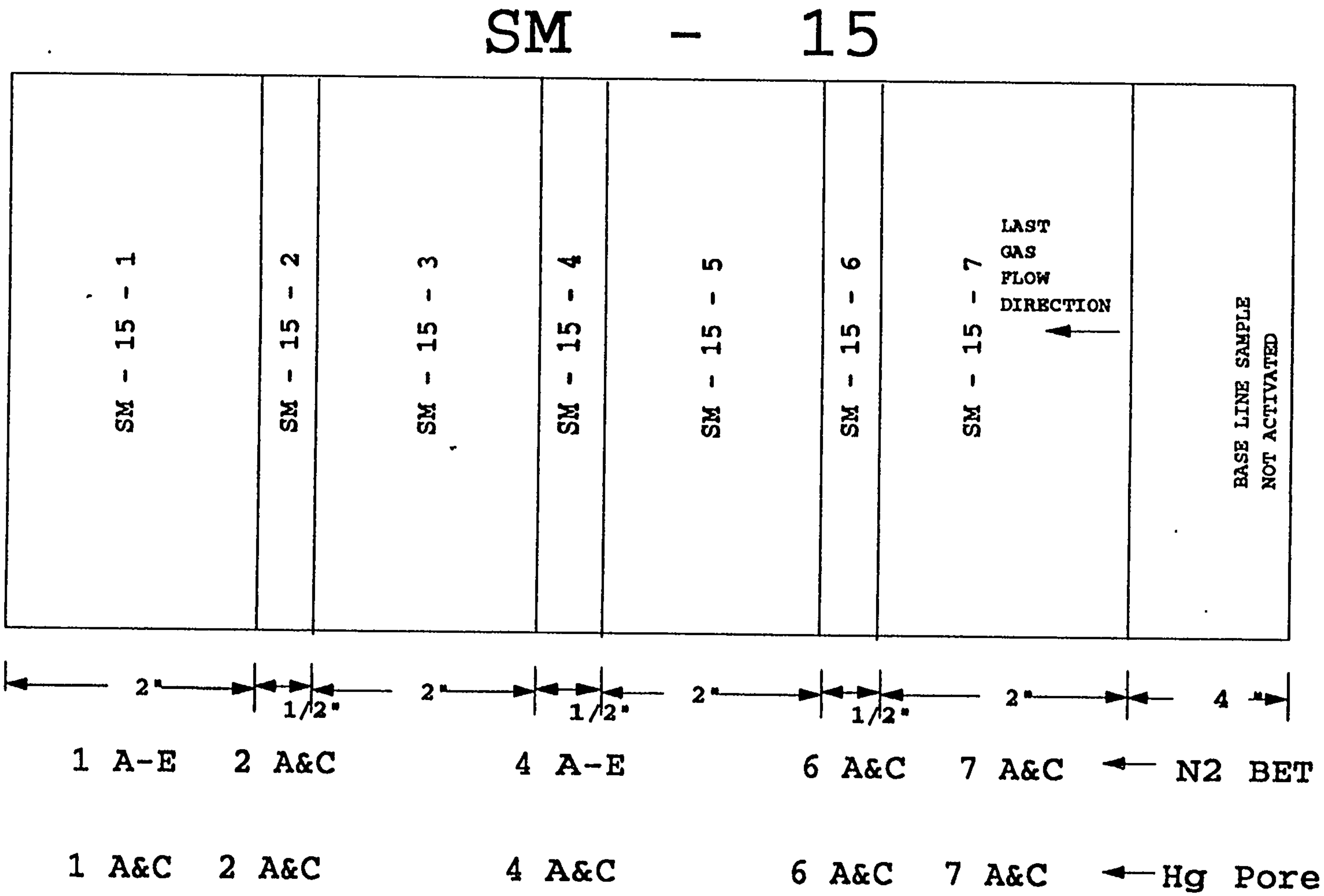

Figure 2. Sample locations in CFCMS billet SM-15

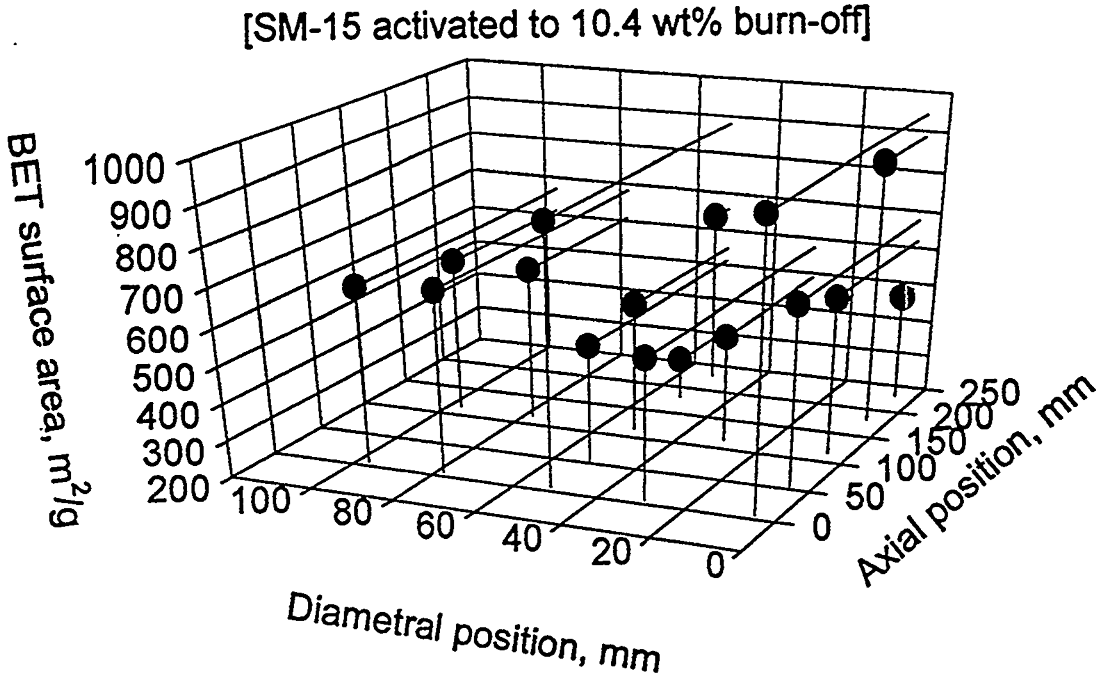

Figure 3. BET surface area as a function of position in billet SM-15

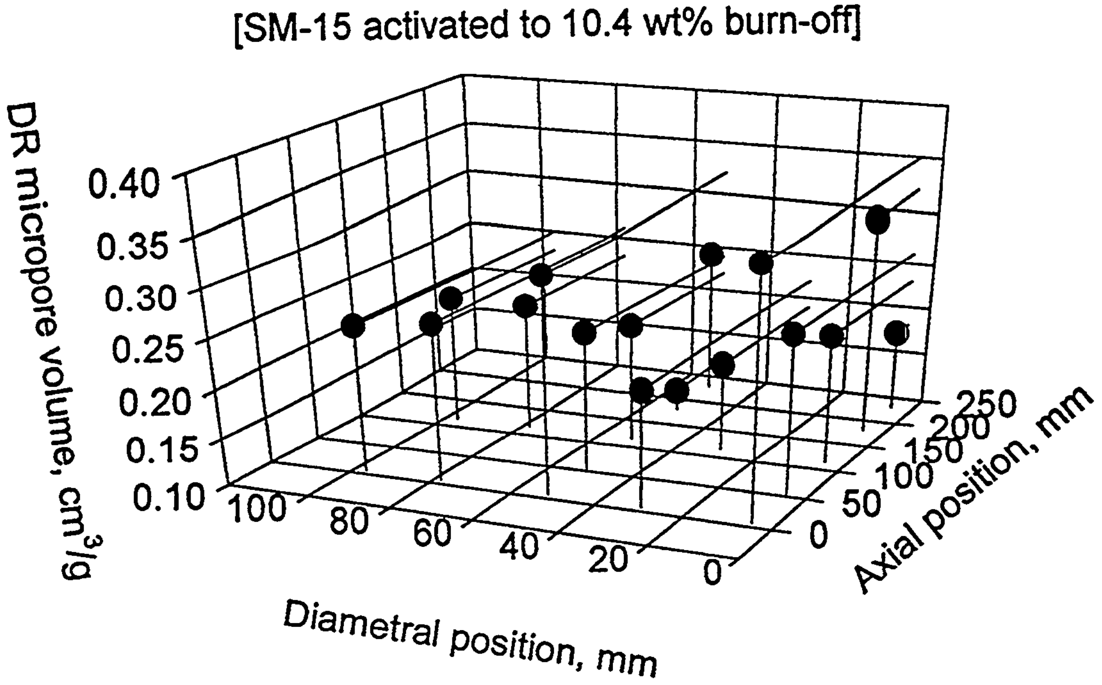

Figure 4. DR micropore volume as a function of position in billet SM-15

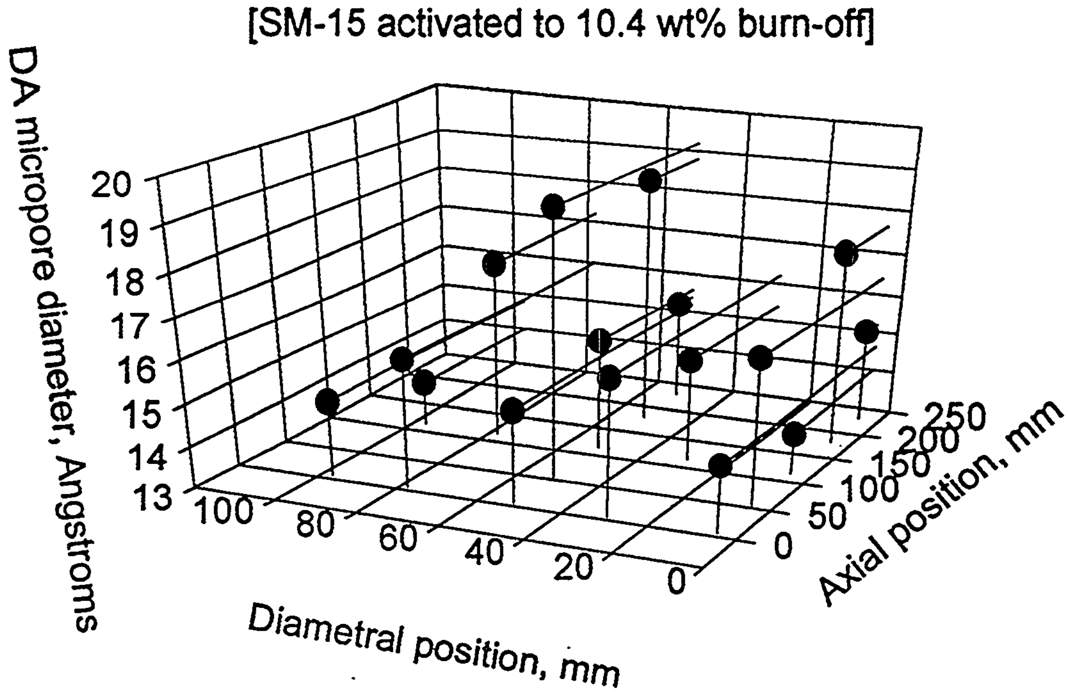

Figure 5. DA micropore diameter as a function of position in billet SM-15

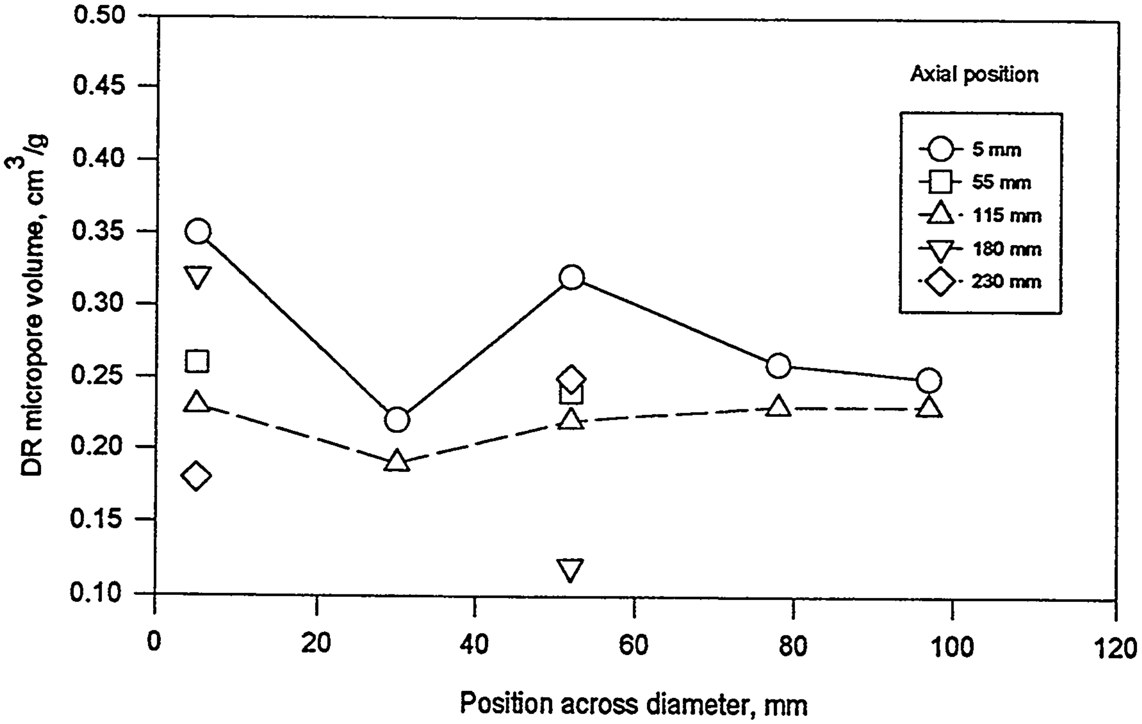

Figure 6. Variation of DR micropore volume in a CFCMS billet SM-15

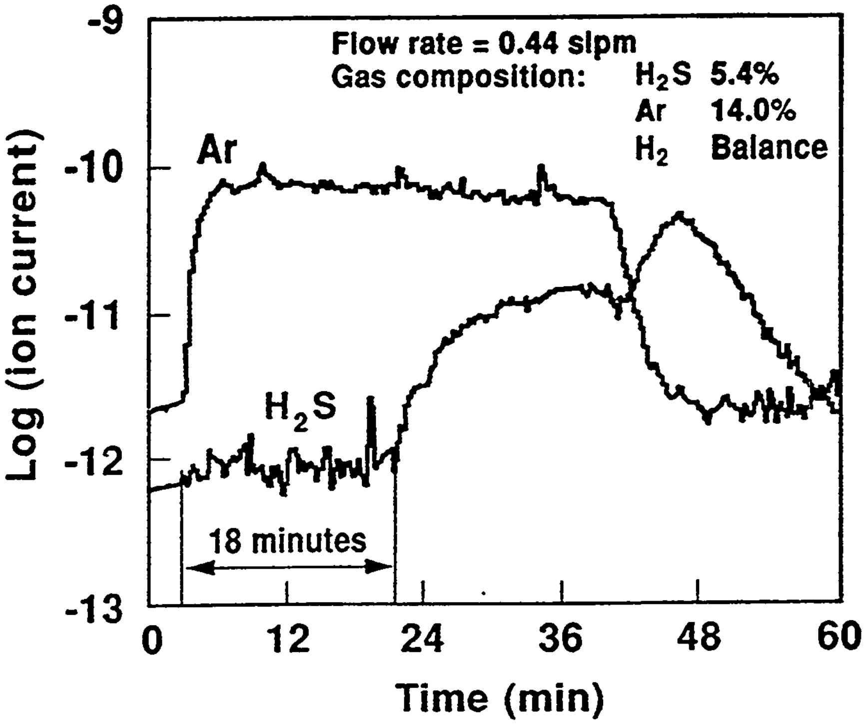

Figure 7. H_2S breakthrough plot for activated CFCMS showing the electrical desorption of the H_2S

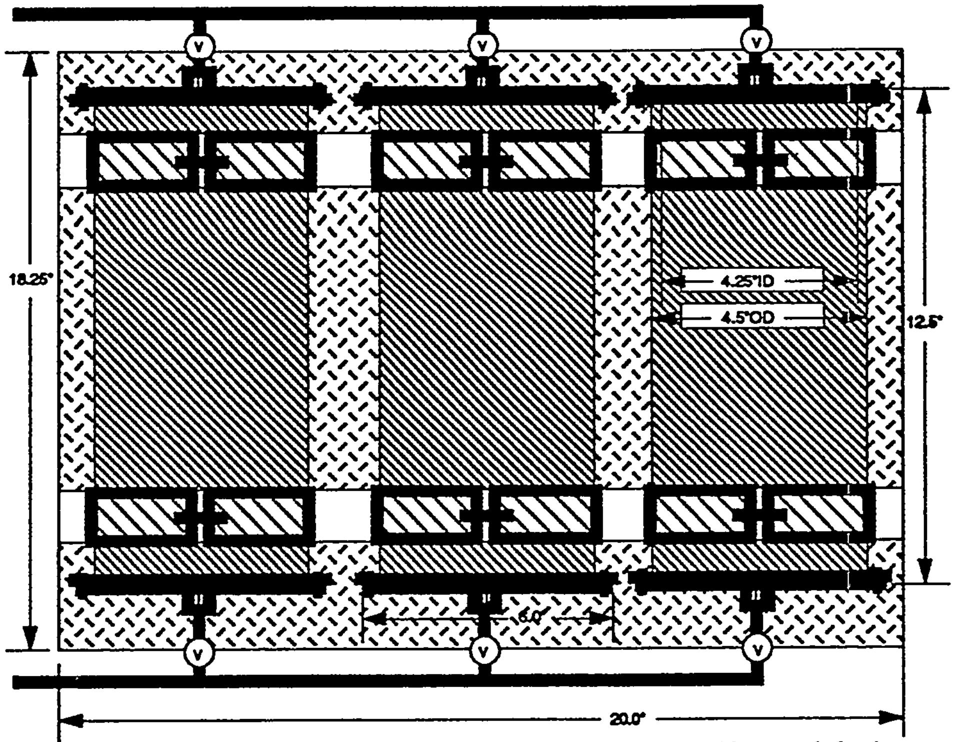

Figure 8. Schematic representation of our three-bed NG guard device containing CFCMS monoliths

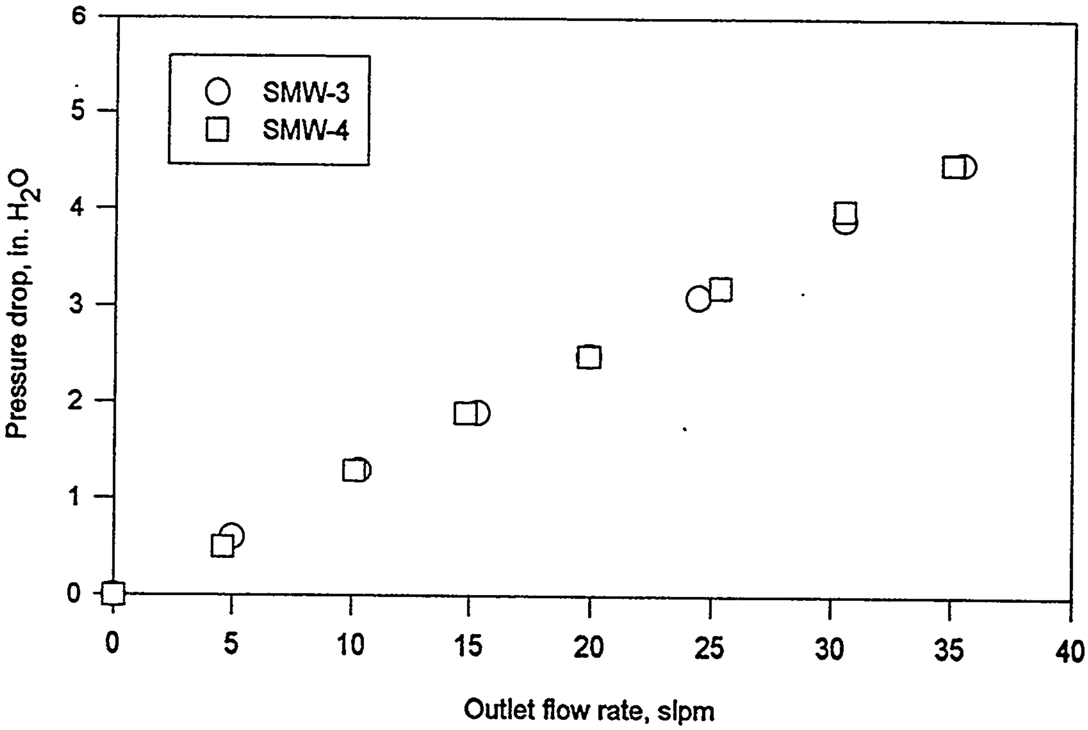

Figure 9. Pressure drop through a large monolith as a function of the He flow rate

CONCLUSIONS

Reasonably uniform activation was achieved in our CFCMS materials. Micropore volumes of 0.12 to 0.35 cm^3/g were attained. The ability of the materials to adsorb H_2S, the acceptable pressure drop, and its electrical heating capability suggests that CFCMS will make an ideal guard-bed material. Our three bed NG guard device is currently undergoing field trials.

REFERENCES

1. Burchell, T. D., Judkins, R. R., Rogers, M. R. and Williams A. M., *Carbon* 35 (1997) in press.
2. Burchell, T. D. in. *Proc. 8th Ann. Conf. on Fossil Energy Materials, CONF-9405143, ORNL/FMP-94/1*, pub. Oak Ridge National Laboratory, Aug. 1994, pp. 63-70.

SESSION II

CERAMICS, NEW ALLOYS, AND FUNCTIONAL MATERIALS

MECHANICAL PERFORMANCE OF HI-NICALON/CVI-SiC COMPOSITES WITH MULTILAYER SiC/C INTERFACES

H. G. Halverson, R. H. Carter, and W. A. Curtin

Department of Engineering Science and Mechanics
Virginia Polytechnic Institute and State University, Blacksburg, VA 24061

ABSTRACT

The mechanical properties and interfacial characteristics of new SiC/SiC ceramic composites, composed of Hi-Nicalon fibers in a CVI-SiC matrix and having a variety of multilayer SiC/C coatings between the fibers and the matrix, are studied in detail to elucidate the roles of the coatings and fibers. Axial tension tests and unload/reload hysteresis loop measurements are performed to determine mechanical performance. All materials exhibit the strong and tough behavior characteristic of good ceramic composites, with all multilayer variants performing quite similarly. SEM microscopy demonstrates that matrix cracks penetrate through the multilayers and debond at the fiber/inner-coating interface. Analysis of the hysteretic behavior leads to values for interfacial sliding resistance $\tau \approx 11$ ksi and interfacial toughness $\Gamma_i \approx 2$ J/m^2 that are nearly independent of multilayer structure, and are similar to values obtained for standard pyrolitic carbon interfaces. These results all indicate debonding at the fiber surface for all coating structures, which provides a common roughness, τ, and Γ_i. Analysis of fiber fracture mirrors provides an estimate of the in-situ strength of the fibers and demonstrates the high strength retention of the Hi-Nicalon fibers. The in-situ fiber strengths are combined with the measured pullout lengths to obtain an independent determination of $\tau = 8.5$ ksi that agrees well with the value found from the hysteretic behavior. Predictions of composite strength using the derived fiber strengths agree well with the measured value although the predicted failure strain is too large. This study demonstrates that Hi-Nicalon fiber/CVI-SiC composites perform well for a wide range of multilayer interface structures and that the interfaces present relatively high values of τ and Γ_i, both of which are beneficial to strength and toughness. The small carbon layer thicknesses in these multilayer coatings may allow for improved mechanical performance at elevated temperatures, in radiation environments, and possibly oxidizing environments.

INTRODUCTION

Here we report on a broad spectrum of experimental measurements and characterization performed on new Hi-Nicalon/CVI-SiC ceramic composites with multilayer SiC/C interfaces. These materials were fabricated and supplied by Hyper-Therm Inc.[1] The purposes of this effort are several. First, we want to obtain the basic macroscopic mechanical performance in these systems, and assess differences between different multilayer variants. Second, we want to carefully characterize the interface sliding and interface toughness in these systems, and again correlate properties with coating structure. Third, we want to perform optical and SEM microscopy to examine the crack path selection and crack density in these materials. Fourth, we want to assess the as-processed Hi-Nicalon fiber strengths and to determine if existing theories of composite strength, validated on a wide variety of other CMC systems, can successfully predict the observed strengths of these materials. In total, this effort assesses the efficacy of both multilayer coatings and Hi-Nicalon fibers in creating high-quality composite materials for various energy applications.

MECHANICAL PROPERTIES

The materials studied here consist of Hi-Nicalon fibers in a CVI-SiC matrix with a variety of SiC/C multilayer coatings. Both the individual SiC layer thicknesses and the number of such layers were varied. The layer thicknesses were characterized as "Thin", Medium" and "Thick", and the number of layers ranged from 2 to 8. Based on SEM, the thin SiC layers are approximately 0.06-0.10 μ in thickness, the medium layers are 0.10 -0.12 μ, and the thick layers are 0.15 μ. The carbon layers ranged from 0.01-0.03 μ. Two straight-sided samples of each type were supplied. Each sample was designated by the number of layers, the thickness, and the sample number (e.g. 2M-2 is the 2-layer, Medium thickness, 2nd sample).

The stress-strain curves for these materials are all quite similar, exhibiting an initial linear response, a subsequent non-linear response due to matrix cracking, and a final failure after extensive non-linear deformation (Figure 1). The elastic modulus, onset of non-linear behavior, strength, and failure strain are all larger than similar materials having CG-Nicalon fibers, which is attributable to the improved properties of the Hi-Nicalon fibers. Table I presents the benchmark values of the mechanical behavior for each of these materials. The elastic modulus is the same for all samples, as expected for well-controlled fiber volume fraction and matrix porosity, and is independent of interface type.

The onset of matrix cracking is determined using an 0.005% offset stress and the measured elastic modulus; the values range from 13-17 ksi, with no strong dependence on interface type although the 2M samples show slightly higher values than most. The hysteresis loop widths (not shown) are essentially zero for all speciments at and below 15 ksi, indicating no sliding behavior; this suggests that the longitudinal fiber tows are not cracked/debonded until stresses larger than 15 ksi. The ultimate tensile strengths, although most are grip failures, show very little difference among almost all specimens, except for the 2M material. The stronger 2M specimen actually survived 50 ksi and failed on reloading. There is a slight trend toward decreasing strength with increasing layer thickness (2M excepted), but the strengths for the 8K specimens could be low due to slight misalignment during sectioning. The failure strains are more variable, and the 2M samples exhibit quite high failures strains – values approaching those measured in CG-Nicalon/glass-matrix systems. The level of acoustic emission activity is superimposed on the stress-strain data in Figure 1 and shows a peak in number of events versus stress around 20-25 ksi, typical of all materials. The average number of acoustic events versus stress for all interface types (not shown) suggests that there is slightly more activity for 2 layer specimens and thin layer specimens, with the thick layer specimens generally having the lowest numbers of hits. Much of acoustic activity is at stresses larger than the regime of strong non-linearity in the stress-strain curves between 15-20 ksi, suggesting that initial transverse cracking occurs in the 90° tows below 15-20 ksi followed by further cracking in the 0° tows at higher loads. Acoustic emission declines substantially above 30-35 ksi. There were no identifiable correlations between features in the acoustic emission signal (amplitude, duration, energy, rise time) and stress.

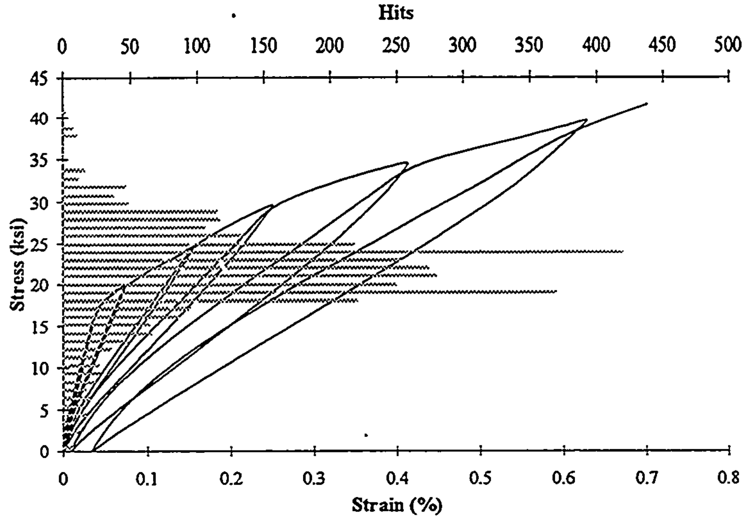

Figure 1: Sample Stress-Strain Curve

Table I: Mechanical Properties of Multi-layer SiC/SiC Materials

Specimen	Elastic Modulus (msi)	Tensile Strength (ksi)	Failure Strain (%)	0.05% Offset Stress (ksi)
2T	42.79	39.56	0.540	12.77
2M	42.10	45.90	0.741	16.88
2K	41.97	37.90	0.695	14.78
4T	45.22	37.94	0.428	15.15
4M	40.50	35.57	0.563	14.05
4K	42.46	33.80	0.614	14.50
8T	44.09	39.35	0.549	12.95
8M	40.38	36.70	0.655	15.42
8K	46.66	33.04	0.517	15.92

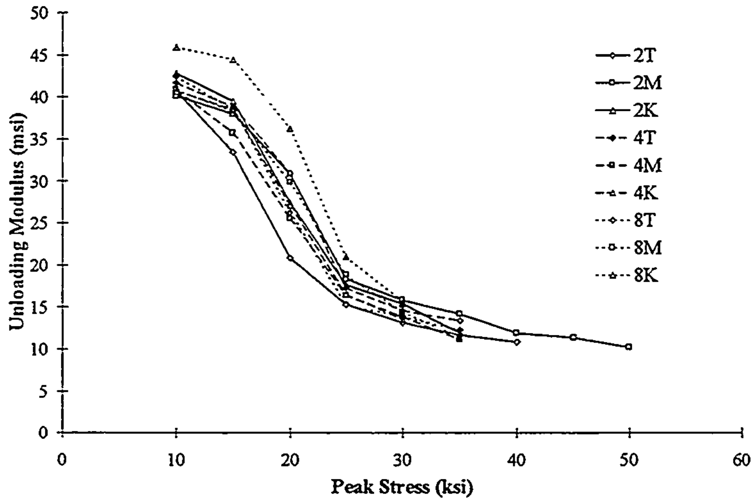

Figure 2: Unloading Modulus

The initial unloading modulus upon just unloading slightly versus the peak applied load is shown in Figure 2, and also indicates essentially no correlations among either different thickness or different numbers of layers. This shows that the crack densities are essentially identical in all materials.

MICROSCOPY OBSERVATIONS

We have performed both Optical and SEM microscopy to observe the crack behavior in these multilayer systems, and to attempt to correlate the physical cracking with the measured mechanical properties. The 2M samples were most carefully studied. Optical microscopy (not shown) under polarized light was generally successful for observing large scale cracking of matrix rich regions, transverse fiber tows, and the impingment of cracks into the 0° infiltrated fiber tows. All samples exhibited transverse cracking along the entire gauge section, with typical crack spacings d=250μm.

Of great importance to the stress-strain behavior, strength, and failure strain, is the cracking within the 0° fiber tows. It is this finer-scale cracking, rather than the larger-scale cracking in the 90° tows, that controls the major non-linear behavior of the composite and the hysteretic behavior, since frictional sliding occurs at the interfaces of the 0° fibers. To search for cracking in the 0° tow regions, we have performed SEM studies, although the microscopy is difficult because of the topography of the woven fiber surface even after careful polishing. Generally, we are unable to observe cracks that are entirely confined to the 0° tows; most of the cracks observed in the longitudinal tows are connected to the larger through-cracks. Occasionally, however, a fine crack is visible which is only 30 μm or so from another crack. The microscopy is thus, at present, inconclusive as to the presence of finer-scale cracks. We argue below that such cracks must exist, and are preparing samples to further investigate this cracking.

Figure 3 shows the efficacy of the multilayer fiber coatings. In the backscattered images, the thin carbon interlayers appear has faint dark lines and are visible near the surfaces of many fibers. *The*

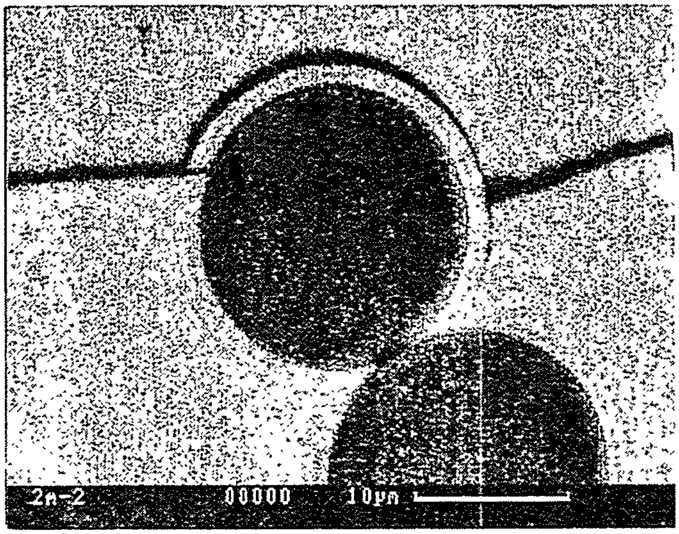

Figure 3: Oblique Crack Deflection

cracks impinging on the fibers in the 0° tows almost always penetrate through the coatings and terminate at the fiber/inner coating interface. We have not observed any cracks terminating at the outer layers. Cracks impinging on the transverse fibers exhibit varying behavior depending on the angle of impingement. Cracks approaching nearly perpendicular to an interface penetrates to the fiber surface and then debond. Cracks approaching more obliquely can debond at one or more of the multilayer interfaces. Thus, the C layers are "weak" layers which can act to deflect cracks but it appears that some component of opening, rather than shear, is required.

Although not all the different materials have been investigated in such detail, we have no evidence that the interfaces in any of the materials behave differently than discussed here. All cracks appear to penetrate the multilayer coatings when approaching at high angles. This conclusion is consistent with the measured mechanical responses showing that all materials have very similar overall deformation behavior and strength.

INTERFACIAL DEBONDING AND SLIDING

Here we analyze the measured hysteretic behavior in much more detail to elucidate differences in the interface-specific quantities: the interface frictional stress (τ) and the interface Mode II toughness (Γ_i). Debonding and sliding affect the stress-strain relation of a material, but in a standard quasi-static tensile test it is difficult to separate the various effects of the formation of new cracks, the extension of the fiber/matrix debond, and other damage events from one other. As a result, careful analysis of unloading/reloading hysteresis is used. During an unload/reload curve, no additional damage occurs in the material, and it is possible to directly relate the non-linearities in the stress-strain response to the interface properties. A typical hysteresis loop (Figure 4; inset), shows two regions, a quadratic region of increasing slip length, and a linear region where the slip zone extends over the entire debond region. Figure 4 shows the inverse of the hysteresis curve slope, the so-called Inverse Tangent Modulus (ITM), for the reloading curve for a series of peak stresses.

A method of determining Γ_i and τ from the ITM for unidirectional materials has recently been published[3]. For cross-ply materials with distinct matrix cracks in both the 90° and 0° plies, the analysis is not well-defined. Here, we will assume either (i) the only cracks are those observed in the microscopy or (ii) the existence fine-scale 0° fiber tow cracks not been observed in the microscopy. In both cases, the material can then be treated as effectively unidirectional; in case (ii) this is so only after the large through cracks have been formed, which occurs below/around 15 ksi. The constant slope region of the ITM (Figure 4) is related to τ and crack spacing d by the relationship

$$Slope = \frac{b_2(1-a_1 f)r}{2\tau d E_m f^2} \quad (1)$$

where b_2 and a_1 are known combinations of elastic properties of the fiber and matrix, f is the fiber volume fraction, r is the fiber radius, and E_m is the matrix elastic modulus.

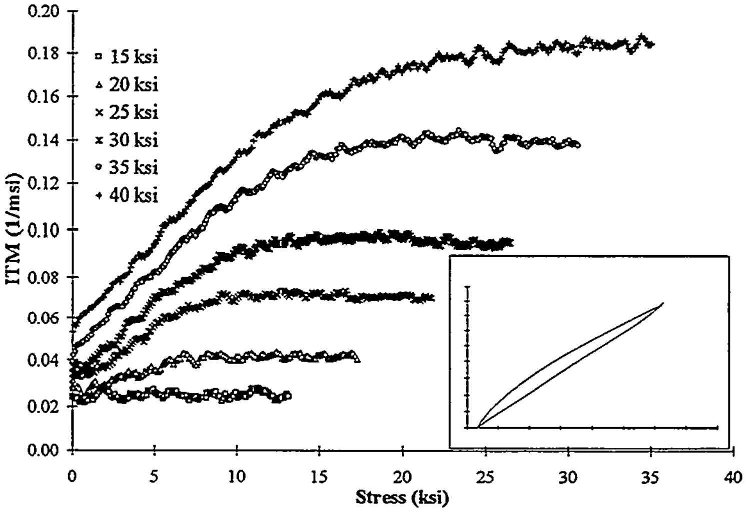

Figure 4: Inverse Tangent Modulus Plot

From our microscopy, it *appears* that the crack spacing is d≈250μ. Let us take the 250μm crack spacing to exist at 30 ksi, above which the acoustic emission (Figure 1) is decreasing rapidly and the unloading modulus (Figure 2) begins to saturate. Then, from the measured slope of the ITM at the 30 ksi peak load we can derive τ for each specimen. The typical values are around 1.2 ksi, which is very low. *In fact, we believe this analysis using the observed crack spacing must be incorrect and that this τ value is much too small.* Arguments and analysis supporting this claim are discussed below.

We now discuss an alternative method of determining the crack spacing indirectly from the mechanical test data. The mechanical data show that hysteresis does not exist at or below 15 ksi, and that significant acoustic emission ceases after 30 ksi. We thus believe that 0° tow cracking, which causes hysteresis, begins at around 15 ksi and has ended at 30 ksi. Now consider the very instant that unloading begins: the reverse slip zone has zero length and since no slip occurs the deformation must be completely elastic. Therefore, the initial unloading modulus E* is dependent <u>only</u> on the elastic properties of the material and the crack spacing, and the relationship is

$$\frac{E^*}{E_c} = \left(1 + \frac{D_1^0 r}{d}\right)^{-1} \quad (2)$$

where D_1^0 is a parameter found by a finite element solution[4]. For f≈32% in a 0° tow and the known elastic properties, $D_1^0=2.4$. Applying this to the woven structure, we assume that the modulus measured at 15 ksi reflects the modulus of the material with cracked 90° regions, and so is the "initial" value E_c to be used in Eq. (2). Then, we can use the measured initial unloading modulus (Figure 2) with Eq. (2), to derive the crack spacing d versus peak load. At 30 ksi, the crack spacing derived is 25-35 μm. A crack spacing of 30 μm was observed by Evans and coworkers on a CG-Nicalon/SiC material with a pyrolitic C interface. Our microscopy also shows the occasional crack spacing of about 30 μm in the 0 tows. Thus, our derivation of this final crack spacing is consistent with related results. In contrast, if one insists that the only cracks are those observed, with d=250 μm, then at the end of the test the unloading modulus would drop by only 7%. This is at odds with the measurements, suggesting the existence of many more cracks.

With the values of d determined above versus peak load, we now use the ITM data to derive τ. The results for τ are nearly constant versus peak load and the values obtained at 30 ksi peak stress are shown in Table II. The results for individual specimens vary from 8.7 ksi to 14.8 ksi with an average value of 11.8 ksi. We will further corroborate this value through independent measurements of fiber pullout as described in the next section.

The interface toughness, Γ_i, controls the extent of the debond and can be determined by the stress at which the transition from the frictional sliding region (constant slope of ITM) to elastic reloading region (constant ITM) occurs. This relationship is given by

$$\Gamma_i = \frac{r\sigma_p^2 c_1^2}{E_m}\left(1-\frac{\sigma_{tr}}{2\sigma_p}\right)^2 \tag{3}$$

where σ_p is the peak applied stress of the hysteresis loop, σ_{tr} is the transition stress, and c_1 is a combination of elastic constants. The values at peak stress 20 ksi are listed in Table II, with a typical value of 2.3 J/m^2 that is similar to that obtained in standard SiC/SiC.

Analysis of the hysteretic behavior of the multilayer materials thus leads to the following conclusions: (i) the crack spacing in the 0° fiber tows is ≈30μm at the end of the matrix cracking; (ii) τ≈11 ksi; and (iii) Γ_i≈2.3 J/m^2, for all materials studied here. These properties are comparable to values obtained in the standard pyrolitic carbon interface materials with CG-Nicalon fibers. Coupled with the microscopy, which shows debonding at the fiber/inner-coating interface, this result is not too surprising: the roughness and interface toughness are controlled by properties of the fiber/inner-coating interface in both thick Carbon and multilayer materials. Of some interest is the nearly complete insensitivity to the total carbon thickness in the multilayer materials. The thermal clamping stresses must depend quite sensitively on the carbon thickness, as is well established, so we conclude that in the present materials the clamping is mainly governed by roughness of the sliding interface, which would not be controlled by the carbon thickness. The insensitivity to total C thickness also suggests that the reduced radial compliance associated with increasing total carbon thickness is not an important factor in establishing the sliding resistance.

Table II: Interface Properties of Multi-layer SiC/SiC Materials

Specimen	Interface Frictional Stress (ksi)	Interface Toughness (J/m^2)
2T	8.67	2.58
2M	10.30	2.49
2K	11.74	2.24
4T	12.85	2.17
4M	11.64	2.42
4K	12.82	2.32
8T	11.29	2.65
8M	12.88	1.92
8K	12.66	2.23

FRACTURE MIRRORS, FIBER PULLOUT, PREDICTED STRENGTH, AND τ

The fracture surfaces of failed composites can provide a wealth of supplementary data useful for understanding the origins of the failure and the interfacial behavior. Specifically, fracture mirrors on the fracture surfaces of the pulled out fibers can be related to the as-processed fiber strength distribution (characteristic strength σ_C and Weibull modulus m) at the critical in-situ gauge length that controls the tensile strength and failure strain. The fiber pullout lengths are governed by a combination of the fiber strength (σ_C, m) and the interfacial sliding resistance τ by the relationship

$$\langle L\rangle = 0.25\,\lambda(m)\,r\sigma_C/\tau \qquad (4)$$

where λ is a known parameter around unity[2]. Therefore, measurements of both fracture mirrors and pullout lengths can be combined to quantitatively estimate τ. Moreover, the in-situ fiber strengths can be utilized to predict tensile strength as[2]

$$\sigma_{uts} = f\phi(m)\left(\frac{m}{2}\right)^{\frac{m}{m+1}}\left(1-e^{-2/m}\right)\sigma_c \qquad (5)$$

where ϕ is another known parameter.

Micrographs of the pullout from the 4T-2 specimen (gauge failure) and a typical fracture mirror are shown in

Figure 5a and b. The average pullout length is 93μm. The radius of a mirror is related to the fiber strength. Measuring a number of fracture mirrors allows for the creation of the statistical distribution of strengths {S} which are related to the desired quantities σ_C and m describing the true in-situ fiber strength

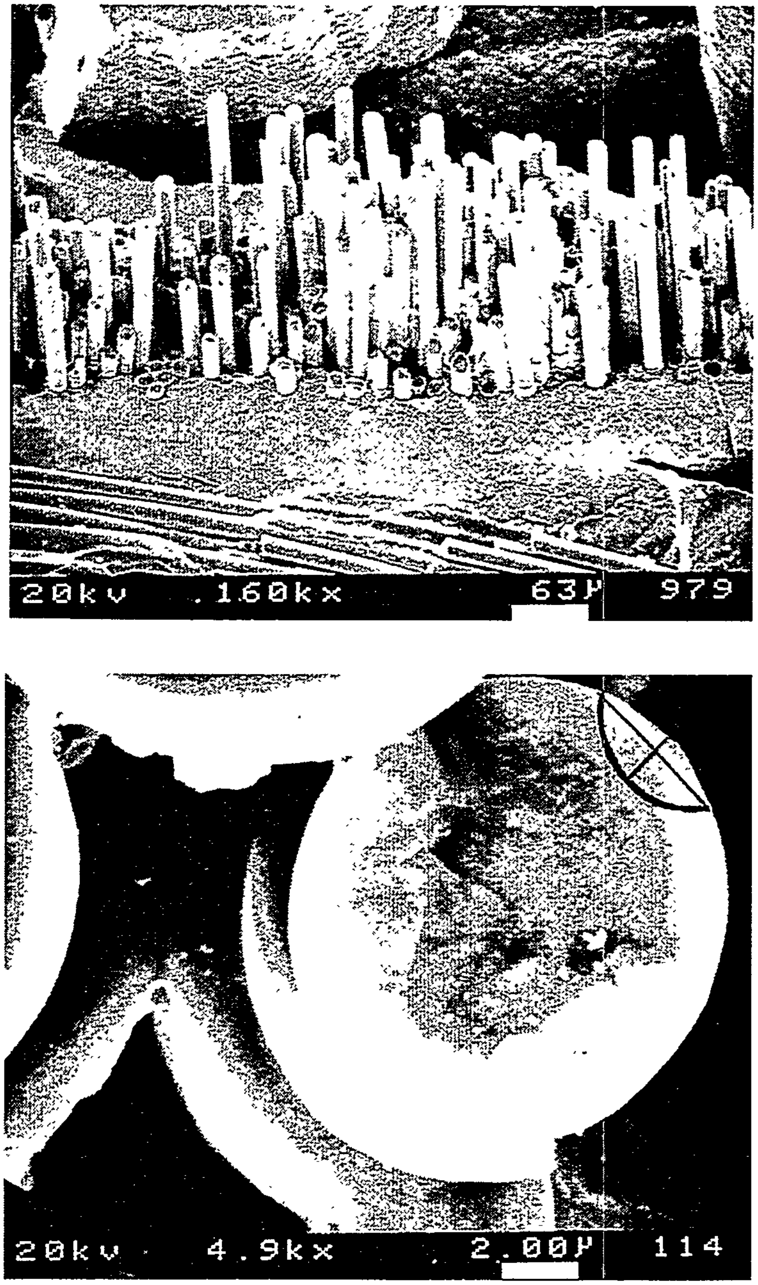

Figure 5a,b: Pullout and Fracture Mirror Photomicrographs

distribution. In measuring fracture mirrors for the 4T-2 specimen, only about 30% of the fibers exhibit measurable mirrors; 42% are too large and 38% are too small to assess reliably. This limits the accuracy of the determinations of the fiber strengths and, in particular, the Weibull modulus m of the fibers. Continuing nonetheless, we obtain σ_C= 388 ksi; m≈2. With the value λ=1.03 at m=2, we invert Eq. (4) to derive a value for τ of 8.1 ksi. This independent estimate is in reasonable agreement with the value of 12.5 ksi obtained from the hysteresis measurements. With the understanding that the fracture mirror data is not extremely accurate in this case, we nonetheless find that the two different methods for deriving τ are in the same range. In contrast, the estimate made using the observed 250μm crack spacing was only about 1.2 ksi – a factor of 10 difference; such a value of τ would lead to a predicted pullout of 625μm.

Using the derived values for σ_C and m, and f, the predicted composite strength is σ_{uts} = 39.2 ksi, which agrees well with the measured value of 36.7 ksi. The predicted failure strain is

$$\varepsilon_f = \left(\frac{\sigma_c}{E_f}\right)\left(\frac{2}{m}\right)^{\frac{1}{m+1}} = 0.89\%, \qquad (6)$$

which is larger than the measured value of 0.42%. Some of this deviation could be due to residual stress or flatness in the stress-strain. However, some materials exhibited much higher failure strains (see Table I), suggesting that such strains are indeed possible here.

SUMMARY

The main results of our experimental investigations on the current generation of Hyper-Therm multilayer SiC coated composites are as follows. We find that all of the materials examined show tough composite-like behavior, with large non-linearity and strain-to-failure. However, there are no significant differences among materials having different interface layer thicknesses or numbers of layers. Detailed analysis of the interfacial characteristics show all the materials to have similar interfacial sliding resistances. Microscopy on these materials shows that cracks penetrate the multilayers and tend to debond at the fiber/inner-coating interface. These observations are completely consistent with the common mechanical behavior observed. Analysis of the fracture mirrors and pullout on one specimen corroborates the interfacial sliding resistance measured using the hysteretic behavior, and indicates that the Hi-Nicalon fibers retain strength quite well after processing, in contrast to CG-Nicalon fibers. Performance of these and similar materials at elevated temperatures and under fatigue loadings will be the subject of future work. However, considerable opportunity exists for tailoring of the interface layer structure, carbon distribution, and layer roughnesses, to obtain even better materials.

Acknowledgements: Portions of this work were supported by the Department of Energy through a Phase II SBIR award to Hyper-Therm High Temperature Composites.

REFERENCES

1 Hyper-Therm, Inc., Huntington Beach, California

2 Curtin, W.A., "Theory of Mechanical Properties of Ceramic-Matrix Composites", *J. Amer. Ceram. Soc.*, Vol. 74, pp. 2837-2845, (1991).

3 Vagaggini, E., Domergue, J.-M., Evans, A.G., "Relationships between Hysteresis Measurements and the Constituent Properties of Ceramic Matrix Composites: I, Theory", *J. Amer. Ceram. Soc.*, Vol., 78, pp. 2709-2720, (1995).

4 He, M.Y., We, B.-X., Evans, A.G., Hutchinson, J.W., "Inelastic Strains due to Matrix Cracking in Unidirectional Fiber-Reinforced Composites", *Mech. Matl.*, Vol. 18, pp. 213-229, (1994).

HEAT TREATMENT EFFECTS FOR IMPROVED CREEP-RUPTURE RESISTANCE OF A Fe_3Al-BASED ALLOY

C. G. McKamey and P. J. Maziasz

Metals and Ceramics Division
Oak Ridge National Laboratory
Oak Ridge, TN 37831-6115

ABSTRACT

The iron-aluminide alloy FA-180, an Fe_3Al-based alloy with a composition of Fe-28Al-5Cr-0.5Nb-0.8Mo-0.025Zr-0.05C-0.005B (at.%), is of interest because of its improved creep-rupture resistance when compared to other Fe_3Al and FeAl-based alloys. Creep-rupture testing at 593°C and 207 MPa shows that FA-180 has a rupture life of about 100 h in the warm-rolled and stress relieved (1 h at 700-750°C) condition as compared to about 20 h for the FA-129 base alloy (Fe-28Al-5Cr-0.5Nb-0.2C). This report summarizes studies conducted in the last several years to determine the creep-rupture resistance of FA-180 as a function of the microstructures produced by varying the heat treatment temperature and cooling procedures. Solution-annealing for 1 h at 1150°C (air cooled) dramatically improved the creep-rupture life of FA-180 to about 2000 h. Transmission electron microscopy analysis showed that this strengthening was due to the precipitation of fine ZrC in the matrix and along grain boundaries. A further improvement in creep-rupture life to over 6000 h resulted from increasing the cooling rate (by quenching in oil or water) after solution annealing at 1150°C. The microstructure of the quenched specimen contained many fine dislocation loops instead of precipitates. During creep testing, these small loops evolved into a structure of larger dislocation loops and networks, resulting in significant strengthening at temperatures of 593-700°C.

INTRODUCTION

Past studies have shown that binary Fe_3Al possesses low creep-rupture strength compared to many other alloys, with creep-rupture lives of less than 5 h being reported for tests conducted at 593°C and 207 MPa.[1,2] The combination of poor creep resistance and low room-temperature tensile ductility due to a susceptibility to environmentally-induced dynamic hydrogen embrittlement[3-5] have limited use of these alloys for structural applications despite their generally excellent corrosion behavior.[6] With regard to the ductility problem, alloy development efforts have produced significant improvements, with ductilities of 10-20% and tensile yield strengths as high as 500 MPa being reported.[7,8] Initial improvements in creep resistance have been realized through small additions of B, C, Mo, Nb, and Zr.[1,9-13] Control of the amounts of these additions was also found to be important for producing improved weldability in these alloys.[12]

In recent years, further creep strengthening has been produced by using heat treatments to control the microstructure.[14,15] This paper summarizes work performed during the last three years to determine the effect of annealing temperature and the post-anneal cooling rate on creep-rupture properties and microstructural behavior.

EXPERIMENTAL PROCEDURES

The alloy composition used in this study was Fe-28Al-5Cr (at.%) with 0.5% Nb, 0.8% Mo, 0.025% Zr, 0.05% C, and 0.005% B (Oak Ridge National Laboratory designation FA-180). A 7-kg ingot was prepared by arc-melting and drop-casting into a chilled copper mold. Fabrication to an 0.8-mm-thick sheet was accomplished by hot-rolling, beginning at 1000°C and finishing at 600-650°C. After stress relieving for 1 h at 700°C, flat tensile specimens (0.8x3.18x12.7 mm) were mechanically punched from the rolled sheet. Before creep-rupture testing, specimens were annealed in air for 1 h at 1150°C and then were either air cooled to room temperature (slow cool) or were quenched in oil or water (faster cooling rate).

Creep-rupture tests were performed in air at temperatures from 593 and 750°C under stresses of 138 to 310 MPa (20-45 ksi). In order to obtain creep exponents and activation energies, minimum creep rates (MCR) were measured as the slope of the linear portion of the test curve and the data were plotted to a power-law equation. Tensile tests were also conducted at room temperature at a strain rate of 3.3 x 10^{-3}/s.

Scanning electron microscopy (SEM) using a Hitachi S-4100 (field emission gun) and optical metallography were used to study the microstructures and fracture modes. Analytical electron microscopy (AEM) using either a Philips CM30 (300 kV) or a CM12 [120 kV, with ultra-thin-window x-ray energy dispersive spectrometry (XEDS) detector] electron microscope was performed on samples cut from the gage portion of selected test specimens.

RESULTS AND DISCUSSION

As shown in Fig. 1, a 1-h heat treatment at 1150°C followed by air cooling to room temperature produced creep lives of over 2000 h for tests conducted at 593°C and 207 MPa. This is a significant improvement over the 100-h life observed for specimens of FA-180 heat treated at 750°C (signified by the horizontal line in Fig. 1). Especially interesting in Fig. 1 is the sharp dependence of creep strength on heat treating temperature. Transmission electron microscropy (TEM) of as-heat-treated specimens revealed the presence of a very fine $D0_3$ ordered structure within coarser B2 ordered domains (see Fig. 2). Also present in the matrix of specimens annealed at 1150°C was a fine dispersion of Zr-based precipitates (Fig. 2). These precipitates appeared to pin dislocations during creep, as shown in Fig. 3 for a specimen creep tested at 593°C.[14] This, together with an activation energy for creep of approximately 150 kcal/mole (a value which is about twice that obtained earlier[1] for the binary alloy heat treated at 750°C) and high creep exponents of 7-12 (ref. 15), indicated that the observed strengthening was being produced by a precipitation mechanism. The general conclusion was that the 1150°C heat treatment resulted in the dissolution of some of the coarse particles remaining from the melting and casting process. The finer Zr-based precipitates then formed during cooling or during the early stages of creep.

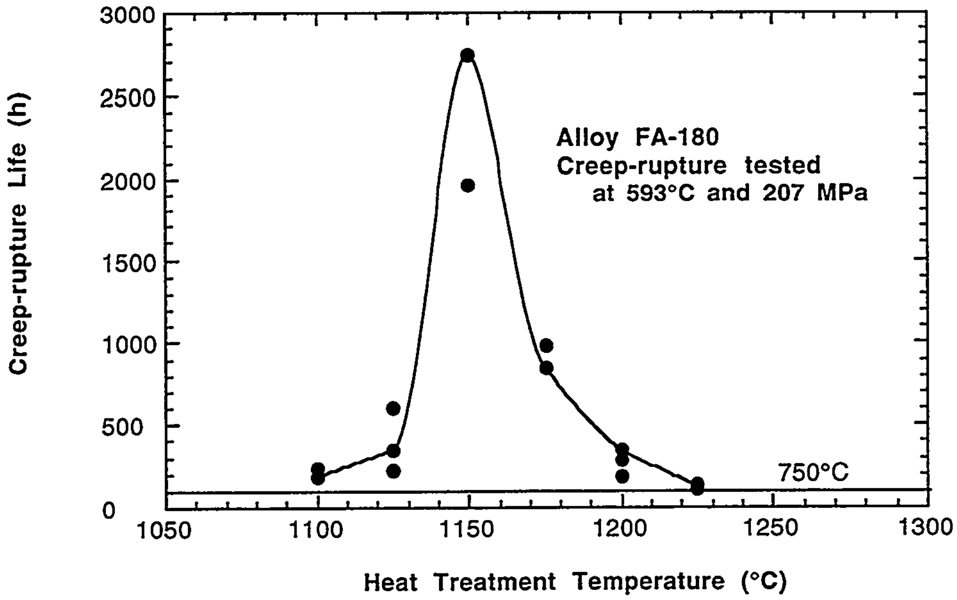

Fig. 1. Creep-rupture life as a function of heat treatment temperature for tests conducted on alloy FA-180 at 593°C and a stress of 207 MPa. The horizontal line at a life of 100 h represents the test of a FA-180 specimen heat treated for 1 h at 750°C.

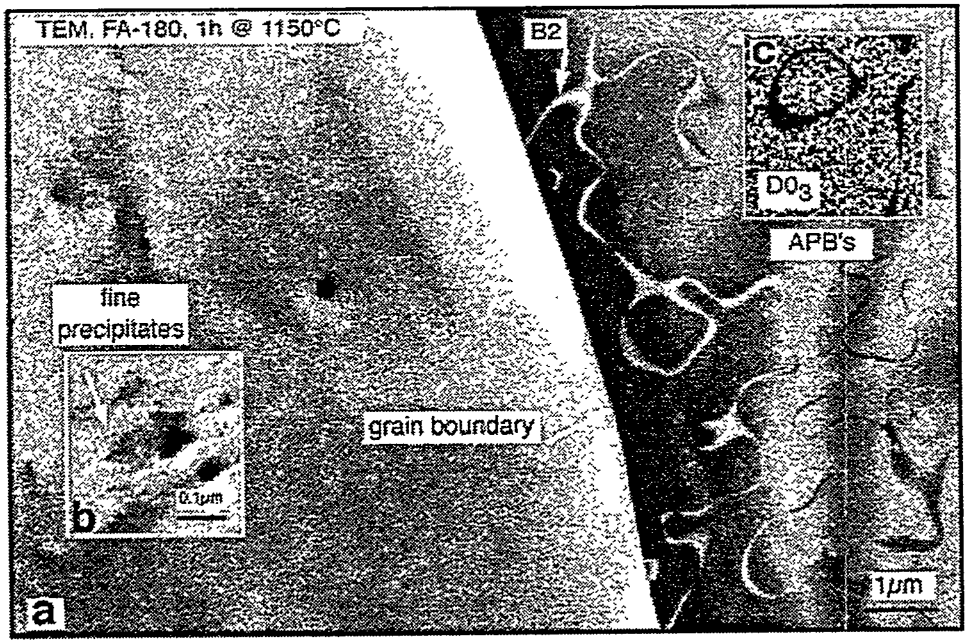

Fig. 2. Electron micrographs showing microstructural features of FA-180 as-heat-treated at 1150°C: (a) clean grain boundaries and low density of matrix dislocations, (b) fine matrix precipitates, and (c) the ordered structures produced by air cooling from 1150°C; fine $D0_3$ structure within coarse B2 structure.

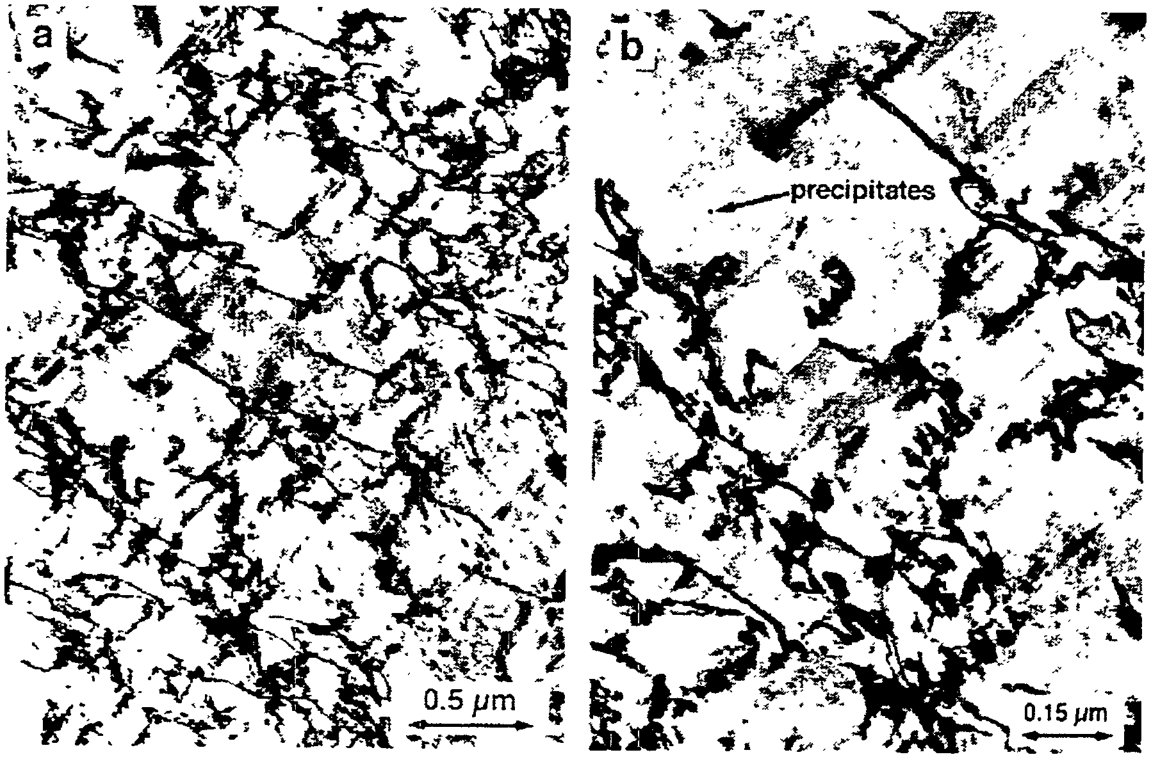

Fig. 3. Transmission electron micrographs showing (a) dislocation tangles and (b) fine matrix precipitates in alloy FA-180 air cooled from a heat treatment at 1150°C and creep tested at 593°C.

Creep-rupture tests were conducted on specimens cooled by different methods from the 1150°C heat treatment temperature and the data are presented in Table I. The more rapidly cooled specimens (oil or water quenched) exhibited the best resistance to creep. Even though the air-cooled specimen exhibited a very good rupture life of approximately 1959 h when tested at 593°C and 207 MPa, a specimen that had been quenched in oil showed no signs of rupturing (no increase in the very low, steady-state creep rate) after 6480 h, at which time the test was stopped. At more severe test conditions (650°C and 241 MPa), the ability of air-cooled specimens to resist creep was lost and failure occurred after an average of only 3 h, while an oil quenched specimen retained its resistance to rupture for over 240 h. Additionally, a water quenched specimen lasted 1637 h at 650°C and 241 MPa before rupture. In each case the fracture mode was observed to be ductile-dimpled rupture. This data suggest that there are fundamental differences in the strengthening mechanism for the quenched versus air cooled specimens.

The strengthening effect produced by quenching from 1150°C was also evident in room temperature tensile data (shown in Table II). The data in this table shows that quenching in oil resulted in hardening with an increase in yield strength from 255 to 481 MPa, even though the grain size was approximately 150 μm for both conditions. The hardening was also evident in the elongation to fracture. For all annealing conditions listed in Table II, the fracture mode was predominantly transgranular cleavage. These

Table I. Creep-Rupture Data for Alloy FA-180 as a Function of the Method Used for Cooling from the 1150°C Heat Treatment

Test Temp. (° C) Stress (MPa)	Air Cooled			Oil Quenched		
	Life (h)	Elong. (%)	MCR (/s)	Life (h)	Elong. (%)	MCR (/s)
593, 207	1959	10	8.3×10^{-7}	>6480[a]	>5	2.7×10^{-8}
650, 207	1059	11	5.5×10^{-7}	2180	14.4	8.3×10^{-8}
675, 207	2	32	1.8×10^{-3}	467	12	6.9×10^{-7}
700, 207	1	29	3.9×10^{-3}	104	11	5.5×10^{-6}
650, 241	3	42	2.2×10^{-3}	242	15	1.9×10^{-6}
650, 241				1637[b]	9[b]	2.2×10^{-7}
650, 241				86[c]	13[c]	2.6×10^{-6}

[a]Test stopped before rupture.
[b]Water-quenched from 1150° C.
[c]Oil quenched from 1150° C, then reannealed for 1 h at 750° C and air-cooled before creep testing.

Table II. Effect of Heat Treatment on Room Temperature Tensile Properties of Alloy FA-180

Heat treatment	Cooling medium	Yield strength (MPa)	Ultimate tensile strength (MPa)	Elongation (%)
1h/1150° C	air	255	347	2.7
1h/1150° C	oil	481	538	1.0
1h/1150° C+1h/750° C	oil/air	293	384	2.4

results are consistent with strengthening produced by quenched in defects, as has already been well established.[16-18] The reduced creep-rupture resistance and tensile yield strength of oil-quenched specimens that were reannealed at 750°C and air cooled (see data in Tables I and II) support this assumption.

Creep tests were conducted as a function of temperature (T) and stress (σ), and the data were fitted to a power-law creep equation of the form $\varepsilon = A\sigma^n(e^{-Q/RT})$ (ref. 19) in order to determine if the appparent activation energies for creep (Q) and the creep exponents (n) were the same in both the air-cooled and oil-quenched conditions (ε is the minimum creep rate, A is a constant, R is the gas constant). The results are shown in Figs. 4 and 5, respectively. At a stress of 207 MPa (30 ksi), the apparent Q for creep in the oil-quenched specimens was determined to be 84 kcal/mol, compared to a Q of 141 kcal/mol for air-cooled specimens. (The values of Q reported here are slightly different from those reported earlier[15,20] because more recent data have been included.) The large creep exponents shown in Fig. 5 for both the air-cooled and oil-quenched specimens are indicative of alloys which have been strengthened through some kind of dislocation-pinning mechanism,[21-24] although the much larger slope for the oil-quenched specimens suggests a difference compared to the air-cooled specimens. For the oil-quenched specimens, a distinct change was observed in the slope of the minimum creep rate versus stress curve in Fig. 5. The break occurred at approximately 200-250 MPa, with the creep exponent decreasing from nearly 20 at the higher stresses to less than 1 at the lower stresses. Data for the air-cooled specimens also suggest the possibility of a change in slope at stresses below 100 MPa. At this point in the research, the reason for this change in slope is unknown, but it could relate to a change in the creep mechanism with stress level.

In order to better determine the stability of the microstructures produced by quenching from 1150°C, creep tests of oil-quenched specimens were conducted as a function of temperature at a constant stress of 207 MPa (30 ksi), and the data are included in Table I. The data indicate that a more efficient and stable strengthening mechanism is operative in the oil-quenched specimens. The air-cooled specimens showed good creep strengths at temperatures as high as 650°C. Above this temperature, however, the specimens quickly became severely weakened, resulting in dramatically reduced creep lives and large elongations to failure at 675°C and above. The oil quenched specimens, on the other hand, exhibited excellent creep strength at temperatures up to and including 650°C and a creep life of over 100 h at 700°C. This data supports the idea that the dislocation pinning mechanism operating in the oil-quenched specimens is more stable than that in the air-cooled specimens, in that it provides strengthening to higher temperatures and loses its effectiveness more gradually as the temperature is increased. This could mean that either more

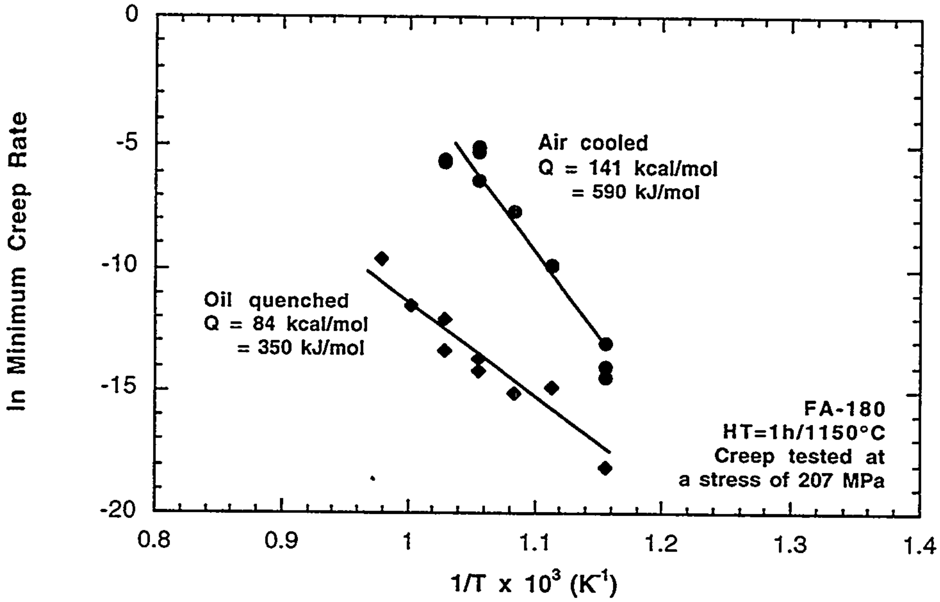

Fig. 4. Determination of creep activation energies for alloy FA-180 after either air cooling or oil quenching from a heat treatment at 1150°C.

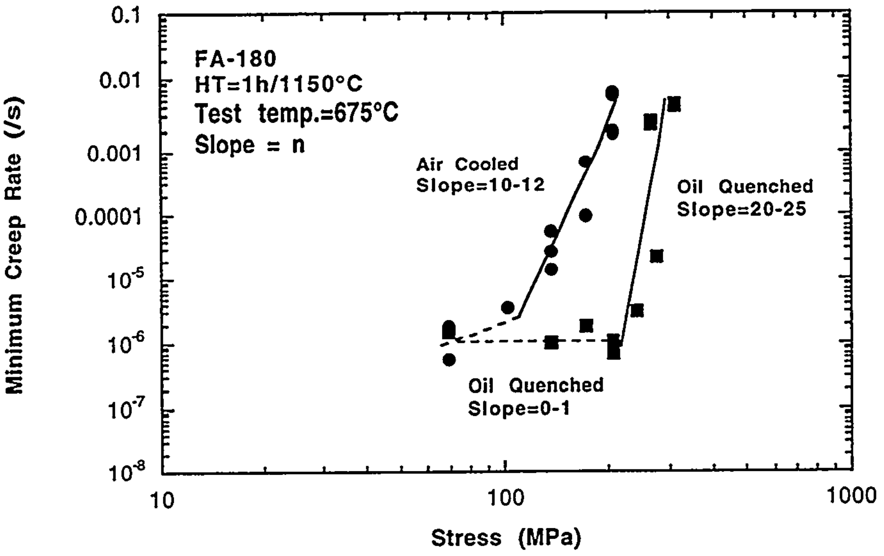

Fig. 5. Determination of creep exponents at a test temperature of 675°C for air cooled or oil quenched FA-180 heat treated at 1150°C.

and/or finer precipitates (identified previously as the strengthening mechanism in the air-cooled specimens[14]) are present in the oil-quenched specimens, or a more stable kind of pinning mechanism is active.

TEM examination of a control specimen oil quenched from 1150°C showed the presence of coarse B2 domains (Fig. 6) enclosing much smaller DO_3 domains, similar to the structure for the air cooled specimen shown in Fig. 2. In this as-heat-treated condition, the specimen also contained only a sparse distribution of dislocations. However, instead of a dispersion of precipitates, the oil-quenched specimen contained ultrafine (<10 nm) defects that were visible as black-white lobed images using g=011[B2] (see Fig. 6). These tiny defects exhibited a sharp line separating the black and white lobes that did not rotate with changes in g, consistent with the established contrast behavior of small edge loops.[25] Similar image analysis performed on the air-cooled specimen showed that those black-white strain contrast images did rotate with changes in g, consistent with their defect nature as 3-dimensional precipitates instead of 2-dimensional edge loops. Although loop nature (vacancy/interstitial) remains to be determined, many investigators observe higher vacancy concentrations in quenched FeAl type alloys,[16,17] and the likelihood of self-interstitial defects without irradiation is remote; therefore, it is reasonable to assume these are vacancy-type loops.

A TEM micrograph of the creep-induced microstructure in the gage of an oil-quenched specimen creep-tested at 593°C and 207 MPa for 6480 h without rupture is shown in Fig. 7. This microstructure clearly shows many large (>0.2 μm) loops uniformly dispersed throughout the matrix, accompanied by long pairs of 2-fold superdislocations. The growth of loops during creep from the "black dots" observed in

Fig. 6. TEM micrograph of alloy FA-180 showing B2 domains and fine dislocation loops (black dots) produced by oil-quenching from 1150°C (g=011 [B2], s=0).

the oil-quenched control specimen in Fig. 6 to the large loops observed in the creep-tested specimen is consistent with a vacancy nature. The loops observed in Fig. 7 have a basic square or rectangular shape, but with many kinks and jogs that would indicate intersections with network dislocations during creep. They appear to be distributed on orthogonal habit planes [either (110) or (100) types], and their contrast behavior (completely visible or invisible with g=011) is consistent with the behavior of edge loops.

The conclusion from TEM and the Q and n analyses is that vacancy loops, rather than fine precipitates, are the obstacles to dislocation motion in the oil-quenched material. The very low creep-rates and extended secondary creep regimes at 593°C and 650°C relative to the air-cooled material indicate that the vacancy loops are more effective barriers to dislocation climb despite their coarseness relative to the ultrafine precipitates observed in the air-cooled material. Their growth by vacancy absorption from the matrix and their direct interaction with intersecting network dislocations are likely factors making dislocation climb and glide through this loop structure more difficult than the ultrafine precipitate structure, consistent with the data in Table I. Although the general description of a mechanism which could produce creep-rupture strengthening through the pinning of dislocations on point defects would be similar for both precipitates and vacancies, fundamental differences (such as size of the defect, interfacial strength, coherency, stability as a function of temperature, etc.) could be responsible for the differences in Q and n shown in Figs. 4 and 5. The analysis of this data using a model for dispersion-strengthened materials[26] would probably be helpful in understanding the differences in the strengthening mechanisms involved.

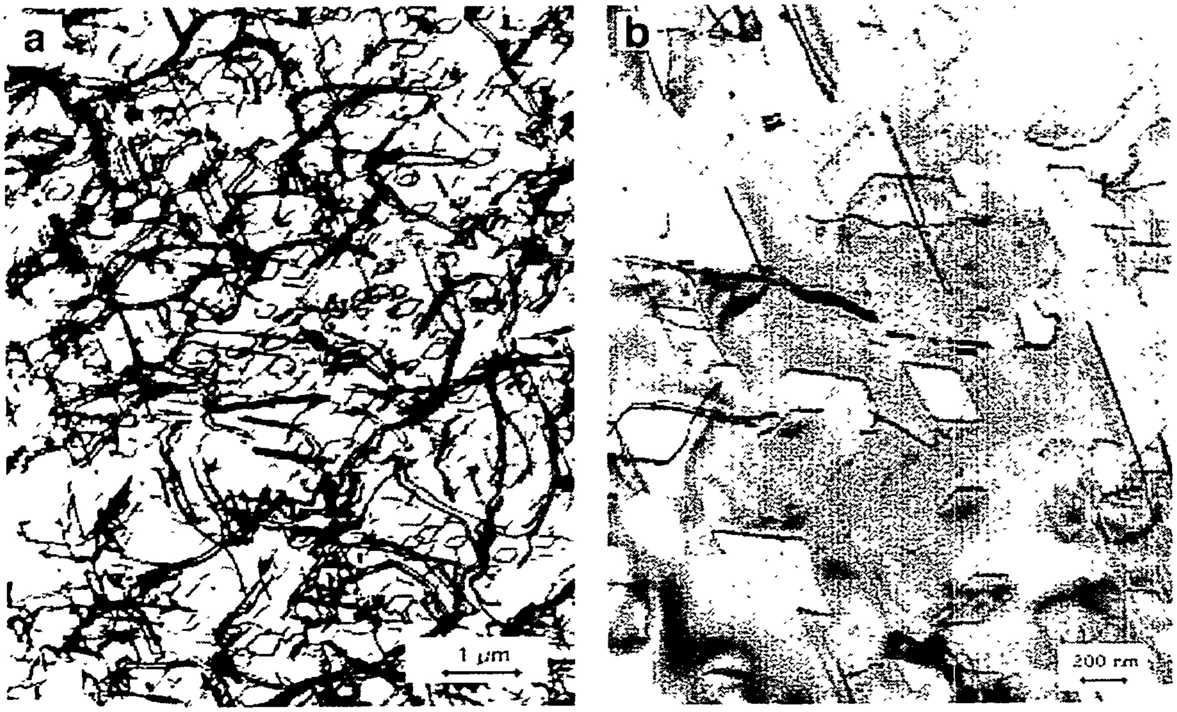

Fig. 7. TEM microstructure of a FA-180 (1150°C/oil quenched) specimen creep tested at 593°C/207 MPa for 6480 h without rupture (gage section), showing a) creep-induced dislocation network structure together with a dense dispersion of dislocation loops, and b) higher magnification showing several individual loops containing kinks and jogs, present on orthogonal habit planes (g=011[B2]).

CONCLUSIONS

The improved creep-rupture strength of an Fe_3Al-based alloy, FA-180 (Fe-28Al-5Cr-0.5Nb-0.8Mo-0.025Zr-0.05C-0.005B, at.%), was shown to be dependent on processing-induced microstructure. The creep-rupture resistance of this alloy was significantly improved by a solution-annealing heat treatment of 1 h at 1150°C. In specimens air-cooled from 1150°C, microstructural analysis revealed that strengthening was due to a fine dispersion of ZrC precipitates in the matrix and along grain boundaries. These precipi-tates were not observed in specimens annealed at higher or lower temperatures. Their presence was attributed to the dissolution of coarser ZrC particles (formed during the melting and casting process) during solution annealing, followed by reprecipitation during cooling or creep testing. Specimens solution-annealed at 1150°C and quenched to suppress the ZrC precipitation were found to be hardened by a dispersion of quenched-in loops that grew and evolved during creep testing at temperatures of 593-750°C and significantly delayed the onset of tertiary creep. Microstructural and creep activation/exponent analyses suggested that these were vacancy loops that acted as barriers to dislocation climb, resulting in the observed improvement in creep resistance.

ACKNOWLEDGEMENTS

This research was sponsored by the U.S. Department of Energy, Office of Fossil Energy, Advanced Research and Technology Development Materials Program, and by the Assistant Secretary for Energy Efficiency and Renewable Energy, Office for Industrial Technologies, Advanced Industrial Materials Program, under contract DE-AC05-96OR22464 with Lockheed Martin Energy Research Corp.

REFERENCES

1. C. G. McKamey, P. J. Maziasz, and J. W. Jones, *J. Mater. Res.*, **7(8)** (1992), 20892106.
2. C. G. McKamey, J. H. DeVan, P. F. Tortorelli, and V. K. Sikka, *J. Mater. Res.*, **6(8)** (1991), pp. 1779-1805.
3. C. T. Liu, C. G. McKamey, and E. H. Lee, *Scripta Metall. Mater.*, **24(2)** (1990), 385-90.
4. C. T. Liu and C. G. McKamey, in *High Temperature Aluminides and Intermetallics*, eds. S. H. Whang, C. T. Liu, D. P. Pope, and J. 0. Stiegler, (TMS, Warrendale, PA, 1990), pp. 133-151.
5. C. G. McKamey and C. T. Liu, in *Proceedings of ADVMAT/91, First International Symposium on Environmental Effects on Advanced Materials*, eds. R. D. Kane, (Houston, TX: NACE, 1992), paper no. 17-1.
6. P. F. Tortorelli and J. H. DeVan, in *Processing, Properties, and Applications of Iron Aluminides*, eds. J. H. Schneibel and M. A. Crimp (TMS, Warrendale, PA, 1994), pp. 257-70.
7. V. K. Sikka, *SAMPE Quart.*, **22(4)** (1991), 2-10.
8. V. K. Sikka, S. Viswanathan, and C. G. McKamey, *Structural Intermetallics*, eds. R. Darolia, J. J. Lewandowski, C. T. Liu, P. L. Martin, D. B. Miracle, and M. V. Nathal, (Warrendale, PA: The Metallurgical Society, 1993), 483-91.
9. P. J. Maziasz and C. G. McKamey, *Mater. Sci. & Eng.*, **A152** (1992), 322-34.
10. D. M. Dimiduk, M. G. Mendiratta, D. Banerjee, and H. A. Lipsitt, *Acta Metall.*, **36** (1988), 2947-58.
11. P. J. Maziasz, C. G. McKamey, and C. R. Hubbard, in *Alloy Phase Stability and Design*, eds. G. M. Stocks, D. P. Pope, and A. F. Giamei (MRS, Pittsburgh, PA, 1990), pp. 349-55.
12. C. G. McKamey, P. J. Maziasz, G. M. Goodwin, and T. Zacharia, *Mat. Sci. & Eng.*, **A174** (1994), 59-70.
13. D. G. Morris, M. Nazmy, and C. Noseda, *Scripta Metall. Mater.* **31**, 173 (1994).
14. C. G. McKamey and P. J. Maziasz, in *Processing, Properties, and Applications of Iron Aluminides*, eds. J. H. Schneibel and M. A. Crimp (TMS, Warrendale, PA, 1994), pp. 147-58.
15. C. G. McKamey, Y. Marrero-Santos, and P. J. Maziasz, in *High Temperature Ordered Intermetallic Alloys VI*, eds. J. A. Horton, I. Baker, S. Hanada, R. D. Noebe, and D. S. Schwartz (MRS, Pittsburgh, 1995), pp. 249-254.
16. P. Nagpal and I. Baker, *Metall. Trans.* **21A**, 2281 (1990).
17. A. Ball and R. E. Smallman, *Acta Metall.* **16**, 233 (1968).
18. D. J. Gaydosh and M. V. Nathal, *Scripta Metall. Mater.* 24, 1281 (1990).
19. O. D. Sherby and P. M. Burke, *Prog. Mat. Sci.* 13, 325 (1968).
20. C. G. McKamey and P. J. Maziasz, in *Proceedings of the Tenth Annual Conference on Fossil Energy Materials*, compiled by N. C. Cole and R. R. Judkins, ORNL/FMP-96/1, Aug. 1996, pp. 215-23.
21. O. D. Sherby and P. M. Burke, *Prog. Mater. Sci.* **13**, 325 (1968).
22. R. Lagneborg and B. Bergman, *Met. Sci. J.* **10**, 20 (1976).
23. K. Sadananda, H. Jones, C. R. Feng, and A. K. Vasudevan, in *High Temperature Ordered Intermetallic Alloys IV*, eds. L. A. Johnson, D. P. Pope, and J. O. Stiegler (MRS, Pittsburgh, 1991), pp. 1019-25.
24. I. Jung, M. Rudy, and G. Sauthoff, in *High Temperature Ordered Intermetallic Alloys II*, eds. N. S. Stoloff, C. C. Koch, C. T. Liu, and O. Izumi (MRS, Pittsburgh, 1987), pp. 263-74.
25. J.W. Edington, *Interpretation of Transmission Electron Micrographs*, Monograph 3 in Practical Electron Microscopy in Materials Science, N.V. Philips, Eindhoven, Netherlands, 1975.
26. J. Rösler and E. Arzt, *Acta Metal. Mater.* 38(4), 671 (1990).

THE EFFECTS OF COMPOSITION ON THE ENVIRONMENTAL EMBRITTLEMENT OF Fe_3Al Alloys

D. A. Alven and N. S. Stoloff

Rensselaer Polytechnic Institute
Troy, New York 12180-3590

Fe - 28 Al - 5Cr
↓

ABSTRACT

This paper reviews recent research on embrittlement of iron aluminides at room temperature brought about by exposure to moisture or hydrogen. The tensile and fatigue crack growth behavior of several Fe28-Al-5Cr alloys with small additions of Zr and C are described. It will be shown that fatigue crack growth behavior is dependent on composition, environment, humidity level, and frequency. Environments studied include vacuum, oxygen, hydrogen gas, and moist air. All cases of embrittlement are ultimately traceable to the interaction of hydrogen with the crack tip.

INTRODUCTION

This paper is concerned with the embrittlement of Fe28-Al-5Cr alloys containing various levels of Zr and C by moisture and by water vapor. The iron aluminides have been considered to be brittle when tested in air at room temperature, failing by transgranular cleavage or by intergranular cracking at elongations of 5% or less. However, when tested in dry environments, ductilities of up to 25% are observed [1 - 3]. It is generally agreed that moisture in air, in contact with aluminum-rich alloys, is broken down into hydrogen and oxygen; embrittlement actually results from the penetration of hydrogen into the lattice [1 - 4].

Several techniques have been devised to avoid embrittlement or to reduce its severity. These include use of dry oxygen or high vacuum environments. However, even when tested in air the ductility of the aluminides is markedly influenced by aluminum content, presence of solutes and control of the microstructure. Alloys with 28a%Al display the highest ductility in the Fe_3Al group, and Cr is the most effective solute to further increase ductility in the presence of moisture [2]. Other techniques to improve ductility include control of grain size and shape, changes in the type and decreases in the degree of long range order, and the addition of microalloying elements [4].

This paper will discuss the rate-limiting mechanism for fatigue crack growth behavior of several Fe-28Al-5Cr alloys containing Zr and C in moist air, oxygen, vacuum and hydrogen gas environments.

Under cyclic loading, crack growth rates have been shown to vary by orders of magnitude between wet and inert (dry) environments [3, 5 - 7]. The results of our crack growth experiments will be discussed in the context of dislocation-assisted transport of hydrogen to crack tips.

Experimental Alloys and Procedure

The alloys studied, all of which were supplied by Oak Ridge National Laboratory (ORNL), are listed in Table 1. Note that the Zr and C containing alloys are partially recrystallized; their processing was governed by recommendations from ORNL to maximize tensile ductility. All alloys were tested in the partial ordered B2 state. All tensile tests were run at a strain rate of $3x10^{-4} s^{-1}$ on cylindrical specimens with a 12.7mm long by 5.7mm diameter gauge length. Fatigue crack growth experiments were performed on all alloys in air, oxygen gas(1.3 atm), and hydrogen gas(1.3 atm), as well as in vacuum. All gases used in this study were of ultra high purity grade, with a maximum water vapor content of 3 ppm Fatigue crack growth tests were run at a frequency of 20Hz and an R ratio (σ_{min}/k_{max}) = 0.5, except where noted. Compact tension specimens were used for all fatigue tests which were 31.7mm x 30.5mm x 4.8mm thick.

TABLE 1. Composition of Iron Aluminide Alloys (Atomic %)

	Ternary	1%Zr-C	0.5%Zr-C	0.5%Zr
Fe	67.0	65.95	66.45	66.5
Al	28.0	28.0	28.0	28.0
Cr	5.0	5.0	5.0	5.0
Zr	-	1.0	0.5	0.5
C	-	0.05	0.05	-
g-size	180μm	*	*	*

*-partially recrystallized

Experimental Results

Effect of Composition

A summary of fatigue crack growth data in air for all alloys studied to date appears in Fig. 1. The fatigue crack growth data illustrate the effect of order and microstructure on the embrittlement of iron aluminides. The highest crack growth rate is found in the disordered, low aluminum content

FAP-Y alloy, while the lowest rate is found in the B2 ordered 0.5%Zr-C alloy. For Fe_3Al alloys the imperfect ordered B2 state has a lower crack growth rate than the highly ordered DO_3 state [3, 6].

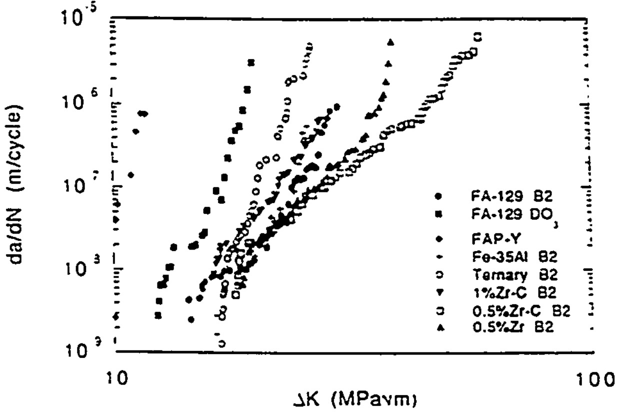

Fig. 1 Fatigue crack growth of iron aluminides in air at 25°C

The influence of environment on fatigue crack growth data for the Zr-containing alloys has been reported previously[5]. A summary of threshold stress intensities and critical stress intensities for the four alloys are shown in Fig. 2a) and b). Zr has its major effect in the high ΔK region (above the threshold region) and that 1 at% Zr is less effective than is 0.5 at% Zr. The presence or absence of carbon seems to have little influence, perhaps because of the high Zr/C ratios used in this work (see Table 1). No evidence of carbides or oxides were seen by TEM.

Fibrous tearing was predominant in all environments for the Zr-containing alloys except for 0.5%Zr and 1%Zr-C in hydrogen [5]. By contrast, FA-129 and the ternary alloy show predominantly cleavage in all environments [3, 6]. Dimpled rupture was only evident in FA-129 in the inert O_2 environment.

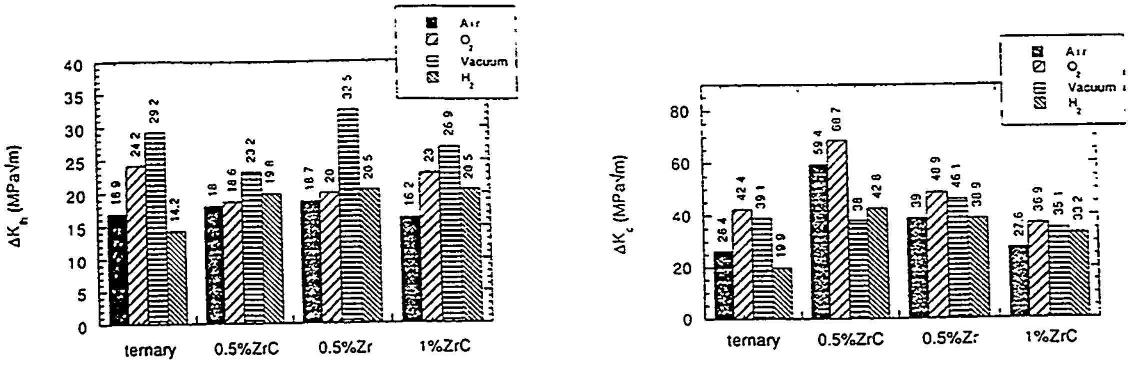

Fig. 2. (a) Threshold stress intensities in iron aluminides fatigued at 25°C. Frequency = 20Hz, R = 0.5.

(b) Critical stress intensities in iron aluminides fatigued at 25°C. Frequency = 20Hz, R = 0.5.

Effect of Humidity

The effect of increased humidity on the FCG resistance in 0.5%Zr-C is shown in Fig. 3. Similar data were obtained for the 0.5%Zr and 1%Zr-C alloys. The fatigue test conducted in oxygen is also shown in Fig. 3, as it is considered the inert reference environment.

An increase in humidity level had no effect on ΔK_{th} in 0.5%Zr-C. $\Delta K(10^{-7})$ was reduced 16% from 29.0 MPa√m in 21%rH air to 24.3 MPa√m in 81%rH. The embrittling effect of increased humidity was evident in 0.5% Zr-C, since ΔK_c was reduced from 59.4 MPa√m to 37.2 MPa√m.

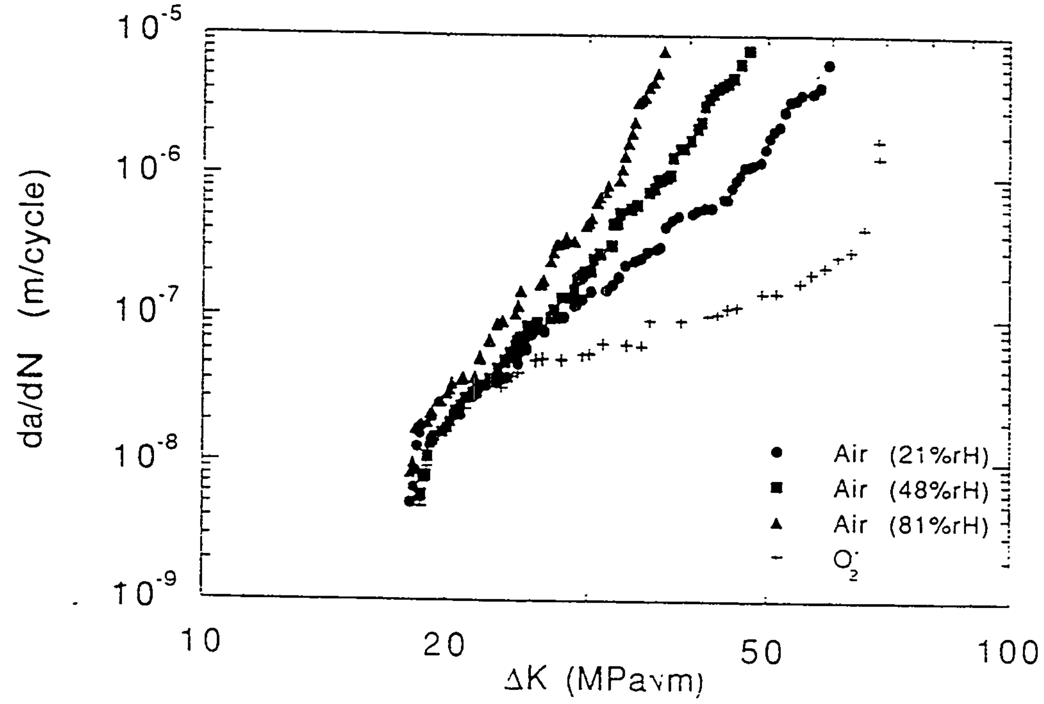

Fig. 3. Influence of humidity on fatigue crack growth of the 0.5%Zr-C alloy at 25°C.

Effect of Frequency

The effect of decreasing the test frequency for the 0.5%Zr-C alloy is shown in Fig. 4. All tests were run at a constant humidity level of 21%rH. Also shown is the fatigue test conducted in oxygen.

As can be seen in Fig. 4, the lower frequencies increased the rate of fatigue crack growth, and had a significant effect on both the threshold and critical stress intensities. The largest decrease in FCG resistance was seen between 20Hz and 2Hz, with the curves for 2Hz, 0.2Hz and 0.08Hz falling close together. While the FCG resistance and ΔK_c decreased as the frequency was lowered, ΔK_{th} increased, although the effect was small.

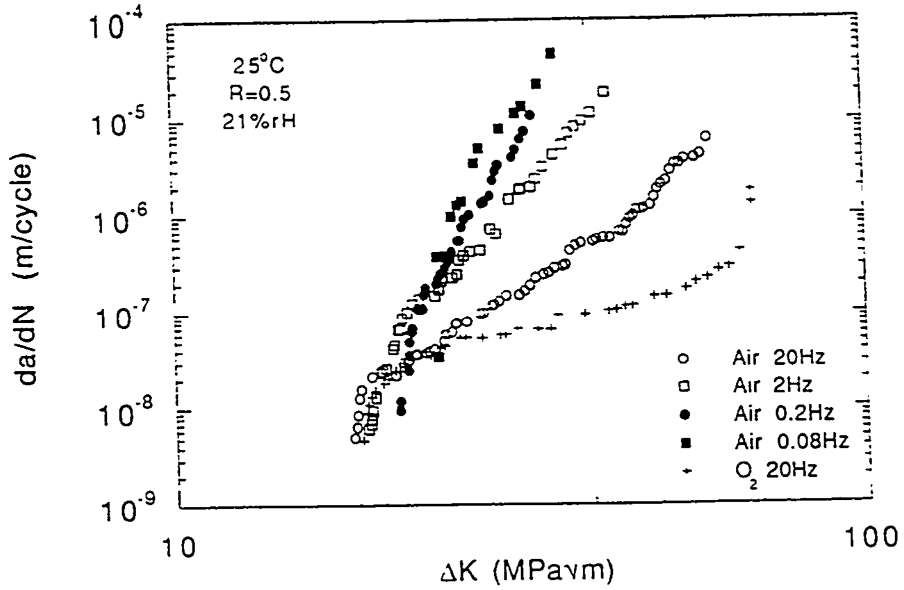

Fig. 4. Effect of frequency on 0.5%Zr-C fatigued in 21%rH air at 25°C. R = 0.5.

DISCUSSION

In terms of alloying, the addition of 0.5% Zr to Fe-28Al-5Cr results in an increase in tensile ductility and a decrease in the crack growth rate as compared with the other alloys. Carbon additions have been found to increase the critical stress intensity with little effect on the crack growth rate. There exists a limit to the beneficial effects of alloying with Zr, as the 1% Zr alloy has a higher crack growth rate than either of the 0.5% Zr alloys. Sikka [8] has previously shown that additions of 0.1 at% Zr + 0.01 at% C and 0.2 at% Zr +0.02 at% C give higher ductilities than 1 or 2 at% Zr. This suggests that the optimum Zr content for high ductility is between 0.1 and 0.5 at% Zr.

Fractographic evidence indicates two mechanisms by which the zirconium additions affect the crack growth rates in the Fe_3Al, Cr alloys. First, all the Zr-containing alloys exhibited a fibrous, transgranular surface when fatigued in oxygen (Fig. 5(b)). This is typical of ductile materials. Only the ternary alloy exhibited a characteristically brittle fracture surface in oxygen, which consisted of mixed transgranular and intergranular failure. The indications from the shift in fracture mode of the Zr-containing alloys when compared to the ternary alloy is that the addition of zirconium strengthens the grain boundaries. Previous research [9] has shown that the addition of B and Zr shifted the fracture path of several iron aluminides from intergranular to transgranular, but it was believed that the boron addition had caused the grain boundary strengthening. In this study, the addition of 0.5 at.% Zr resulted in a shift of fracture mode which indicates that zirconium also strengthens grain boundaries in Fe_3Al.

Second was the observation of some intergranular failure in 0.5%Zr and 1%Zr-C in hydrogen-containing environments. These results are interesting as most studies on iron aluminides have shown no effect on the fracture path in alloys of less than 35% Al. Previous work supports the view that a dislocation-transport mechanism in iron aluminides is responsible for embrittlement [6, 10]. Such a mechanism would allow for increased hydrogen contents at the grain boundaries where the dislocations pile-up. Trapping of the hydrogen by precipitates along the grain boundaries could lead to premature failure, when compared to the bulk, due to localized embrittlement. The appearance of the intergranular facets in 0.5%Zr and 1%Zr-C in hydrogen bearing environments, as compared to fibrous tearing fracture in an inert environment, indicates that excess hydrogen is being delivered to, or trapped, at the grain boundaries.

An increase in the amount of intergranular facets with increased Zr content was noticed. This may also be indicative of hydrogen trapping by zirconium-containing precipitates observed by TEM. Several studies [11, 12] have noted that increased precipitation of high binding energy and high saturability traps, with respect to hydrogen, decreases the resistance to hydrogen embrittlement.

A third explanation for the increased resistance to embrittlement might lie in effects of zirconium on the oxidation behavior of these alloys. The amount of reactive elements needed has been shown to be between 0.1 and 0.2 at%-, deterioration of scale adhesion was noted with additions of over 1 at%[13-15]. While it has not been shown that this same effect is operable at room temperature, it is possible that zirconium could influence the Al_2O_3 layer which, in turn, could influence the hydrogen-metal reactions.

Previous research has shown that dislocation-assisted diffusion is the rate limiting process in hydrogen embrittlement during fatigue crack growth of iron aluminides [10]. This phenomenon has been observed in a number of materials and is responsible for increased penetration depths of hydrogen over that caused by volume diffusion [16-19]. In this section, the model proposed by Castagna [10] will be applied to 0.5%Zr-C.

In dislocation-assisted diffusion, an atmosphere of hydrogen develops about a dislocation generated near the crack tip. As the dislocation travels away from the tip, the hydrogen is dragged with it through the lattice. The penetration depth of hydrogen ahead of the crack tip is equal to the dislocation velocity times the time available per cycle, that is V/2f where V is the dislocation velocity and f the test frequency. In the model proposed by Tien and Richards [18], the predicted maximum dislocation velocity that can be achieved before the hydrogen atmosphere is stripped away from the dislocation is used to determine the maximum penetration depth for dislocation assisted transport. Calculations based on this model for the 0.5%Zr-C alloy tested at frequencies ranging from 0.08Hz to 20Hz showed that the penetration depth increased by over 200 times, from 1.29×10^{-8}m to 3.24×10^{-6}m as the frequency decreased from 20Hz to 0.08Hz.

Castagna[10] proposed that the corrosion-fatigue expression for crack growth contains both a stress intensity and frequency dependence:

$$\left(\frac{da}{dN}\right)_{cf} = A\,\Delta K^{m} r^{n} \qquad \text{Eq. 1}$$

In Eq. 1, r is the penetration depth of hydrogen ahead of the crack tip, and A is a constant. Eq. 1 indicates that there is no embrittlement if either the applied stress intensity is zero or the internal hydrogen concentration is zero and the frequency effect is reflected in the penetration depth term as the depth will increase over one cycle as the frequency decreases. If it is assumed that the mechanical component of Eq. 1 is independent of frequency and that the stress corrosion component is zero, the total crack growth rate in an embrittling environment, (da/dN), can then be expressed as a superposition of the response in the inert environment, $(da/dN)_i$, and the corrosion fatigue term as:

$$\left(\frac{da}{dN}\right) = \left(\frac{da}{dN}\right)_{i} + \left(\frac{da}{dN}\right)_{cf} \qquad \text{Eq. 2}$$

In order to verify the validity of Eq. 1, it can be rearranged as:

$$\mathrm{Log}\left(\frac{da}{dN}\right)_{cf} = \mathrm{Log}(A) + m\mathrm{Log}(\Delta K) + n\mathrm{Log}(r) \qquad \text{Eq. 3}$$

and a plot of $\mathrm{Log}(da/dN)_{cf}$ vs. $\mathrm{Log}(r_{max})$ at constant ΔK should yield a straight line with a slope of n and an intercept of Log(A) + mLog(ΔK). In order to create this plot, the corrosion-fatigue term must be determined from Eq. 3. This is done assuming that $(da/dN)_i$ can be taken as the response in the inert oxygen environment. The crack growth data for 0.5%Zr-C in air have been broken down into the purely mechanical component and the corrosion-fatigue component, $(da/dN)_{cf}$ at the frequencies of 20 to 0.08 Hz. The plots of Eq. 3 are shown in Fig. 7 for ΔK = 27, 29, and 31 MPa√m.

As can be seen in Fig. 5, the correlation is excellent, and from the least squares fit the exponent n in Eq. 1 is 0.74. To find the values of A and m in Eq. 1, the latter is rearranged into:

$$\mathrm{Log}\left[\frac{\left(\frac{da}{dN}\right)_{cf}}{r_{max}^{0.74}}\right] = \mathrm{Log}(A) + m\mathrm{Log}(\Delta K) \qquad \text{Eq. 4}$$

Plotting Eq. 4 for all values of ΔK and frequencies yields a single frequency-modified curve and from a least squares fit the values of A and m are $4.9\mathrm{x}10^{-19}$ and 11.7, respectively.

As a final check, a plot of $(da/dN)_{cf}$ vs. $(r_{max})^{0.74}$ should result in a straight line for each applied stress intensity. Once again the correlation was excellent and showed that in fatigued 0.5%Zr-C hydrogen moves into the lattice ahead of the crack tip by a dislocation-assisted transport mechanism.

It should be noted that even though the degree of embrittlement increased dramatically with decreased frequency the exponent, n, was unchanged. This indicates that the embrittlement does little to change the mobility, ease of generation , or hydrogen-carrying capacity of the dislocations in 0.5%Zr-C. Due to this observation, any hydrogen-metal interaction which involves a change in dislocation mobility, such as hydrogen enhanced plasticity or inhibited dislocation motion in the presence of hydrogen, can be ruled out.

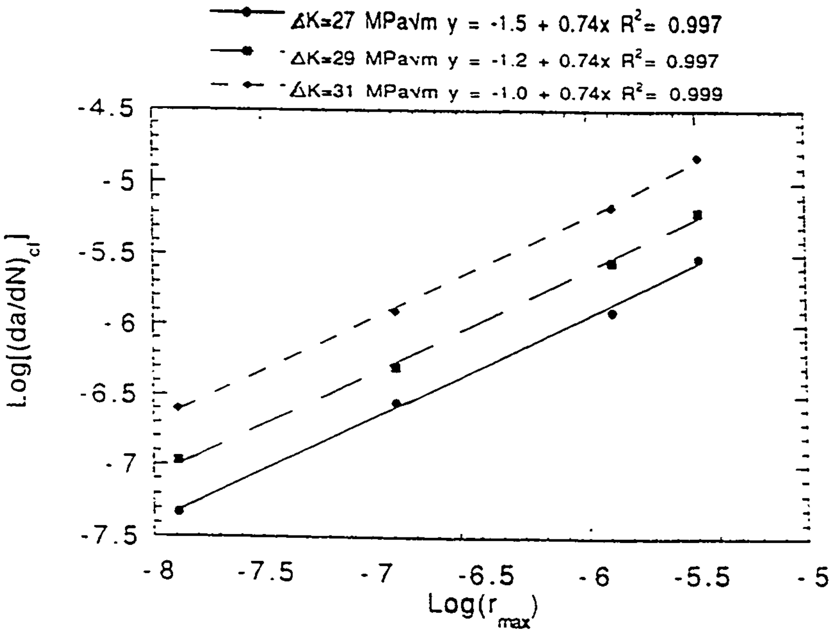

Fig. 5 Log-log plot of $(da/dN)_{cf}$ vs. maximum hydrogen penetration depth due to dislocation transport in 0.5%Zr-C fatigued in 21%rH air.

TABLE 2. Comparison of Constants in Eq.4 for 0.5%Zr-C and FA-129

Values	0.5%Zr-C	FA-129
n	0.74	0.52
m	11.7	10.3
A	4.9×10^{-19}	3.8×10^{-18}

The physical meaning of the exponent, n, in Eq. 1 has been described as either related to the quantity of hydrogen dislocations can carry into the plastic zone and the concentration of hydrogen required to enhance crack growth, or related to the distribution of penetration depths of the hydrogen-bearing dislocations [10]. Table 2 lists the calculated constants found for the two alloys analyzed. 0.5%Zr-C is found to have higher exponents and a lower pre-exponential constant than FA-129. As shown in Fig. 1, 0.5%Zr-C also displays a higher fatigue crack growth resistance than does FA-129.

SUMMARY

The susceptibility to moisture-induced hydrogen embrittlement in Fe_3Al,Cr alloys is reduced by the addition of zirconium. The beneficial effects of zirconium on the ductility and fatigue crack growth resistance of Fe_3Al,Cr alloys are limited to below 1 at.%. Zr. Fatigue crack growth resistance was seen to decrease with increased humidity level in air. The possible mechanisms for increased resistance to moisture-induced hydrogen embrittlement due to the addition of zirconium are; a) increased grain boundary strength, b) trapping of hydrogen by zirconium rich precipitates, and c) effects on the oxidation behavior. The zirconium to carbon ratio greatly influences the ductility, as proposed by Sikka [8] , and fatigue crack growth behavior in iron aluminides. Dislocation-assisted transport is responsible for the motion of hydrogen atoms released from water vapor through the lattice of 0.5%Zr-C, and this process is the rate limiting step in the hydrogen embrittlement that occurs during fatigue crack growth. 0.5%Zr-C exhibits the highest fatigue crack growth resistance in both inert and embrittling environments compared to the ternary alloy, 0.5%Zr, 1%Zr-C and to all other Fe_3Al alloys previously tested in this laboratory.

Acknowledgment

Research supported by the US Department of Energy, Fossil Energy Program, under Martin Marietta Energy Subcontract No. 19X-SF521C

REFERENCES

1. C. T. Liu, E. H. Lee and C. G. McKamey, Scr. Metall., vol. 23, pp. 875-880 (1989).

2. C. G. McKamey, J. A. Horton and C. T. Liu, J. Mater. Res., vol. 4, pp. 1156-1163 (1989).

3. A. Castagna, P. J. Maziasz and N. S. Stoloff, Influence of Environment on Crack Growth Resistance of an Fe_3Al,Cr Alloy, I. Baker, R. Darolia, J. D. Whittenberger, M. H. Yoo, Eds., High Temperature Ordered Intermetallic Alloys V (MRS Symp. Proc., Pittsburgh, 1993), vol. 288, pp. 1043-1048.

4. N. S. Stoloff and C. T. Liu, Intermet., vol. 2, pp. 75-87 (1994).

5. D. A. Alven and N. S. Stoloff in Proc. Tenth Annual Conf. on Fossil Energy Materials, ORNL/FMP-96/1, May 1996, pp. 225-235.

6. A. Castagna and N. S. Stoloff, Mater. and Design, vol. 14, pp. 73-75 (1993).

7. D. A. Alven and N. S. Stoloff, Scr. Metall., vol. 34, pp. 1937-1942 (1996).

8. V. K. Sikka, Oak Ridge National Laboratory, unpublished work, (1996).

9. C. G. McKamey, P. J. Maziasz, G. M. Goodwin and T. Zacharia, Mater. Sci. Eng., vol. 174, pp. 59-70 (1994).

10. A. Castagna, Ph.D. Thesis, Rensselaer Polytechnic Institute (1995).

11. B. G. Pound, Acta Metall. Mater., vol. 38, pp. 2373-2381 (1990).

12. B. G. Pound, Acta Metall. Mater., vol. 42, pp. 1551-1559 (1994).

13. P. Y. Hou and J. Stringer, Mater. Sci. Eng., vol. 202, pp. 1-10 (1995).

14. A. M. Huntz, Mat. Sci. Eng., vol. 87, pp. 251-260 (1987).

15. J. Stringer, Mater. Sci. Eng., vol. 120, pp. 129-137 (1989).

16. J. Albrecht, I. M. Bernstein and A. W. Thompson, Met. Trans. A, vol. 13A, pp. 811-820 (1982).

17. M. R. Louthan, G. R. Caskey, J. A. Donovan and D. E. Rawl, Mat. Sci. Eng., vol. 10, pp. 357 (1972).

18. J. K. Tien and R. J. Richards, Scripta Metall., vol. 9, pp. 1097-1101 (1975).

19. J. K. Tien, A. W. Thompson, I. M. Bernstein and R. J. Richards, Metall. Trans. A, vol. 7A, pp. 821-829 (1976).

EFFECTS OF TITANIUM AND ZIRCONIUM ON IRON ALUMINIDE WELDMENTS

B.L. Mulac*, R.P. Burt**, G.R. Edwards*, and S.A. David†

*Center for Welding, Joining, and Coatings Research
Colorado School of Mines
Golden, CO 80401

**Alumax Technical Center
Golden, CO 80401

†Oak Ridge National Laboratory
Metals and Ceramics Division
Oak Ridge, TN 37831

ABSTRACT

When gas-tungsten arc welded, iron aluminides form a coarse fusion zone microstructure which is susceptible to hydrogen embrittlement. Titanium inoculation effectively refined the fusion zone microstructure in iron aluminide weldments, but the inoculated weldments had a reduced fracture strength despite the presence of a finer microstructure. The weldments fractured by transgranular cleavage which nucleated at cracked second phase particles. With titanium inoculation, second phase particles in the fusion zone changed shape and also became more concentrated at the grain boundaries, which increased the particle spacing in the fusion zone. The observed decrease in fracture strength with titanium inoculation was attributed to increased spacing of second phase particles in the fusion zone.

Current research has focused on the weldability of zirconium- and carbon-alloyed iron aluminides. Preliminary work performed at Oak Ridge National Laboratory has shown that zirconium and carbon additions affect the weldability of the alloy as well as the mechanical properties and fracture behavior of the weldments. A sigmajig hot cracking test apparatus has been constructed and tested at Colorado School of Mines. Preliminary characterization of hot cracking of three zirconium- and carbon-alloyed iron aluminides, each containing a different total concentration of zirconium at a constant zirconium/carbon ratio of ten, is in progress. Future testing will include low zirconium alloys at zirconium/carbon ratios of five and one, as well as high zirconium alloys (1.5 to 2.0 atomic percent) at zirconium/carbon ratios of ten to forty.

TITANIUM INOCULATION

The superior oxidation and sulfidation resistance and good high temperature strength (up to 600°C) of iron aluminides make these materials attractive alternatives to stainless steels for structural applications in the fossil energy industry [1]. Iron aluminides also conserve strategic elements, such as chromium, and have the potential to be relatively low cost materials. However, the low room temperature ductility (less than 5 percent) observed in Fe_3Al-based alloys has hindered the implementation of iron aluminides for industrial applications.

Liu et al. [2, 3] improved the room temperature ductility of Fe_3Al-based alloys by changing the environment in which tensile testing was performed. The measured elongation improved from 2.2% in air, to 5.4 and 11.3% when tested in vacuum and dry oxygen, respectively. Liu et at. concluded that iron aluminides were intrinsically ductile and that the observed brittle behavior was the result of an extrinsic effect, namely hydrogen embrittlement. Recent research performed on iron aluminides at Oak Ridge National Laboratory has shown that an acceptable degree of room temperature ductility can be achieved in the presence of water vapor through alloying and thermomechanical processing [4, 5, 6, 7].

Although the properties of wrought iron aluminides have been improved, the weldability of Fe_3Al-based alloys remains an issue. Gas-tungsten arc welded iron aluminides form a coarse fusion zone microstructure which is susceptible to hydrogen cracking when water vapor is present in the welding atmosphere. Fasching et al. [8] refined the fusion zone microstructure in iron aluminide weldments with magnetic arc oscillation and observed that the refined fusion zone microstructure was more resistant to cold cracking in the presence of water vapor. However, the magnetic arc oscillation process was determined to be acceptable only for very precisely controlled applications, because the technique was extremely sensitive to changes in the concentration of water vapor in the welding atmosphere.

Titanium inoculation of iron aluminide weldments has also been shown to be an effective fusion zone refinement method [9]. With optimal welding parameters and titanium concentration, a fine, equiaxed fusion zone microstructure was achieved with weld pool inoculation.

EXPERIMENTAL PROCEDURE

Gas-tungsten arc welding was performed on 0.76mm iron aluminide alloy FA-129 (Fe - 28.0 at. pct. Al - 5.00 at. pct. Cr - 0.50 at. pct. Nb - 0.20 at. pct. C) sheet in a dry argon atmosphere. The fusion zone was inoculated by welding over a groove (machined into the welding coupon) which was filled with titanium powder (99.5%, <44μm) and encapsulated with a thin strip of alloy FA-129. All welding was performed at a travel speed of 2mm/s and a heat input of 142J/mm. Welding with two titanium concentrations (0.8 and 1.2 wt. pct.), plus welding without titanium inoculation, produced three unique fusion zone microstructures for slow strain rate tensile testing. The welding procedure, as well as the effect of welding parameters and titanium concentration on the fusion zone microstructure, have been published in greater detail elsewhere [9].

To produce samples for tensile testing, the original welding coupons (75mm x 50mm) were sheared to a width of 25 millimeters. A reduced section was then ground into the sample at the fusion zone, and the weld bead was ground to a uniform thickness to promote fracture within the fusion zone. Only those tests in which fracture occurred within the fusion zone were considered successful.

Slow strain rate ($2.8 \times 10^{-6} s^{-1}$) tensile testing was performed on an 810 MTS system fitted with a Plexiglas chamber to control the concentration of water vapor in the testing atmosphere. Strain rate control testing was performed in atmospheres of 300 to 9000ppm water vapor as measured by a Nyad Series 300 moisture/oxygen analyzer. For tests in water vapor atmospheres, argon was bubbled through distilled water and routed through the testing chamber until the desired water vapor concentration was achieved. The lowest water vapor concentration (approximately 300ppm) was achieved by continuously routing grade 5 argon through the chamber during the duration of the test.

Metallographic samples were prepared using standard techniques. An etchant of 60ml methanol, 40ml nitric acid, and 20ml hydrofluoric acid was used to observe the grain structure, and the etchant used to contrast the fusion zone second phase particles consisted of 96ml water, 2ml nitric acid, and 2ml hydrofluoric acid.

Second phase particles within the fusion zone were analyzed on a scanning electron microscope with energy dispersive spectroscopy (EDS) and image analysis capabilities. Additional identification analysis of the particles was performed on a scanning transmission electron microscope (STEM) capable of EDS as well.

RESULTS AND DISCUSSION

As previously reported, extensive fusion zone grain refinement was achieved by titanium inoculation. The addition of 0.8 and 1.2 weight percent titanium reduced the fusion zone grain size from 530μm to 370μm and 70μm, respectively. With the significant fusion zone refinement accomplished, it was expected that slow strain rate tensile tests would show improved weldment properties similar to the results of the magnetic arc oscillation study by Fasching et al. [8]. However, with an increased titanium concentration, the fracture strength of the weldment decreased. For each titanium concentration, fracture strength also decreased with increasing water vapor concentration.

The reduced fracture strength was not the result of a change in fracture mode. With titanium inoculation, the fraction of second phase particles at the grain boundaries increased from 15 to approximately 50 percent. With the increased concentration of second phase particles at the grain boundaries, the decrease in fracture strength was originally suspected to have been caused by a change to intergranular fracture. However, all fractures occurred by transgranular cleavage, as was observed by Fasching et al. In other research performed on an Fe_3Al-based alloy, alloying with carbon caused the perovskite phase, Fe_3AlC, to be preferentially precipitated out at the grain boundaries, which reduced the ductility [10]. The presence of the perovskite phase at the grain boundaries, however, did not change the fracture mode. When the same material was decarburized, the precipitates did not form and ductility was recovered. The presence of second phase particles at the grain boundaries can change the mechanical properties of iron aluminides without changing the fracture mode. Given the normally brittle behavior of iron aluminides, fracture initiation, not propagation, is the key concern.

The initial proposal of this research was that the hydrogen cracking susceptibility of weldments could be decreased by refining the fusion zone microstructure, as demonstrated. Fasching et al. [8] showed that the fracture strength of iron aluminide weldments refined by magnetic arc oscillation could be predicted using a Hall-Petch type model, indicating that the fracture strength was controlled by the length of the dislocation pileups at the grain boundaries. The coarse fusion zone microstructure in iron aluminide weldments accommodates relatively long dislocation pileups, generating an area of high stress concentration at the tip of each pileup. A relatively low applied stress is required to initiate fracture at the tip of a long dislocation pileup. The coarse fusion zone microstructure also provides easy crack propagation paths, further decreasing the properties of the weldment. Finer-grained materials exhibit improved mechanical properties because the average slip length is shorter, which reduces the stress at the tip of a dislocation pileup. A higher stress must therefore be applied to initiate cleavage fracture. A finer microstructure also results in a more torturous path for crack propagation. However, the finer fusion zone microstructure in inoculated weldments failed to improve the mechanical properties.

Grain boundaries are not the only microstructural features which can act to pin dislocations. Dislocations moving on a slip plane can be blocked by a second phase particle, and assuming that conditions are such that climb is difficult, a pileup can be formed at the particle. The space between particles then controls the length of the pileup.

Liu and Gurland [11] proposed a model for higher-carbon steels which related the fracture strength to the maximum slip distance as defined by the average particle spacing. The model proposed by Liu and Gurland is:

$$\sigma = \sigma_o + \frac{\sigma_c}{2}\sqrt{\rho/\Lambda} \tag{1}$$

where:

σ = applied stress
σ_o = friction stress
σ_c = critical fracture stress of matrix
ρ = radius of curvature at crack tip
Λ = available slip distance

A linear relationship between the inverse square root of the mean particle intercept length and the fracture strength was found to exist for high carbon steels, similar to a Hall-Petch plot. Similar results were later obtained by Curry and Knott [12] for quenched and tempered steels.

With titanium inoculation, the second phase particle spacing in iron aluminide weldments was observed to be dependent upon the concentration of titanium in the fusion zone. With increased titanium concentration, the mean particle intercept length increased in the fusion zone. The fracture strength of both inoculated and non-inoculated weldments are plotted against the mean particle intercept length in Figure 1. The measured fracture strengths corresponded well to the mean intercept length, implying that the fracture strength of FA-129 weldments was controlled by the second phase particle spacing.

Because second phase particles provide cleavage nucleation sites, attributes other than the spacing of the particles can affect the mechanical properties of a material. Cleavage fracture has been proposed to initiate by three general mechanisms: slip bands blocked by barriers, mechanical twin intersections, and cracking of brittle second phase particles [13]. Cracking of second phase particles appears to be the most likely mechanism for the initiation of transgranular cleavage in iron aluminides.

Both fractured second phase particles and fractured particle/matrix interfaces were observed in inoculated FA-129 weldments after tensile testing (Figure 2). Liu and Gurland [11] observed both fracture types in steels, and concluded that, although both

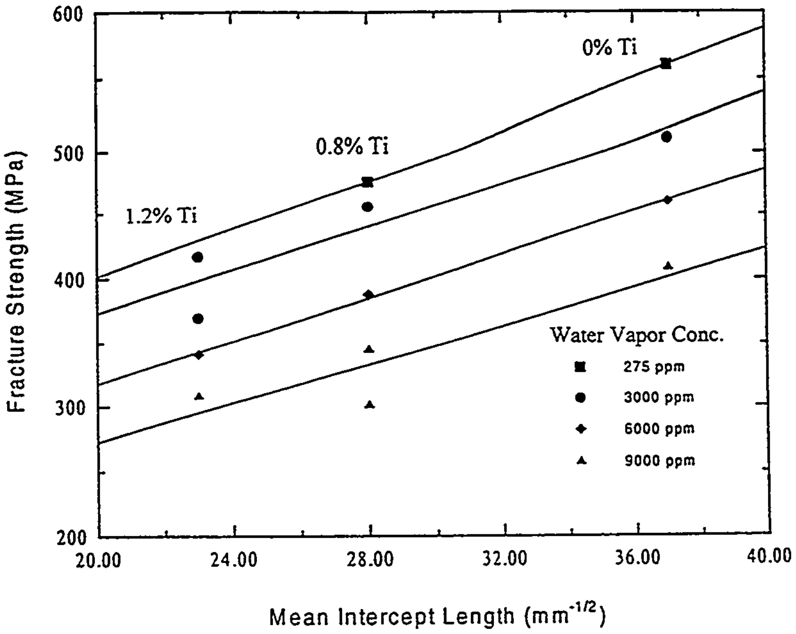

Figure 1. Effect of second phase particle spacing on the fracture strength of FA-129 weldments.

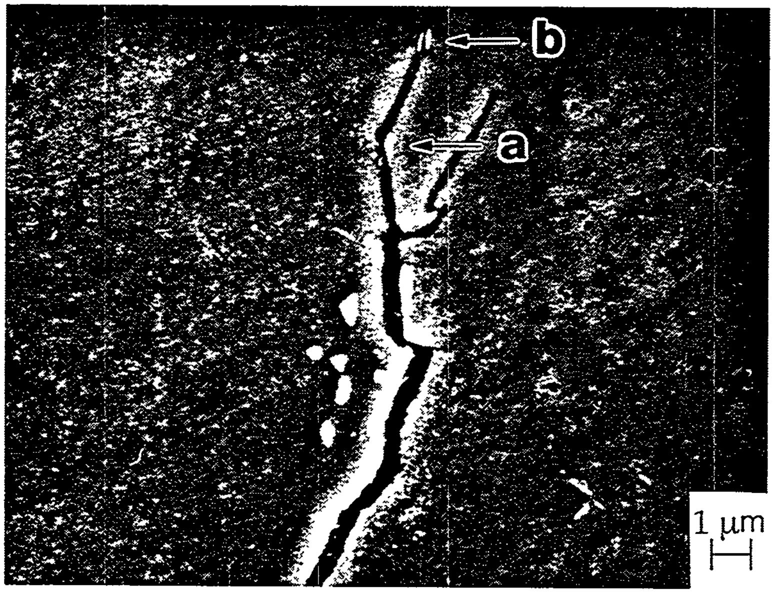

Figure 2. Fusion zone second phase particles associated with fracture in inoculated weldment. a) Failed interface b) Fractured particle.

defect types could initiate void formation, only carbide fracture could initiate cleavage nucleation. Given the hydrogen cracking susceptibility of iron aluminides, once a microcrack is initiated at a second phase particle and the Griffith crack propagation criteria is satisfied, the crack will propagate in an unstable manner. It is assumed then, that the stress required to fracture the second phase particles in the iron aluminide weldments influenced the fracture strength measured for the titanium inoculated weldments. The stress required to fracture a second phase particle is a function of the type, size, and shape of the second phase particles.

The type of second phase particle is critical because its fracture strength is dependent upon composition and crystal structure. In the present study, niobium carbides were observed in the non-inoculated welds. With titanium inoculation, the fusion zone second phase particles were observed to have a different composition. The particles consisted of niobium, titanium, and carbon. Selected area diffraction (SAD) analysis also revealed that the structure of the particles was face-centered cubic. The exact phase formed in the inoculated fusion zone was not determined. However, both niobium and titanium carbides are face-centered cubic, so the phase was most likely a complex titanium and niobium bearing carbide.

Although both carbides precipitated were face-centered cubic, they may have different fracture strengths, which are unknown. The change in particle composition and location (at the grain boundary) would have changed the stress required to initiate fracture, but the impact on weldment properties was not clear and was assumed to be a secondary effect.

With the addition of titanium to the weld metal, the second phase particles not only changed in composition, but were also observed to change in size and shape. Table 1 summarizes the fusion zone second phase particle characteristics. As titanium concentration increased, the second phase particles became more elongated and less spherical.

Table 1. Size and Shape of Fusion Zone Second Phase Particles

Weight Percent Titanium	Avg. Particle Diameter (μm)	Aspect Ratio (length/width)
0	0.51±0.24	1.7
0.8	0.44±0.16	2.7
1.2	0.52±0.16	2.6

The shape of the carbide impacts the fracture strength of a material by changing the type of crack formed when the particle is fractured. When spherical particles are fractured, a penny-shaped crack is formed. The Griffith crack propagation criteria for a penny-shaped crack is:

$$\sigma_f = \left(\frac{\pi E \gamma_p}{2\left(1-\upsilon^2\right) r} \right)^{1/2} \qquad (2)$$

where:

γ_p = effective surface energy
υ = Poisson's ratio
r = particle radius

A cracked grain boundary carbide is characterized as a through-thickness nucleus. The Griffith crack criteria for a through-thickness nucleus is:

$$\sigma_f = \left(\frac{2 E \gamma_p}{\pi\left(1-\upsilon^2\right) r} \right)^{1/2} \qquad (3)$$

Note that the change from a penny-shaped nucleus (spherical particle) to a through-thickness nucleus (grain boundary particle) reduces the material fracture strength by a factor of $\pi/2$. Curry and Knott [14] confirmed the dependence of the fracture strength on the size and shape of carbides in tool steels. Fracture strength was observed to decrease as carbides became larger and more elongated.

As previously noted, when titanium was added to the FA-129 fusion zones, the second phase particles were concentrated at the grain boundaries. These grain boundary particles were much more elongated than the majority of the particles in the non-inoculated fusion zones (Table 1). Therefore, the decreased fracture strength observed with titanium inoculation could have been a result of the changed shape of the cleavage nucleation sites as the particles became less spherical. However, if the fracture strength was dependent upon the second phase particle shape, the relationship between the fracture strength and particle spacing would not have been linear as was shown (Figure 1).

The addition of 0.8 weight percent titanium to the fusion zone caused the second phase particles to become more elongated. Assuming that the particle shape was critical, the decrease in fracture strength measured with the 0.8 weight percent titanium addition would have consisted of two components, a decrease caused by the increased particle spacing and a decrease caused by the particle shape change. The highest titanium addition, 1.2 weight percent, further decreased the fracture strength, but the addition did not cause any further second phase particle shape change (Table 1). The decreased fracture strength measured, therefore, could only be attributed to the increased particle spacing, and a linear relationship would not have existed between the fracture strengths and the three second phase particle spacings. Since the relationship was linear, the fracture strength could not have been dependent upon the second phase particle shape over the range of shapes observed in this study.

CONCLUSIONS

Although titanium inoculation effectively refined the fusion zone microstructure in iron aluminide weldments, the fracture strength was deteriorated by the addition of titanium. With titanium inoculation, second phase particles in the fusion zone concentrated at the grain boundaries. The higher frequency of grain boundary particles increased the spacing of the fusion zone second phase particles as well as the average aspect ratio of the particles. Transgranular cleavage was more easily initiated in weldments with the highly spaced, elongated second phase particles. Given the cracking susceptibility of iron aluminides in the presence of water vapor, a more facile fracture initiation decreased the fracture strength of the weldments.

ZIRCONIUM- AND CARBON-ALLOYED IRON ALUMINIDES

Current work has focused on the weldability of zirconium- and carbon-alloyed iron aluminides. Work performed at Oak Ridge National Laboratory has shown that additions of zirconium and carbon greatly affect the mechanical properties of iron aluminides. Studies have shown that carbides of zirconium have a beneficial effect on creep resistance and additions of 0.1% to 0.5% zirconium improve tensile and fatigue properties [17]. Small amounts of zirconium are beneficial for oxidation resistance as well. Zirconium changes the morphology of the oxides formed at high temperature and retards oxide spalling [18].

However, a major concern with zirconium-containing alloys is weldability. Hot cracking has been observed more frequently in zirconium-containing alloys than was seen with alloy FA-129 or other ternary alloys. Zirconium lowers the liquidus temperature of the alloy, which results in an increase in the amount of liquid present during weld solidification. Two techniques have been identified as possible solutions to the hot cracking problems: 1) reduce the amount of liquid present during weld solidification, and 2) increase the amount of liquid present during weld solidification. The first technique would involve decreasing the amount of zirconium present during the time of solidification either by decreasing the total concentration of zirconium in the alloy, or by adding sufficient carbon to tie the zirconium up as zirconium carbides prior to final solidification. The second technique looks at increasing the amount of zirconium concentration in the alloy to provide enough liquid to back fill a forming hot crack and "heal" it. Future research on this program will be focused on characterizing the effects of zirconium and carbon on the hot cracking resistance of iron aluminides.

PRELIMINARY TESTING AND RESULTS

Testing of hot cracking resistance is in progress on three iron aluminide alloys containing zirconium and carbon. Compositions are shown in Table 2. The alloys contain different total concentrations of zirconium at the same zirconium/carbon ratio of ten. Alloy specimens are cut from 0.76mm sheet into 50x50mm coupons, heat treated at 650°C for two hours, and then pickled to remove any oxide. Gas tungsten arc welding and determination of the critical cracking stress in a sigmajig apparatus constitutes the testing procedure.

Table 2. Compositions of Zirconium-Containing Alloys

Alloy	Fe (at%)	Al (at%)	Cr (at%)	Zr (at%)	C (at%)
A	Bal.	28	5	0.2	0.02
B	Bal.	28	5	0.35	0.035
C	Bal.	28	5	0.5	0.05

The threshold hot cracking stress of alloys A and C have been determined to be 10 KSI and 8 KSI, respectively. The results indicate that increasing zirconium content decreases the hot cracking resistance of iron aluminides. When compared with other iron aluminide alloys (see Table 3 for compositions), the hot cracking resistance of the zirconium/carbon alloys is inferior, as shown in Figure 3.

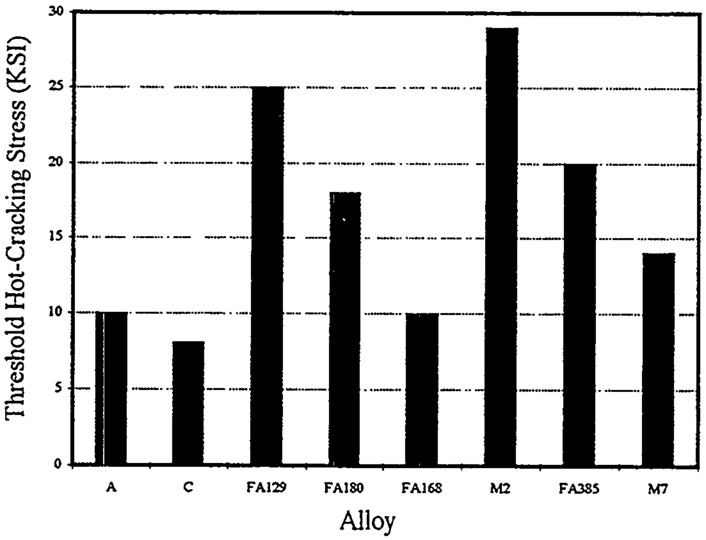

Figure 3. Comparison of threshold stress of zirconium-containing alloys to other iron aluminides.

Table 3. Compositions of Other Iron Aluminides.

Alloy	Al (wt%)	Mo (wt%)	Zr (wt%)	B (ppm)	Cr (wt%)	Nb (wt%)	C (wt%)
FA129	16	-	-	-	5.4	1.0	0.04
FA180	16	1.6	0.05	10	5.4	1.0	0.01
FA168	16	1.6	0.1	10	5.4	1.0	0.007
M2	21.2	0.42	0.1	50	-	-	0.03
FA385	21.2	0.42	0.1	-	-	-	0.03
M7	21.2	0.42	0.2	-	2.3	1.0	0.06

FUTURE WORK

Five alloys containing zirconium ranging from 0.05 to 0.5 atomic percent and possessing a zirconium/carbon ratio of ten will be characterized. The effects of carbon on hot cracking resistance will also be studied by varying the zirconium/carbon ration from ten to five and then one, while holding the zirconium concentration at 0.1 atomic percent. These compositions should contain less low melting point liquid during solidification and thus manifest better hot cracking resistance. High zirconium alloys (1.5 to 2.0 atomic percent or with a ratio of 30 to 40) will also be evaluated to determine the amount of zirconium necessary to eliminate hot cracking by liquid backfilling. Limited characterization of slow strain rate tensile properties of selected alloys at varying water vapor concentrations also will be performed.

Acknowledgments

This research was sponsored by the U.S. Department of Energy, Fossil Energy AR&TD Materials Program under subcontract 19X-27421C. Dr. Gene Goodwin's assistance with hot cracking equipment construction and advice was greatly appreciated. The authors also acknowledge Dr. Vinod Sikka and the Materials Processing Group at ORNL, who provided the material used in this research.

References

1. McKamey, C. G., J. H., Tortorelli, P. F., and Sikka, V. K. 1991. J. of Mat. Sci. Res. 6: 1779.
2. Liu, C. T., Lee, E. H., and McKamey, C. G. 1989. Scripta Met. 23: 875.
3. Liu, C. T., McKamey, C. G., and Lee, E. H. 1990. Scripta Met. 24: 385.
4. McKamey, C. G., Horton, J. A., and Liu, C. T. 1988. Scripta Met. 22: 1679.
5. McKamey, C. G., Horton, J. A., and Liu, C. T. 1989. J. Mat. Res. 4: 1156.
6. McKamey, C. G. and Liu, C. T. 1990. Scripta Met. 24: 2119.
7. Sanders, P. G., Sikka, V. K., Howell, C. R., and Baldwin, R. H. 1991. Scripta Met. 25: 2365.
8. Fasching, A. A., Edwards, G. R., and David, S. A. To be published. Sci. and Tech. of Welding and Joining.
9. Burt, R. P., Edwards, G. R., and David, S. A. 1996. To be published. Proc. and Fab. of Adv. Mat.-V. Proceedings of 1996 TMS Fall Meeting.

10. Kerr, W. R. 1986. Met. Trans. 17A: 2298.

11. Liu, C. T. and Gurland, J. 1968. Trans. ASM. 61: 156.

12. Curry, D. A. and Knott, J. F. 1979. Met. Sci. (June): 341.

13. McMahon, C. J. and Cohen, M. 1965. Acta Met. 13: 591.

14. Curry, D. A. and Knott, J. F. 1978. Met. Sci. (Nov.): 511.

15. Evans, A. G. 1983. Met. Trans. 14A: 1349.

16. Wallin, K., Saario, T., and Törrönen, K. 1984. Met. Sci. 18: 13.

17. Alven, D.A. and Stoloff, N.S. 1996. Proceedings of the Tenth Annual Conference on Fossil Energy Materials. Conf-9605167: 225.

18. June, M. PALL Corporation. Verbal communication.

EFFECTS OF 1000 °C OXIDE SURFACES ON ROOM TEMPERATURE AQUEOUS CORROSION AND ENVIRONMENTAL EMBRITTLEMENT OF IRON ALUMINIDES

R. A. Buchanan and R. L. Perrin

Dept. of Materials Science and Engineering
University of Tennessee
Knoxville, TN 37996-2200

ABSTRACT

Results of electrochemical aqueous-corrosion studies at room temperature indicate that retained in-service-type high-temperature surface oxides (1000 °C in air for 24 hours) on FA-129, FAL and FAL-Mo iron aluminides cause major reductions in pitting corrosion resistance in a mild acid-chloride solution designed to simulate aggressive atmospheric corrosion. Removal of the oxides by mechanical grinding restores the corrosion resistance. In a more aggressive sodium tetrathionate solution, designed to simulate an aqueous environment contaminated by sulfur-bearing combustion products, only active corrosion occurs for both the 1000 °C oxide and mechanically cleaned surfaces of FAL. Results of slow-strain-rate stress-corrosion-cracking tests on FA-129, FAL and FAL-Mo at free-corrosion and hydrogen-charging potentials in the mild acid chloride solution indicate somewhat higher ductilities (on the order of 50 %) for the 1000 °C oxide surfaces as compared to the mechanically cleaned surfaces. These results suggest that the 1000 °C oxides retard the penetration of hydrogen into the metal substrates and, consequently, are beneficial in terms of improving resistance to environmental embrittlement. In the aggressive sodium tetrathionate solution, no differences are observed in the ductilities produced by the 1000 °C oxide and mechanically cleaned surfaces for FAL.

INTRODUCTION

The overall objective was to study the effects of in-service-type high-temperature oxides on the room-temperature aqueous corrosion and environmental embrittlement properties of iron aluminides. The study was designed to be consistent with past and on-going research by Tortorelli and DeVan at the Oak Ridge National Laboratory (ORNL), who have evaluated the high-temperature oxidation resistances of Fe_3Al-based iron aluminides (FA-129 and FAL) in air to simulate combustion products.[1] Equally importantly, Tortorelli and Alexander are conducting studies to characterize the chemical, morphological, and mechanical properties of the oxide scales created by these exposures after cool-down to room temperature.[2] The characteristics of these scales, and in particular the cracking/spallation characteristics, will have a strong influence on the aqueous-corrosion and hydrogen-embrittlement behaviors of the iron aluminides during shut-down periods at room temperature.

EXPERIMENTAL PROCEDURES

FA-129 and FAL iron aluminides were selected for investigation to be consistent with the work by Tortorelli and DeVan.[1] In addition, the iron aluminide FAL-Mo was included. The chemical compositions are given in Table 1. FAL-Mo is very similar to FAL, but with the addition of 1.0 % Mo. Due to the Mo addition, it has been shown to have superior aqueous-corrosion resistance in acid-chloride and sulfur-bearing electrolytes.[3-5]

Table 1. Chemical compositions of iron aluminides (atomic percent).

Alloy	Fe	Al	Cr	Mo	B	Zr	Nb	C	Y
FA-129	66.3	28.0	5.0	-	-	-	0.5	0.2	-
FAL	66.9	28.0	5.0	-	-	0.1	-	-	-
FAL-Mo	65.9	28.0	5.0	1.0	0.04	0.08	-	-	-

To produce the in-service-type high-temperature oxide scales, specimens of all alloys were exposed to air at 1000 °C for 24 hours, then furnace cooled (based on recommendations by Dr. Peter Tortorelli at ORNL). Aqueous corrosion and environmental embrittlement tests were conducted on specimens with, and for comparison, without the 1000 °C oxide. The 1000 °C oxide specimens were first ground through 600-grit SiC, then exposed to the 1000 °C heat treatment. The specimens without the 1000 °C oxide, i.e., the mechanically cleaned specimens, were first ground through 600-grit SiC, then exposed to the 1000 °C heat treatment, then ground again through 600-grit SiC to remove the high-temperature oxides. Specimens were contained in alumina crucibles during all heat treatments.

The principal electrolyte employed in this study was a mild acid-chloride solution [pH = 4 (H_2SO_4), 200 ppm Cl^- (NaCl)]. In this solution, the alloys evaluated are susceptible, to varying degrees, to pitting corrosion. An excellent method for evaluating the relative pitting corrosion susceptibility involves producing and analyzing cyclic anodic polarization curves. A schematic illustration of a cyclic anodic polarization curve is shown in Figure 1, where certain electrochemical parameters are identified.

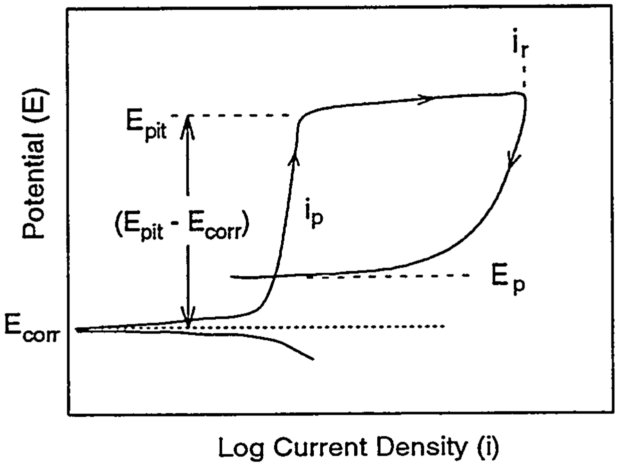

Fig. 1. Schematic illustration of cyclic anodic polarization behavior.

E_{corr} is the steady-state, open-circuit, free corrosion potential; i_p is the passive current density, reflective of passivation wherein the material develops a thin, protective, oxide/hydroxide passive film, and, therefore, corrodes at a very low rate; E_{pit} is the critical pitting potential at which pitting corrosion initiates; i_r is the reversing current density; and E_p is the protection (or repassivation) potential. A parameter often used to characterize the relative resistance to pitting corrosion is the difference between E_{pit} and E_{corr}, i.e., $(E_{pit} - E_{corr})$, with higher values corresponding to greater pitting resistance.

In the present study, room-temperature cyclic anodic polarization tests were conducted utilizing a standard polarization cell and an EG&G Model 273 potentiostat. Stabilization of each specimen was allowed to occur for at least one hour, after which E_{corr} was measured. The cyclic polarization curve was then generated at a scan rate of 600 mV/h. The reversing current density was 1000 $\mu A/cm^2$. Polarization tests were conducted on FA-129, FAL and FAL-Mo in the mild acid-chloride solution [pH = 4 (H_2SO_4), 200 ppm Cl^- (NaCl)] to simulate aggressive atmospheric corrosion. In addition, tests were conducted on FAL in 0.001 M sodium tetrathionate solution ($Na_2S_4O_6$) to simulate an aqueous solution contaminated by sulfur-bearing combustion products.

The environmental embrittlement characterizations involved room-temperature slow-strain-rate tests (SSRTs) in the mild acid-chloride solution (FA-129, FAL and FAL-Mo) and the sodium tetrathionate solution (FAL). In these tests, the specimens were continuously strained in tension at a very slow rate to enhance corrosion and hydrogen-embrittlement effects. The tests were conducted at a strain rate of $1.2 \times 10^{-6}\ s^{-1}$ in a load frame which contained the corrosion cell. Tests were conducted at the free corrosion potential, E_{corr}, and at a cathodic hydrogen-charging potential of -1500 mV(SHE).

RESULTS AND DISCUSSION

The cyclic anodic polarization behaviors of FA-129 (28Al-5Cr), FAL (28Al-5Cr-0.1Zr) and FAL-Mo (28Al-5Cr-1Mo-0.08Zr), in the 1000 °C oxide and mechanically cleaned conditions and in the mild acid chloride solution, are shown in Figures 2, 3 and 4, respectively. The polarization results are summarized in Figure 5, where the resistance to localized corrosion (in terms of the measured parameter (E_{pit} - E_{corr})) is shown for all materials in both surface conditions. In cases where passivation was not obvious, E_{pit} was taken as the potential corresponding to a current density of 10 $\mu A/cm^2$. It is apparent that the mechanically cleaned surfaces for all materials demonstrated superior localized corrosion resistance relative to the 1000 °C oxide surfaces.

The polarization results for FAL-Mo in the 0.001 M sodium tetrathionate solution are shown in Figure 6. This solution proved to be very aggressive toward both the 1000°C oxide and mechanically cleaned conditions. Passivation did not occur for either surface condition.

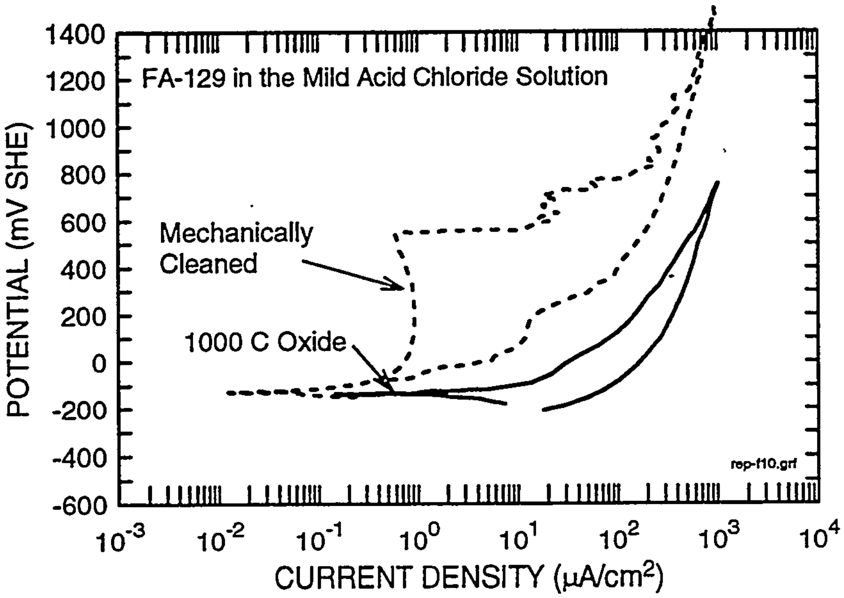

Fig. 2. Cyclic anodic polarization behaviors of FA-129 with 1000 °C oxide and mechanically-cleaned surfaces in the mild acid chloride solution.

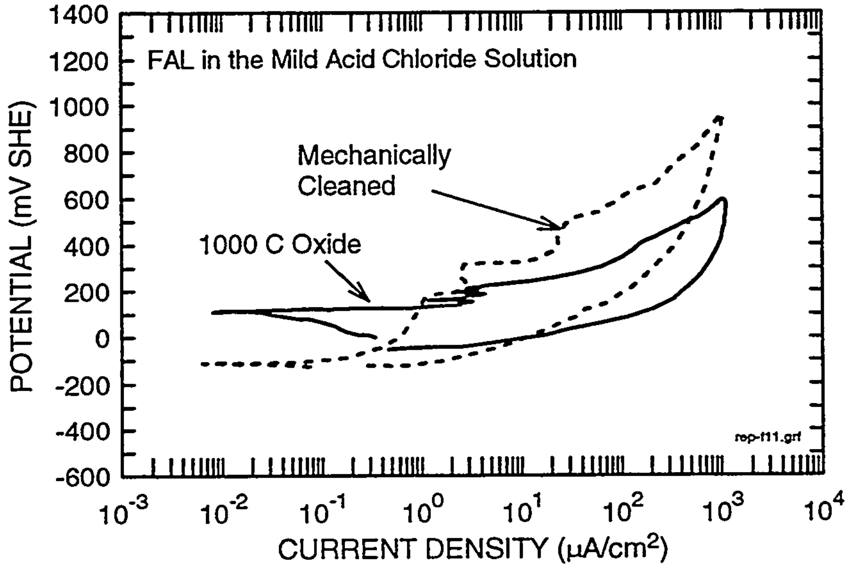

Fig. 3. Cyclic anodic polarization behaviors of FAL with 1000 °C oxide and mechanically-cleaned surfaces in the mild acid chloride solution.

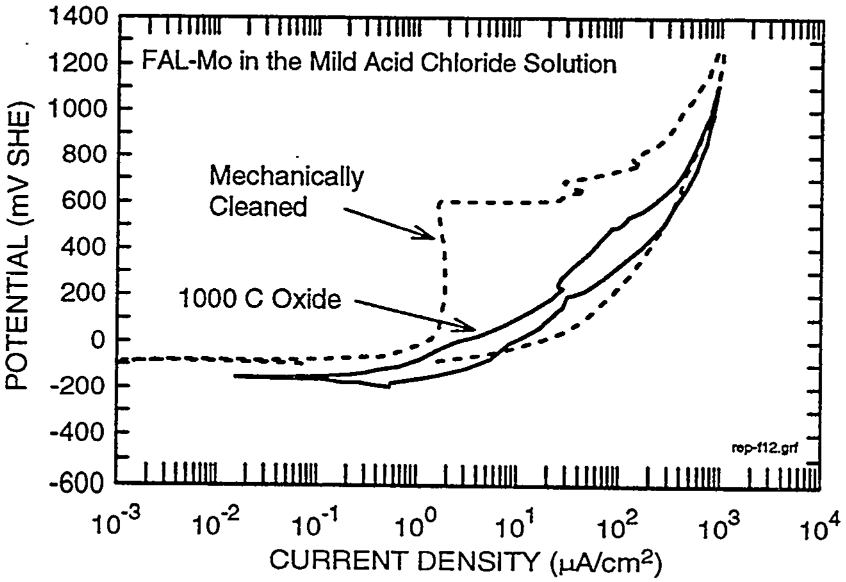

Fig. 4. Cyclic anodic polarization behaviors of FAL-Mo with 1000 °C oxide and mechanically-cleaned surfaces in the mild acid chloride solution.

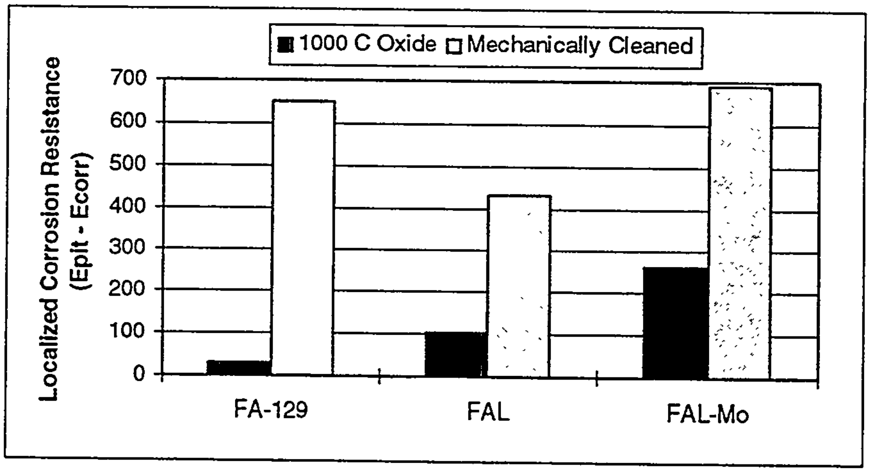

Fig. 5. Effects of 1000 °C oxide and mechanically cleaned surfaces on localized corrosion resistance in the mild acid chloride solution.

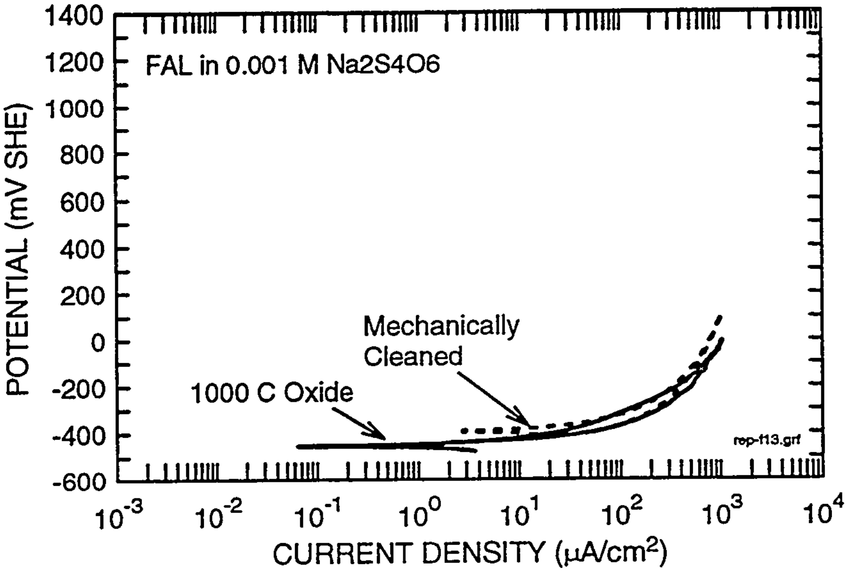

Fig. 6. Cyclic anodic polarization behaviors of FAL with 1000 °C oxide and mechanically-cleaned surfaces in the 0.001 M sodium tetrathionate solution.

The slow-strain-rate test results for replicate specimens of FA-129, FAL and FAL-Mo in the mild acid chloride solution, in terms of the average percent-total-plastic-elongation at the free corrosion potential, E_{corr}, and at the hydrogen-charging potential, -1500 mV(SHE), are given in Figure 7(a) and (b), respectively. It is seen that the 1000 °C oxide surfaces produced higher ductilities than the mechanically cleaned surfaces for all materials at both potentials. At E_{corr}, the average increase in ductility was 39 %, and at -1500 mV(SHE), 52 %. At the hydrogen-charging potential, the FAL and FAL-Mo 1000 °C oxides were noticeably more effective than the FA-129 1000 °C oxide in improving the ductilities. These results imply that the 1000 °C oxides retard hydrogen penetration into the metal substrates and, therefore, improve the resistances of the materials to environmental embrittlement. Under the conditions of this study, the 1000 °C oxides produced beneficial effects, but not dramatically beneficial effects.

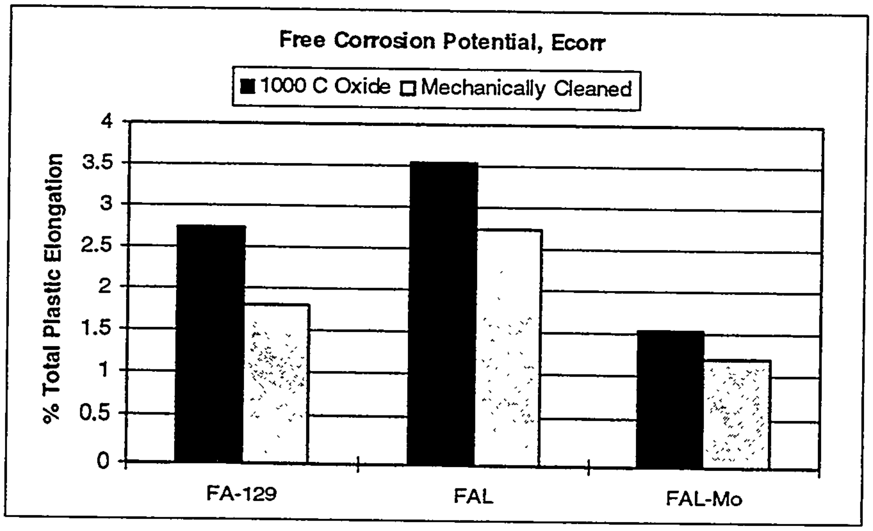

(a)

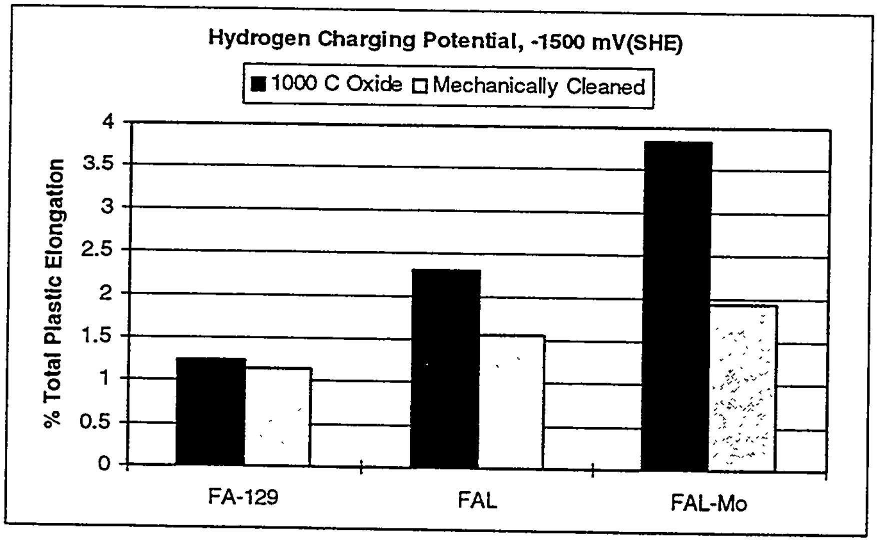

(b)

Fig. 7. Slow-strain-rate test results for iron aluminides in the mild acid chloride solution at (a) the free corrosion potential, E_{corr}, and (b) the hydrogen-charging potential, -1500 mV(SHE).

The slow-strain-rate test results for FAL in the 0.001 M sodium tetrathionate solution, in terms of percent total plastic elongation and fracture stress values, are presented in Table 3. It is seen that the 1000 °C oxide and mechanically cleaned surfaces produced approximately equal ductilities at each of the potentials. Therefore, in this solution, which was considerably more aggressive than the mild acid chloride solution, no beneficial effects were observed for the 1000 °C oxide surfaces in terms of resistance to environmental embrittlement.

Table 3. Results of slow strain-rate tests on FAL iron aluminide in 0.001 M sodium tetrathionate solution.

Material	Potential	Surface Condition	Fracture Stress		Percent Total Plastic Elongation
			(ksi)	(MPa)	
FAL	E_{corr}	Mechanically Cleaned	23	158	1.2
		1000°C Oxide	23	158	1.2
	-1500 mV SHE	Mechanically Cleaned	32	220	1.4
		1000°C Oxide	26	179	1.6

CONCLUSIONS

In terms of room-temperature aqueous corrosion behavior in the mild acid chloride solution, designed to simulate aggressive atmospheric corrosion, the retained 1000 °C oxides (reflective of in-service oxidation) consistently produced major, detrimental results relative to the mechanically cleaned surfaces. Specifically, the pitting corrosion resistances were much lower for the 1000 °C surfaces, relative to the cleaned surfaces, for FA-129, FAL and FAL-Mo Fe_3Al-based iron aluminides. It is believed that the detrimental corrosion effects associated with the high-temperature oxides are related to flaws in the oxides which serve as crevice corrosion sites, thus increasing the susceptibility to localized corrosion.

In terms of room-temperature environmental embrittlement behavior in the mild acid chloride solution, the retained 1000 °C surface oxides consistently produced marginally beneficial results relative to the mechanically cleaned surfaces. Specifically, slow-strain-rate tests of FA-129, FAL and FAL-Mo at free-corrosion and cathodic-hydrogen-charging potentials showed consistently higher ductilities (≈ 50 % higher) for the 1000 °C oxide surfaces as compared to the cleaned surfaces. It is believed that the beneficial effects associated with the high-temperature oxides, i.e., greater resistance to environmental embrittlement, are due to the oxides serving as barriers to hydrogen penetration of the metal substrates in those surface regions where the oxides maintain adherency with the substrates.

More detailed information on this study is available in Reference 6.

REFERENCES

1. J. H. DeVan and P. F. Tortorelli, "Environmental Effects on Iron Aluminides," Proceedings of the Eighth Annual Conference on Fossil Energy Materials, ORNL/FMP-94/1, 309-320, Oak Ridge National Laboratory, Oak Ridge, TN (1993).

2. P. F. Tortorelli and K. B. Alexander, "Mechanically Reliable Scales and Coatings," pp. 247-56 in Proceedings of the Ninth Annual Conference on Fossil Energy Materials, N. C. Cole and R. R. Judkins (comp.), U. S. Department of Energy, August 1995.

3. R. A. Buchanan and J. G. Kim, "Fe_3Al-Type Iron Aluminides: Aqueous Corrosion Properties in a Range of Electrolytes and Slow-Strain-Rate Ductilities During Aqueous Corrosion," Final Report, U. S. Dept. of Energy, Fossil Energy AR & TD Materials Program, ORNL/Sub/88-07685CT92/02, National Technical Information Service, Springfield, VA, August, 1992.

4. J. G. Kim and R. A. Buchanan, "Aqueous Corrosion Properties and Slow-Strain-Rate Ductilities of Fe_3Al-Based and Lean-Aluminum Iron Aluminides," Final Report, U. S. Dept. of Energy, Fossil Energy AR & TD Materials Program, ORNL/Sub/88-07685CT92/03, National Technical Information Service, Springfield, VA, August, 1993.

5. J. G. Kim and R. A. Buchanan, "Pitting and Crevice Corrosion of Iron Aluminides in a Mild Acid-Chloride Solution," Corrosion, Vol. 50, No. 9, pp. 658-668, Sept., 1994.

6. R. A. Buchanan and R. L. Perrin, "Effects of High Temperature Surface Oxides on Room Temperature Aqueous Corrosion and Environmental Embrittlement of Iron Aluminides," Final Report, U. S. Dept. of Energy, Fossil Energy AR & TD Materials Program, ORNL/Sub/88-07685CT92/05, National Technical Information Service, Springfield, VA, September, 1996.